UNIVERSITÀ DEGLI STUDI DI PADOVA

Dipartimento di Fisica e Astronomia "Galileo Galilei"

Master Degree in Physics

Final Dissertation

Commissioning of a Microdosimetric Device for Hadrontherapy

Thesis supervisor

Prof. Marco Mazzocco

Thesis co-supervisor

Dr. Valeria Conte

Candidate

Riccardo Lombardi

Academic Year 2021/2022

Abstract

The present work aims at the characterization of a new microdosimetric device, specifically designed and constructed to be used in proton therapy centers by medical physicists. The new device should be reliable in terms of stability over time and reproducibility, and easy to use. It will be equipped with an integrated preamplifier and a dedicated user-friendly software for data analysis. The core, i.e. the radiation sensor, of the microdosimetric device is a **mini**aturized **T**issue **E**quivalent **P**roportional **C**ounter (mini-TEPC), with a sensitive volume of only 1 mm in diameter, which is designed and constructed at the **L**egnaro **N**ational **L**aboratories (LNL) of INFN. A series of five mini-TEPCs has been designed and constructed as a result of a close collaboration between the research group and the Technical Office and Mechanical workshop of LNL. A user-friendly software (*MikAna*) for the data analysis has been developed in C++, equipped with a **G**raphic **U**ser **I**nterface (GUI) and tested on different machines. The software has been designed to be as simple and intuitive as possible, without losing in computational power and flexibility. In addition, *MikAna* has been implemented with several control routines that give a warning for wrong setting of the analysis parameters and/or system failures occurred during the data acquisition.

A dedicated fast charge-sensitive preamplifier has been developed at *Politecnico di Milano*. This preamplifier is characterized by a low signal-to-noise ratio and a large dynamic range, to detect small signals produced by sparsely ionizing particles as well as signals about four orders of magnitudes larger, produced by densely ionizing particles. These signals can be both present in mixed radiation fields produced in a typical proton treatment. Microdosimetric measurements have been performed both with the new preamplifier and with a commercial one.

The five mini-TEPCs have been tested at the CN accelerator of LNL-INFN, where the reaction ^{7}Li(d,n)^{8}Be has been exploited to produce a neutron field. The response function of the five detectors has been studied by analyzing the full microdosimetric spectra and the relevant mean values of the measured distributions. As a reference, measurements have also been performed with commercial TEPCs.

An additional test has been performed at the proton Therapy Center of Trento, using a mono-energetic 70 MeV proton beam. In particular, by exposing the mini-TEPC at different beam currents, the response function has been investigated as function of the event count rate at the detector.

Furthermore, to study the angular response, paired measurements were performed rotating the mini-TEPC of 90° with respect to the beam direction, at two different proton energies.

Contents

Chapter 1

Microdosimetry

1.1 Proton Therapy

1.1.1 Cancer and its Treatment

As reported by the **I**nternational **A**gency for **R**esearch on **C**ancer (IARC), cancer is the first leading cause of premature death at ages between 30 to 69 years in industrialized countries [1]. In 2016, about 30% of premature deaths from non-communicable diseases, i.e. non transmissible diseases, were due to cancer. Cancer is distinguished by an abnormal growth of cells in the body, which, due to mutations in their DNA, have lost their specific functionality. Its definition is based on four characteristics [2]:

1. Clonality: cancer originates from a single mutated cell, which replicate itself and therefore creates a large number of cells with the same abnormal DNA, increasing the volume of the tumor.
2. Autonomy: these mutated cells do not respond to the chemical and biological control mechanisms employed by the organism to function properly.
3. Anaplasia: the aberrations in the DNA caused the cells to lose their functionalities.
4. Metastasis: under some conditions the cancer cells are able to use the blood vessels to migrate in the body and develop one or more secondary tumor masses, even far from the origin site.

Malignant tumors can be treated with surgery, chemotherapy and radiotherapy, or with a combination of them. The choice of the treatment is based on the type of tumor, its location in the body and the presence of metastasis. Surgery consists in the physical removal of the tumor mass, and it is the first choice for solid tumors if they are easily accessible. Chemotherapy is defined as the administration of specific types of drugs able to interfere with the multiplication process of cells with high rates of proliferation, such as tumor cells. Radiotherapy consists in the treatment of malignant tumors by mean of ionizing radiation, and it is usually used for deep-seated tumors or tumors close to sensitive organs, such as the brain.

1.1.2 Radiotherapy Techniques

In radiotherapy, cancer control is based on the energy release of radiation inside the tumor, leading to ionization and excitation of the constituent atoms. As will be discussed in the next sections, radiation-induced ionization can lead to ruptures in the DNA helix, inducing mutations, aberrations of the chromosome or cell death. Radiotherapy employing high energy photons or electrons includes about the 50% of cancer treatments, and the dose profile for these beams is characterized by an initial increase behind the entrance point, after which the relative dose exponentially decreases as a function of the depth. This dose distribution is far from the ideal case in which normal tissue surrounding the tumor is spared from irradiation, and for this reason hadron therapy is an emerging technique thanks to charged particles' physical and radio-biological advantages compared to X-rays [3].

In fact, energetic protons and heavier ions, such as α particles or carbon ions, deposit the majority of their energy in the *Bragg peak*, as shown in Figure 1.1. After that, the energy deposition strongly decreases. This effect is a consequence of the mechanism of interaction of charged particles with matter, encoded in the Bethe-Bloch formula [4]:

$$-\frac{\mathrm{d}E}{\mathrm{d}x} = \frac{4\pi}{m_e c^2}\frac{nz^2}{\beta^2}\left(\frac{e^2}{4\pi\epsilon_0}\right)\left[\ln\left(\frac{2m_e c^2\beta^2}{I(1-\beta^2)}\right) - \beta^2\right] \tag{1.1}$$

where n is the electron density of the target and I its first ionization energy, β the relativistic velocity of the impinging particle and z its charge. Thanks to a good positioning of the Bragg peak it is possible to concentrate almost all the energy release of the protons inside the tumor volume, reducing the collateral damage to the detriment of normal tissue, as shown in Figure 1.2.

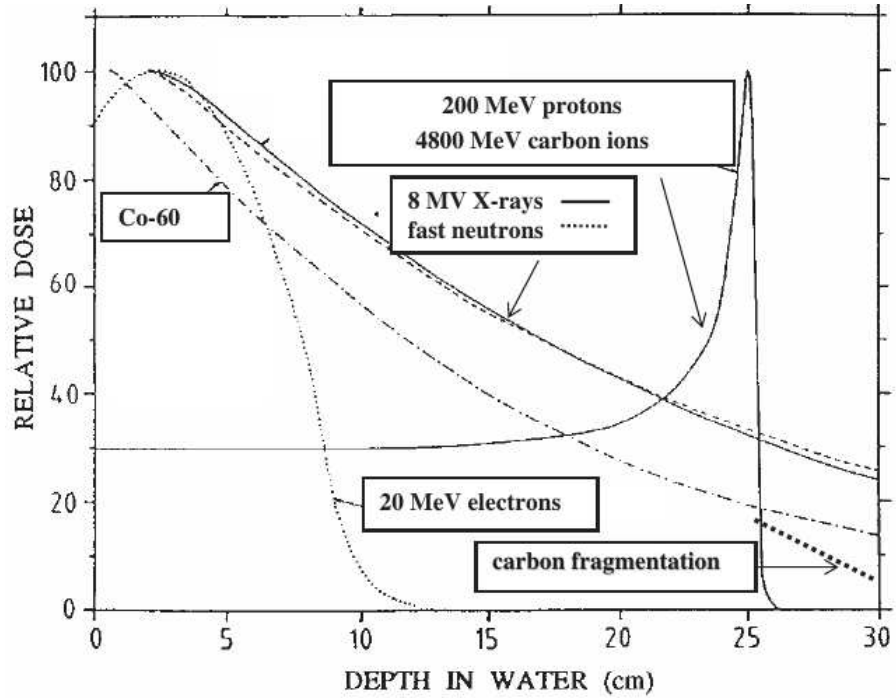

Figure 1.1: Comparison of the depth-dose curves for photons, neutrons and protons.

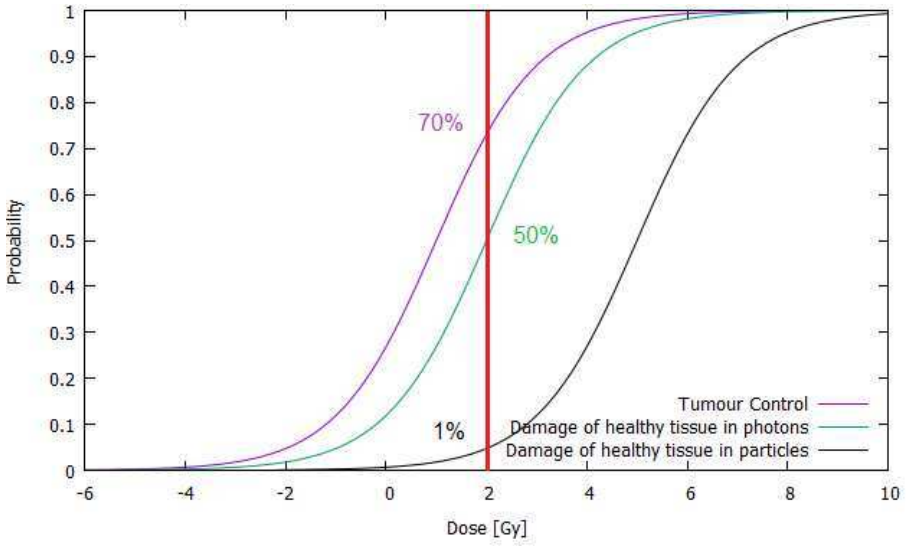

Figure 1.2: Tumor control (purple line) and damage of healthy tissue in photons (green line) and charged particles (black line).

In most practical situations the Bragg peak of a mono-energetic beam is so narrow (less than 1 mm) that it is necessary to "move" the peak in depth, in order to cover all of the tumor volume. This is done by changing the energy of the beam and weighting the components of different energies. The result, as shown in Figure 1.3, is a dose-depth curve presenting a flat top, which extends along all the depth of the tumor, called **S**pread **O**ut-**B**ragg **P**eak (SOBP). To impart as much as possible a uniform dose, beams coming from several different direction are usually employed.

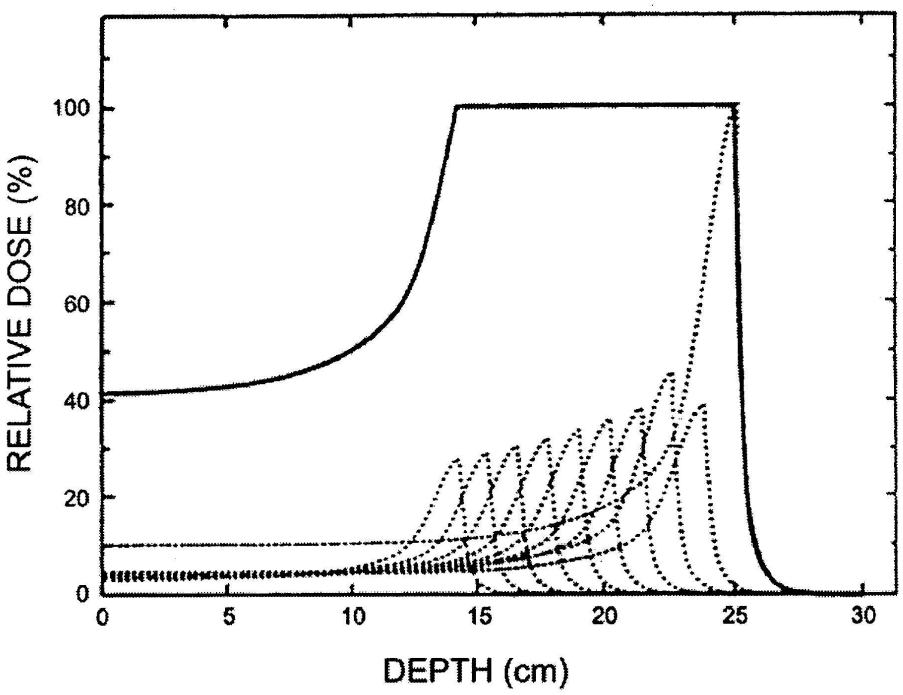

Figure 1.3: Depth dose distribution of the SOBP (solid line) and its components (dotted lines).

1.1.3 Role of Experimental Microdosimetry in Proton Therapy

In current clinical practice, the treatment planning system often includes consideration of radiation quality parameters. In proton therapy, in particular, the use of a fixed RBE of 1.1 to weight the physical dose is under discussion due to evidence of an increase of RBE along the depth dose profile, especially at the end of the particle range [5,6]. Considered the intrinsic uncertainty in the calculation of radiation quality parameters by analytic algorithms or Monte Carlo calculations, experimental microdosimetry is a useful tool to measure the agreement between the planned and the delivered treatment, thus reducing the uncertainties of the biological effectiveness calculated by the **T**reatment **P**lanning **S**ystem (TPS). However, at present there is no routine use of experimental microdosimetry in ion-beam therapy: while the calculated dose distributions produced by the TPS are routinely verified with ionization chambers as part of the quality assurance program, there is no commercial detector available to perform routine verification of the radiation quality. The development of a miniaturized TEPC goes in the direction of making microdosimetry a standard methodology for the quality assurance of advanced treatment planning that takes into account the variable radiation quality. The reduction of the sensitive volume to 1 mm in diameter, allows to cope with high intensity beams, typical of proton therapy. In comparison with the commercial *FWT LET-1/2"* counter, which has an internal diameter of 1.27 cm, the counting rate in the mini-TEPC is reduced by a factor of approximately 500, therefore limiting pile up effects due to high counting rates.

1.2 Overview on Microdosimetry

Ionizing radiation deposits energy in the medium through which it passes as a results of the interaction with the electrons and nuclei of matter. Since the nature of the interaction is purely stochastic, especially at the scale of sub-cellular structures (i.e. the chromosome, chromatine, DNA,...) which are the main biological sites of interest, a precise determination of radiation damage is difficult to achieve without a detailed study in the local energy deposition pattern.

The main objective of microdosimetry is the study of the statistical variation in the energy deposition of the single ionizing particle crossing a volume of micrometric size, similar to sub-cellular structures [7].

As a first approximation it is assumed that the radiation damage is related to the energy absorbed by the medium. The typical quantity to evaluate the damage is the dose, defined as the mean energy imparted by radiation, $\mathrm{d}\bar{\epsilon}$, divided by the target mass $\mathrm{d}m$:

$$D = \frac{\mathrm{d}\bar{\epsilon}}{\mathrm{d}m}\ [\mathrm{Gy}], \quad 1\ \mathrm{Gy} = 1\ \mathrm{J}\cdot\mathrm{kg}^{-1} \tag{1.2}$$

However, it has been observed that even for equal absorbed dose, different radiation qualities (particle type and velocity) produce different biological effects, as a result of the different patter of energy deposition along the particle track. The effect of a certain radiation quality is usually characterized in terms of **R**elative **B**iological **E**ffectiveness (RBE), defined as the ratio between the dose needed to induce a certain biological effect by a reference radiation quality, usually photons, and the dose by the tested radiation needed to achieve the same biological effect. An example is presented in Figure 1.4, where it is possible to observe that to achieve a survival fraction of 10% (y-axis) almost 1/3 of the dose is enough for carbon ions (2 Gy) with respect to photons (6 Gy) with a consequent lower dose delivered also to the healthy tissues surrounding the tumor.

$$\mathrm{RBE} = \frac{\mathrm{D}_\gamma}{\mathrm{D}_{\mathrm{test}}} \tag{1.3}$$

Most often, the radiation quality of charged particles is described in terms of their **L**ineal **E**nergy **T**ransfer (LET), the absolute value of which is identical to their electronic stopping power and it is measured in $\mathrm{keV}\cdot\mu\mathrm{m}^{-1}$. As presented in Figure 1.5 the RBE is almost a unique function of the LET though a significant dependence on particle type has also been observed in radiobiological experiments. In particular low-LET radiation will produce sparsely energy deposition in a uniform way across the whole cell, with low energy imparted to sensitive structures. This kind of damage can be easily repaired by the cell itself, thus resulting in a low RBE. In contrast, high-LET radiation tends to interact in a highly not homogeneous pattern, with regions with high energy imparted alternated to regions with almost no interactions. The higher density of energy imparted usually leads to un-fixable damages, for example multiple strand breaks in the DNA, increasing the killing efficacy of this type of ionizing radiation.

As presented in Figure 1.5, the RBE shows a maximum in the LET region between 100 and 200 $\mathrm{keV}\cdot\mu\mathrm{m}^{-1}$, then it decreases. This is due to the so-called *overkill effect*, in which after a certain value of LET the energy deposited in the cell is larger than that needed for inducing lethal damages, thus an increase of LET is no longer decreasing the survival fraction of the cell population, leading to a reduction in biological effectiveness.

It should be observed that both the absorbed dose D and the LET are average quantities that can not describe the stochastic aspects of the radiation interaction, therefore they are both inadequate for an accurate prediction of the radiobiological effects. The microdosimetric approach is a more reliable method, that offers both computational and experimental instruments to characterize the radiation quality.

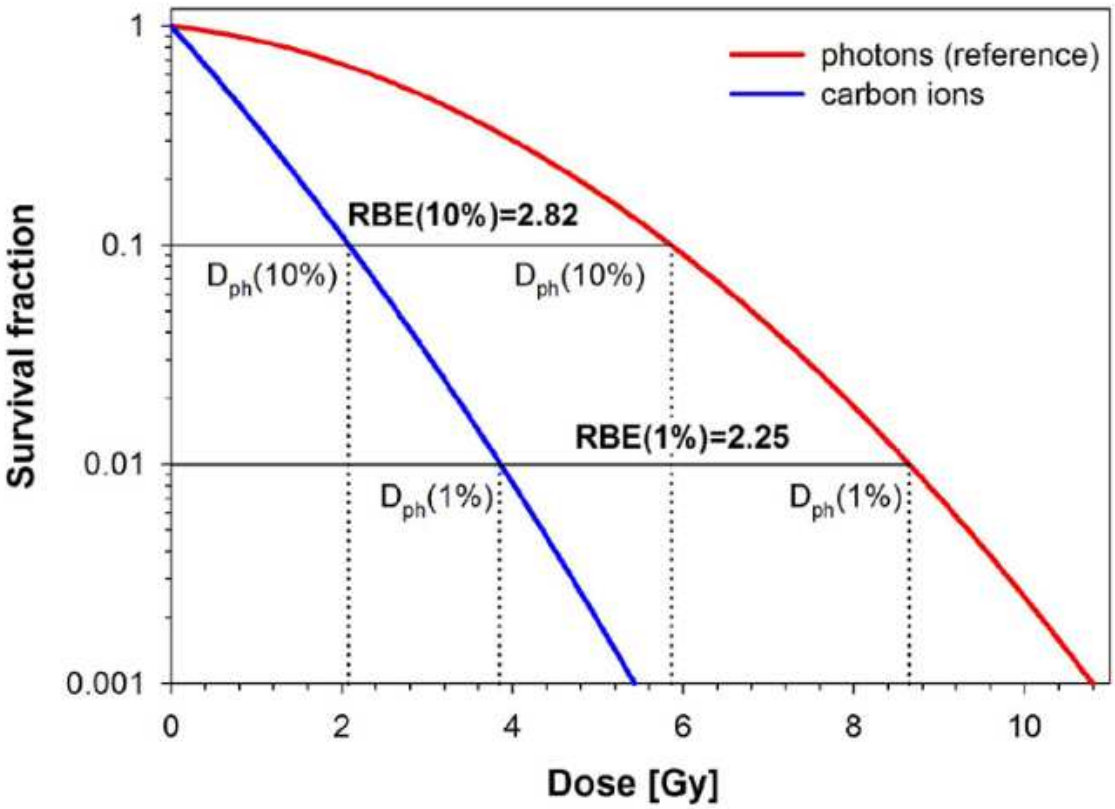

Figure 1.4: Survival fraction of a cells population as function of the dose for photons (red) and carbon ions (blue) [8].

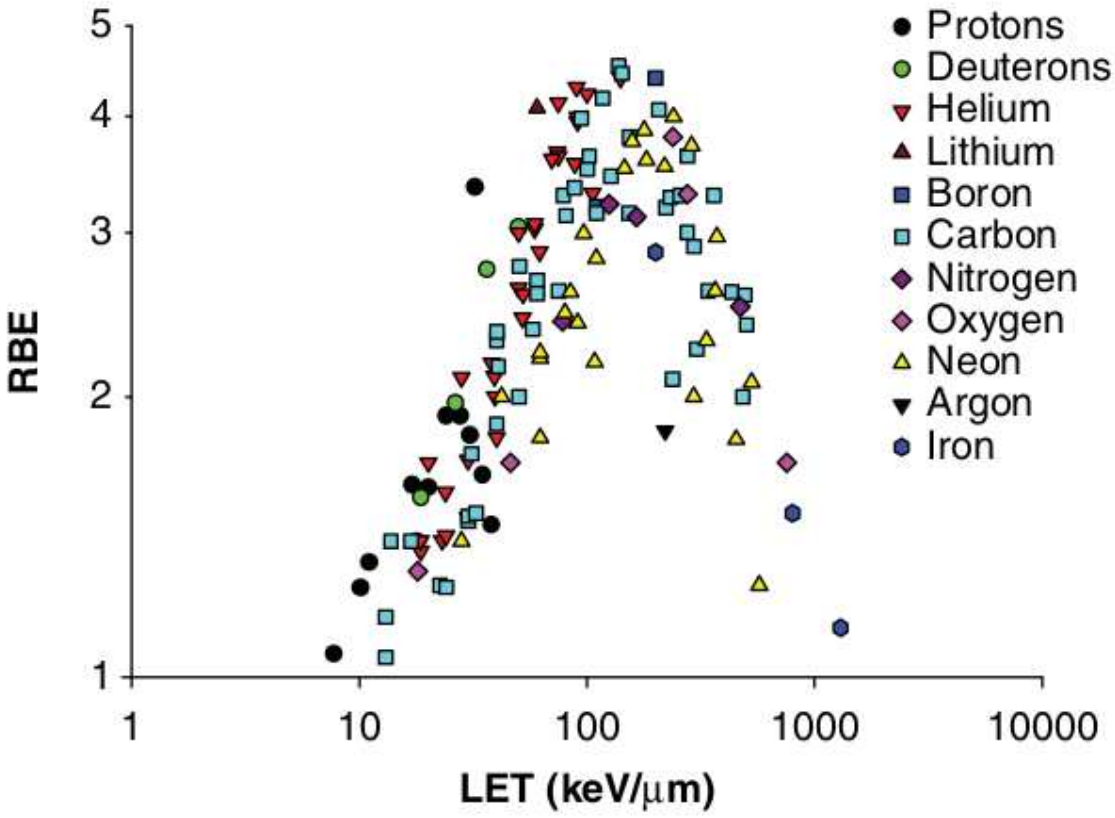

Figure 1.5: Relation between RBE and LET for different radiation qualities [9].

1.3 Microdosimetric Quantities

The definitions of microdosimetric quantities are stated in the **I**nternational **C**ommission on **R**adiation **U**nits and **M**easurements (ICRU), report no. 16, *Microdosimetry*, published in 1983 [10]. As described before, microdosimetry studies the stochastic quantities related to the energy deposition process due to the interaction of ionizing radiation in target volumes of micrometric size.

The imparted energy ϵ is defined as the sum of all the energy deposits occurring in the volume, hence

$$\epsilon = \sum_i \epsilon_i \tag{1.4}$$

From the ICRU, the definition of ϵ_i is

$$\epsilon_i = T_{in} - T_{out} + Q \tag{1.5}$$

where T_{in} is the kinetic energy of the impinging particle without considering its rest mass, T_{out} is the sum of the kinetic energy of all the particles involved in the interaction after it has occurred and Q is the variation of the rest energy of the involved particles, since in case of nuclear reaction or pair production the process can release ($Q > 0$) or absorb ($Q < 0$) the energy. The discrete point in which ϵ_i is released is called *transfer point*.

The stochastic equivalent of the absorbed dose is called *specific energy*, z, defined as the ratio between ϵ by m, being ϵ the energy imparted by ionizing radiation to matter of mass m.

$$z = \frac{\epsilon}{m}\ [\mathrm{Gy}], \quad 1\ \mathrm{Gy} = 1\ \mathrm{J \cdot kg^{-1}} \tag{1.6}$$

Since z is a stochastic quantity, a corresponding distribution function needs to be defined. Named the distribution $F(z)$, its value is, by definition, the probability that the specific energy of an event is equal to or lower than z. The derivative of $F(z)$ represents the **P**robability **D**ensity **F**unction (PDF) of z, defined as

$$f(z) = \frac{\mathrm{d}F(z)}{\mathrm{d}z} \tag{1.7}$$

From the PDF one can retrieve its expectation value, which is a non-stochastic quantity, called *mean specific energy*

$$\bar{z} = \int_0^\infty z \cdot f(z)\ \mathrm{d}z \tag{1.8}$$

Another useful microdosimetric quantity is the *lineal energy*, defined as

$$y = \frac{\epsilon}{\bar{l}}\ [\mathrm{J{\cdot}m^{-1}}] \tag{1.9}$$

in this case ϵ represents the energy imparted by a single energy-deposition event to the matter in a volume and $\bar{l}$ is the mean chord length, for randomly oriented chords, of the volume. The most common unit of measure for y is $\mathrm{keV{\cdot}\mu m^{-1}}$. According to one of Cauchy's theorems [11] the mean chord length of a convex body of surface S and volume V can be evaluated as

$$\bar{l} = 4\frac{V}{S} \tag{1.10}$$

and it represents the mean length of the trajectories of randomly oriented particles crossing the volume.

As the specific energy, y is also a stochastic quantity, related to the PDF $f(y)$. Its mean value is the *frequency-mean lineal energy*

$$\overline{y_{\mathrm{F}}} = \int_0^\infty y \cdot f(y)\ \mathrm{d}y \tag{1.11}$$

In addition, the dose probability density of y has also been defined to represent the fraction of the absorbed dose for an event with lineal energy between y and $y+\mathrm{d}y$. The mean value of this distribution is the *dose-mean lineal energy*

$$\overline{y_{\mathrm{D}}} = \int_0^\infty y \cdot d(y)\ \mathrm{d}y \tag{1.12}$$

From the definitions one can extract the relations between $f(y)$ and $d(y)$, and between their mean values

$$d(y) = \frac{y \cdot f(y)}{\overline{y_{\mathrm{F}}}} \tag{1.13}$$

$$\overline{y_{\mathrm{D}}} = \frac{1}{\overline{y_{\mathrm{F}}}} \int_0^\infty y^2 \cdot f(y)\ \mathrm{d}y \tag{1.14}$$

It is immediate that the in the limit of small volume, the mean specific energy $\bar{z}$ is equal to the absorbed dose D:

$$D = \lim_{z \to 0} \bar{z} \tag{1.15}$$

The relation between LET and linear energy is far more complex and the LET is not simply the average value of the $f(y)$ distribution. The LET is defined as the mean energy transferred by an ionizing particle by means of electronic collisions in a distance $\mathrm{d}x$, crossing a medium of infinite extension. It is always centered on the primary particle track, and it includes the energy carried by all secondary electrons. Conversely, the lineal energy measures the energy released in a small and defined volume by particles directly crossing the volume or passing nearby (and interacting with the target volume via secondary electrons [12]). In addition, it is subject to a geometrical cut-off [7], because energetic electrons can escape the volume and deposit their energy out of it.

1.4 Experimental Microdosimetry

1.4.1 Graphical Representation of Microdosimetric Spectra

In a typical microdosimetric spectrum the lineal energy can span among several orders of magnitude, due to the complexity of radiation fields and the variety of processes involved. In order to represent the data as clearly as possible, the usual representation is made in semi-logarithmic scale, with the lineal energy y in logarithmic scale on the x-axis and, the quantities $yf(y)$ and $yd(y)$ in linear scale on the y-axis. In this representation equal areas under the curve correspond to equal frequency (or dose) fractions, with respect to the total. In fact

$$\int_{y_1}^{y_2} f(y)\ \mathrm{d}y = \int_{y_1}^{y_2} yf(y) \frac{\mathrm{dy}}{y} = \int_{y_1}^{y_2} yf(y)\ \mathrm{d}(\ln(y)) \tag{1.16}$$

Figure 1.6 and Figure 1.7 show examples of microdosimetric spectra measured in a neutron field, achieved in the ^{7}Li(d,n)^{8}Be reaction produced with a deuterium beam at 5.5 MeV impinging on a thin LiF target, and for low energy protons obtained degrading a 70 MeV clinical proton beam in a tissue-equivalent phantom. The frequency and dose mean values of the lineal energy are also shown in the figures.

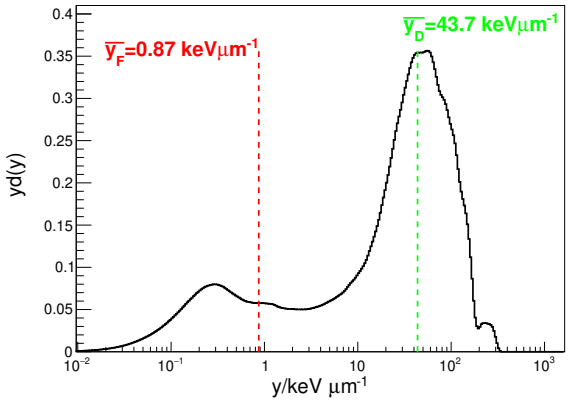

Figure 1.6: The $yd(y)$ spectrum and mean values for a 4 MeV neutron field.

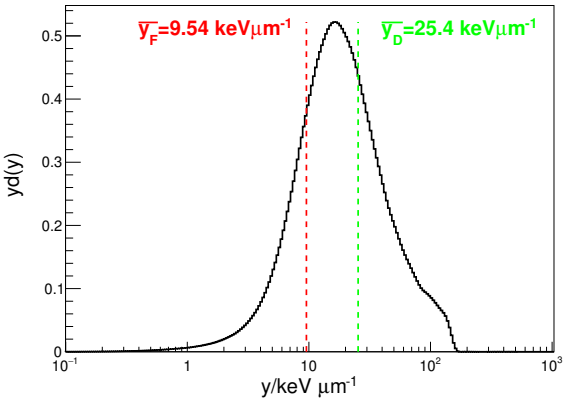

Figure 1.7: The $yd(y)$ spectrum and mean values for a low energy proton field.

In particular, in the neutron field spectrum shown in Figure 1.6 three main regions of LET can be distinguished:

1. Low LET events: below 10 keV·μm^{-1}. This region mainly contains contributions from secondary electrons produced by Compton scattering of prompt γ-rays coming from neutron reactions with the detector walls.
2. Intermediate LET events: from 10 to 171 keV·μm^{-1}. In this region there are the contributions of recoil protons, generated by elastic collision of neutrons in the detector walls. The maximum value is 171 keV·μm^{-1} [13], which corresponds to the maximum energy imparted by a proton in 1 μm of equivalent biological tissue.
3. High LET events: above 171 keV·μm^{-1}. The last part of the spectrum is due to charged particles, heavier than protons, originating from inelastic nuclear reactions, as (n,α), and heavy recoil nuclei.

1.4.2 RBE Assessment

Despite the physical mechanisms of the interaction between radiation and matter are well known and have been largely studied in the last century, the processes through which the ionizing radiation causes a biological damage on a microscopic scale are still up to debate. As discussed in the introduction paragraph, it has been demonstrated that even at equal dose, different radiation qualities cause different biological effects [14]. Microdosimetry can be exploited for assessing the radiation quality, both for radiation protection and radiation therapy purposes, since the microdosimetric spectra are sensitive to the composition of the field. In general microdosimetric data are also more reproducible than biological ones and easier to obtain. If the set-up is calibrated on a specific biological end-point, the microdosimetric distributions of the lineal energy can be used to predict the RBE of complex and unknown radiation fields, by using a biological weighting function of the lineal energy, $r(y)$:

$$\mathrm{RBE}_\mu = \int_0^\infty r(y)d(y)\ \mathrm{d}y \tag{1.17}$$

The subscript μ is used to distinguish the microdosimetric estimation from the direct biological measurement of RBE. The biological weighting function can be numerically determined on empirical and statistical bases using the results of a RBE-microdosimetry intercomparison study [15].

The final uncertainty on the RBE_μ depends on the uncertainties on $d(y)$ and on the biological data, aside from the one of the weighting function. The main contributions on the uncertainty of microdosimetric data are the calibration procedure of the spectrum in lineal energy y and the detector efficiency and resolution. A widely used weighting function for neutrons and protons is presented in Figure 1.8 [16]. From the shape of $r(y)$ three main regions can be identified:

1. Below 10 $\text{keV}\cdot\mu\text{m}^{-1}$: a plateau in which the weighting function is constant and approximately equal to 1.

2. Between 10 and 70 $\text{keV}\cdot\mu\text{m}^{-1}$: the peak in $r(y)$ describes an enhancement in the ability to cause biological damage.

3. Above 70 $\text{keV}\cdot\mu\text{m}^{-1}$: the reduction of $r(y)$ after a certain value of LET is due to the overkill effect, for which higher values of y do not contribute anymore to the biological damage.

In Figure 1.9 a set of biological RBEs is shown as a function of depth in the ocular tissue, in addition to the microdosimetric RBE_μ. It can be observed that, both radiobiological data and microdosimetric predictions describe an increase of the RBE at large penetration depths, where the energy of the primary particle decreases and the LET increases, and in particular in the fall-off region of the dose profile (last millimeters of the primary particle range), just beyond the Bragg peak, the point of maximum energy release before the primary particle stops. For example, the RBE values shown in Figure 1.9 increase from 1.1 in the entrance region (shallow depths) to about 2 in the position corresponding to 50% of the maximum dose reaching values up to 3 in the last millimeters of their range beyond the tumor. These experimental findings are in contrast to the present assumption in clinical treatment planning of a constant RBE=1.1 at any penetration depth. The effect of not taking into account this augmented biological effectiveness in the region behind the tumor could result in underestimated side effects and normal tissue complications following the radiation treatment.

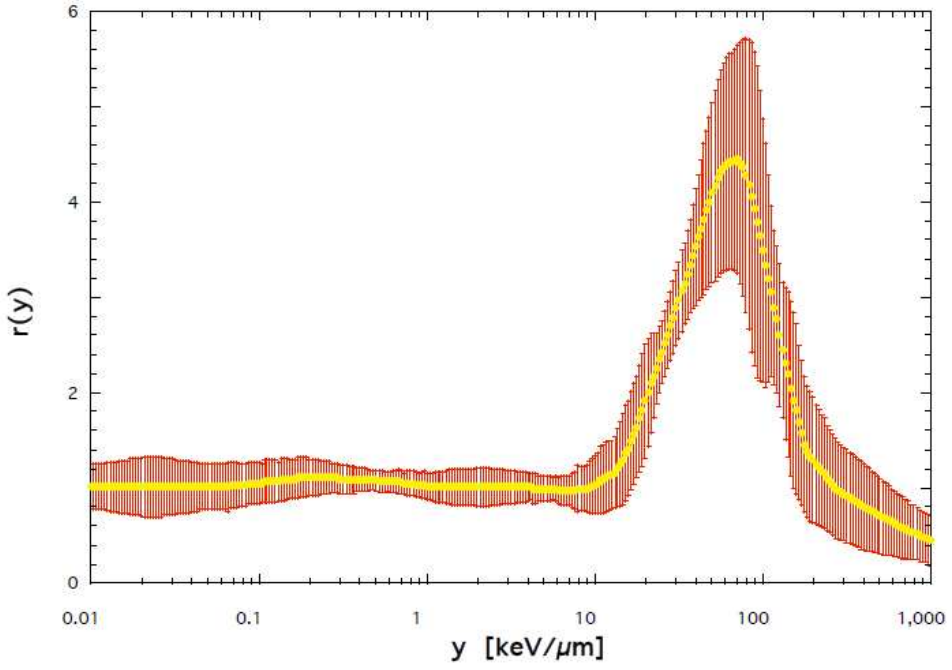

Figure 1.8: Biological weighting function and uncertainties for intestine damage in mice exposed at 8 Gy.

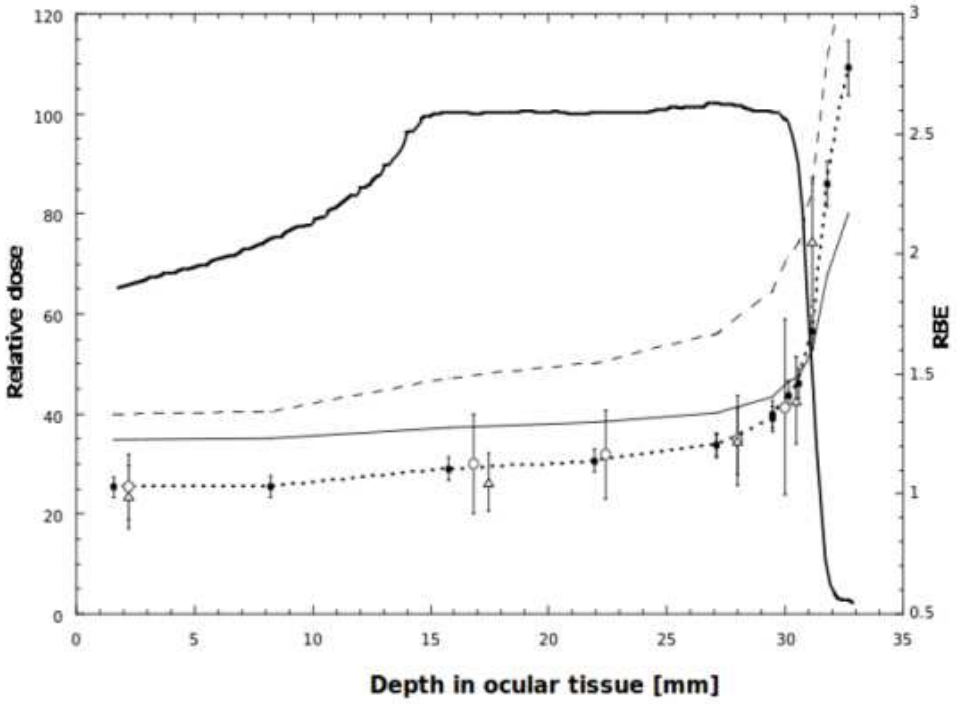

Figure 1.9: Comparison between microdosimetric and radiobiological RBEs [17]. The full line is the proton **S**pread **O**out **B**ragg **P**eak (SOBP), the open symbols represent the radiobiological RBEs for different human tumor cells treated with different doses. The dotted line with filled symbols is the RBE_{μ} evaluated by Loncol et al. [16].

Another approach to correlate microdosimetric data and biological effects is provided by the **M**icrodosimetric **K**inetic **M**odel (MKM) [18]. The MKM relates the cell survival probability after irradiation, S, to the number of lethal lesions caused by the ionizing radiation field, L, and the dose-mean lineal energy measured in the same field with microdosimetric techniques. Moreover, the model can take into account the overkill effect using the saturation-corrected lineal energy y^* [19]. The relation between L and the dose is in agreement with the linear-quadratic model, in which a lethal lesion can arise from the combination of two sub-lesions or directly from an un-repaired complex lesion, thus including a quadratic and a linear terms, respectively.

$$S = \exp(L) = \exp(-\alpha D - \beta D^2) = \exp\left[-\left(\alpha_0 + \frac{\beta}{\rho \pi r_d^2} y^*\right) D - \beta D^2\right] \tag{1.18}$$

1.4.3 Detectors for Microdosimetry

One of the most used type of detector in microdosimetry is the **T**issue **E**quivalent **P**roportional **C**ounter (TEPC) [20]. These detectors allow to simulate cylindrical or spherical micrometric tissue volumes, with assumed density 1 g cm^{-3}, using a millimeter-size active volume filled with a low-density gas. In order to obtain the tissue-equivalence property, since the ionizing particles energy transfer depends on the atomic composition of the medium rather than on the chemical combination, both the construction materials and the gas are realized by compounds rich in hydrogen, carbon, nitrogen and oxygen to mimic the tissue elemental composition [21]. The most used material for the construction of a TEPC are the Rexolite for the insulators, and the conductive plastic A-150 [10] for the wall of the detector used as cathode, while the gases used are usually methane or propane-based tissue equivalent mixtures. The possibility to use as a measuring gas the pure propane has also been demonstrated [22], with the advantages of being more stable with time.

The pressure of the gas needs to be adjusted in such a way that the crossing ionizing particle deposits the same amount of energy as it would do in a real micrometer-sized volume of tissue. This can be achieved considering the mean energy loss ΔE as function of the mass stopping power S/ρ, the density and the volume, in the following the index t stands for tissue and g stands for gas:

$$\Delta E_t = \left(\frac{S}{\rho}\right)_t \rho_t d_t = \left(\frac{S}{\rho}\right)_g \rho_g d_g = \Delta E_g \tag{1.19}$$

Hence, assuming the diameter of the gas sphere $d_g = k \cdot d_t$, and the stopping powers the same, from this the importance of tissue-equivalence materials, it can be obtained

$$\rho_g = \frac{\rho_t}{k} = \frac{1 \text{ g·cm}^{-3}}{k} \tag{1.20}$$

Therefore the requirement for a TEPC to simulate a tissue site of diameter d_t, provided that the filling gas has the same elemental composition as tissue and as a consequence the same mass stopping power, is that the ratio between gas and tissue densities is equal to the ratio between tissue sphere diameter and the gas cavity diameter. In this way it is ensured that the mean energy losses in the gas and in the real tissue are the same. Reducing the density of the gas in the TEPC it is possible to simulate volumes with diameters of the order of the micrometers, down to tens of nanometers. Exposing the detector to ionizing radiation and studying the energy deposition patterns in such scales, it is possible to analyze the correlation between microscopic and nanoscopic characteristics of radiation interaction and the corresponding biological effects at the cellular and subcellular levels.

Alternatively to TEPC, solid-state based detectors have been recently developed for microdosimetric applications. In particular, silicon and diamond **S**olid **S**tate **D**etectors (SSDs) have been successfully applied to microdosimetry, since they are more robust and easier to operate than TEPCs [23–27]. The main advantage of solid-state microdosimeters is that they can be reduced in size, with the single pixel as small as about 10 μm, so that they can easily sustain the high fluence rate typical of proton and carbon ion therapy. In addition the single pixels can be assembled in a regular matrix, allowing for a 2D monitoring of the radiation field.

However these qualities come at a cost, since for a semiconductor-based SSD the active volume depends on the physical size of the device and cannot be modified. In addition, the **S**ignal-to-**N**oise ratio (SN) is proportional to the thickness of the detector, hence very thin sensitive volumes, as the one needed in microdosimetry, inevitably lead to poor SN and low sensitivity compared to the ones of a typical proportional counter [28], in which the intrinsic amplification caused by the charge avalanche development allows a better discrimination between signal and noise. Another drawback of SSDs is their sensibility to radiation damage, which can lead to a loss of resolution caused by displacement of atoms in the crystalline structure of the detector's bulk [29]. Moreover, they are not tissue equivalent and for this reason the acquired spectra must be corrected for the ratio of the mass stopping power in the SSD material and tissue which is not always a straightforward process since the ratio varies with the type and energy of the interacting particles.

1.4.4 Operating Principles of TEPCs

A gas chamber working in the proportionality regime is called proportional counter [4]. The measured physical quantity is the charge released by ionizing interactions of the impinging ionizing particle, amplified by the gas avalanche process, and collected at the anode. In the proportional regime, the collected charge is proportional to the initial number of ionizations produced. By using the so-called *W-value*, the mean energy expended per electron-ion pair produced, the number of ionizations can afterwards be translated into energy imparted. One of the common shapes for a proportional counter is shown in Figure 1.10, and it consists of a cylindrical cathode and coaxial thin anode.

In case of a TEPC the anode has a typical diameter between 25 and 100 μm, and it is usually made of golden-plated tungsten in order to endure the mechanical tension required. The cathode is usually made of A-150 plastic, a conductive and tissue-equivalent material.

Once the bias voltage has been supplied, given the cylinder radius r_c and the anode one r_a, an electric field is produced inside the volume, with an absolute value

$$E(r) = \frac{1}{\ln(r_c/r_a)} \frac{V_A - V_C}{r} \tag{1.21}$$

A low electric field is necessary to avoid the re-combination of electron-ion pairs after the ionization events, and to drift the charges toward the electrodes. Moving toward the anode the electric field increases, and at a certain position it is high enough to accelerate the electrons at such speed that they can produce further ionization by colliding with other electrons in the gas, producing an avalanche. An example of avalanche is shown in Figure 1.11. Under this configuration a single electron undergoes an avalanche process resulting in a large number of electrons collected at the anode. [4], hence enhancing the SN ratio and the capability of the device to detect low-ionization events, in addition to an improved resolution at low energies. However if the electric field is too strong the avalanche may suppress itself, due to the counter-electric field produced by the electrons, losing in proportionality. A typical gas gain in TEPCs is between 500-1000.

Two main aspects are of crucial importance while working with TEPCs:

1. The gas gain must be stable and independent of particle type and energy.
2. The gas avalanche should be confined to a small region around the central anode, to avoid loss of energy resolution.

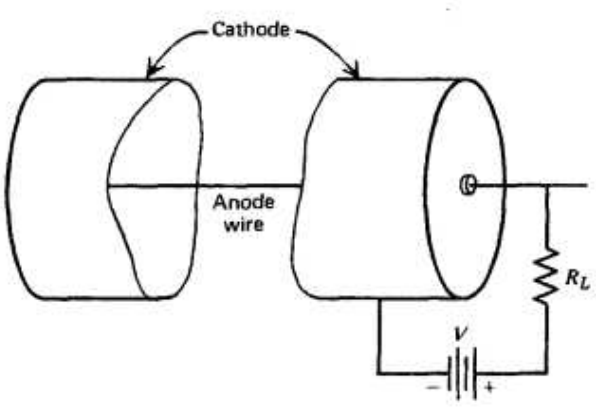

Figure 1.10: Schematic representation of a cylindrical proportional counter [4].

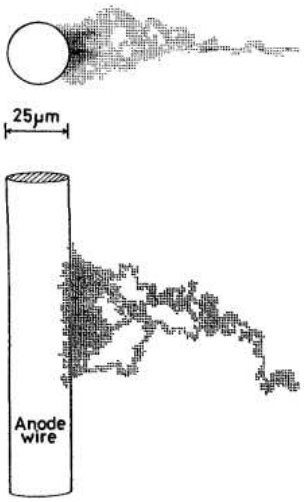

Figure 1.11: Depiction of the avalanche development around the anode wire [4].

Chapter 2

Experimental Setup

2.1 Mini-TEPCs

Miniaturized TEPCs have been developed at INFN-LNL, for specific applications in hadrontherapy [30]. The miniaturization of the sensitive volume allows the TEPC to be operable in the very intense beams typical of hadron-therapy (the average fluence rate in proton therapy is about 10^7 cm^{-2} s^{-1}).

The first version of these mini-TEPCs, and for many years, has been operated in gas flow modality to prevent gas gain instability due to gas deterioration and to facilitate the change of site size for research purpose. More recently, an upgraded mini-TEPC has been developed, able to operate without gas flow [31, 32]. As a result of several measurement campaigns it has been proven that this mini-TEPC response is reproducible and stable over 1 year within approximately a 5% uncertainty on $\overline{y_F}$ and $\overline{y_D}$ [33].

As an result of this test of reproducibility and repeatability of a prototypal detector, five innovative mini-TEPCs, named from *MIKRO-1* to *MIKRO-5* have been produced with engineered construction techniques and assembly procedures, in the experiment *4MiCA*, "complete setup 4 Microdosimetric Clinical Assessment", a project funded by the Technological Transfer of INFN, in the framework of the Research for Innovation call (R4I-2021).

During this thesis work these detectors have been characterized in different radiation fields and their response function studied under different point of view.

The active volume of the detectors consists of a cylindrical cavity of 1 mm both in diameter and height, drilled from a cylinder of A-150 tissue-equivalent conductive plastic with 3 mm diameter and 5 mm height. The anode consists of a 25 μm thin wire, made of golden-plated tungsten. The conductive plastic acts as cathode and during the operation of the device it receives a variable bias between -700 V and -850 V, while the anode wire is set to 0 V. All the components are kept in position by a protective cylinder of Rexolite, which is in turn inserted in a 200 μm thick aluminum cylinder, useful for electromagnetic shielding and vacuum sealing.

As discussed before, the build-up of charge inside the active volume tends to generate a counter-electric field, leading to an instability of the gain. To prevent this effect an additional pair of electrodes, known as *guard tubes*, have been placed coaxial to the anode wire. The project schematics of the detectors are shown in Figure 2.1, while a picture of an assembled detector is presented in Figure 2.2.

All the detector components have been engineered in order to construct them in series using as much as possible numerical control machines with the aim of minimizing the variability of each component for the five detectors. Before the assembly, all the components have been washed from the residuals of the processing using ultrasound cleaning, rinsed with distilled water and left to dry for some days in a vacuum chamber in order to remove as much as possible the remaining molecules of water.

The assembly procedure has also been carefully studied to minimize the time needed to have a complete assembled detector and reducing the risk of damaging the pieces during the procedure. The detectors have also been developed improving their robustness so as to make their transport easier. In Figure 2.3 an overview of the five detectors assembled and placed in their aluminum case, the front-end electronics will be connected directly to the three pins that can be observed in the same picture on the basis of the holder of the detectors.

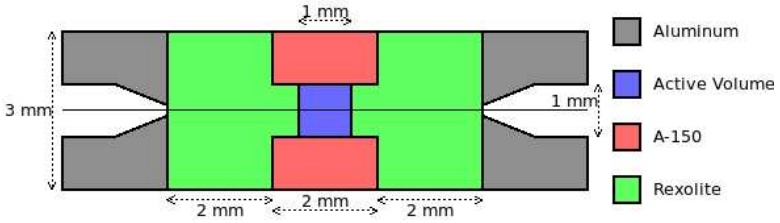

Figure 2.1: Schematics of the mini-TEPC.

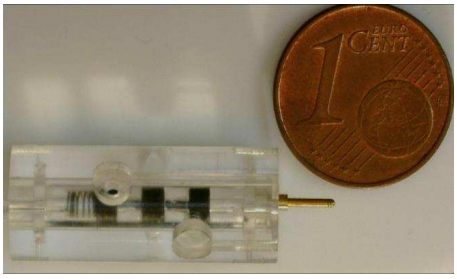

Figure 2.2: A picture of the detector, one cent coin for scale.

Figure 2.3: A picture of the five assembled prototypes.

2.2 Read-Out Chain

2.2.1 Analog

The analog read-out chain used to process the signals from the detectors is schematized in Fig. 2.4a. The detector is connected to a charge-sensitive preamplifier, which also passes the bias provided by the power supply module. The pre-amplifier, namely *4MiCA-V1*, has been specifically developed for microdosimetric measurements, therefore it presents two outputs, one with a x1 amplification factor and one providing a x10 amplification factor.

Since this preamplifier is a new prototype, its performances have been compared with two commercial charge sensitive preamplifiers, the *142* and *142PC* by *EG&G ORTEC*. In addition, the first prototype of custom preamplifier, *4MiCA-V0*, has been tested.

The output signals from the preamplifier are then sent in parallel to two different shaping amplifiers, the *SA - 672* and *SA - 673* by *EG&G ORTEC*, providing the gaussian shaping and further amplification. The amplifier serves two functions in the analog electronic system, adjusting the signal amplitude to match the input range of the multichannel analyzer and maximizing the signal to noise ratio by minimizing the frequency range of the output signal [4]. Limiting the frequency range essentially filters out the components of the preamplifier noise at higher and lower frequencies.

To cover five orders of magnitudes of the input signals, various gains can be set from the front panel. The shaping time can be chosen in a range from 0.25 to 6 μs, depending on the expected rate of events. The longer the shaping time the lower the overall electronic noise but long integration times also limit the maximum usable count rate by increasing the probability of pulse pile up.

The peak sensing **A**nalog to **D**igital **C**onverter (ADC) determines the peak height of the signal and converts it to a channel number in a digital format. For this thesis work the two channel **M**ulti **C**hannel **A**nalyzer (MCA) *ASPEC-MCA-972* by *EG&G ORTEC* has been used. Both the **H**igh-**L**et (HL) and the **L**ow-**L**et (LL) channels are digitized using 14-bit precision, hence each sub-spectrum will present $2^{14} = 16384$ channels.

To calibrate the electronic chain, converting the ADC channels to volts in order to be able to join the two sub-spectra offline, a pulse generator has been connected to the test input of the preamplifier. The module, *DT5800D* by *CAEN*, is controlled via software and it provides a signal with a similar shape to the one generated by the detector, also allowing to control the rise time, the decay constant and the amplitude.

2.2.2 Digital

In recent years the development of high speed, high resolution, ADCs has led to an alternative approach to data acquisition. These ADCs are commonly used as the input stage of digital oscilloscopes. In principle, the digital footprint of a preamplifier output can be stored for later offline analysis of pulse heights. However, the large amount of data produced would overload most data storage and processing systems. The volume of data recorded for offline analysis can be reduced by storing the ADC output in a first in/out buffer memory and monitoring, in real time, for samples above a preset threshold level. To further reduce the amount of data which must be transferred and to eliminate the need for offline processing a **D**igital **P**ulse **P**rocessor (DPP) and histogramming memory can be added. The resulting instrument can be used to replace the shaping amplifier and the peak sensing ADCs but can also be programmed to perform additional data analysis functions. The digital pulse processing stage typically utilizes firmware implemented in a **F**ield **P**rogramable **G**ate **A**rray (FPGA) to recognize pulses, construct a shaped pulse, and detect the peak height of that pulse.

In this work the Dual Digital MCA model *DT5780* by *CAEN* has been used for part of the tests, whose firmware produces a trapezoidal shaped pulse which gives slightly better noise reduction than the gaussian shaping used in analog shaping amplifiers. This digital read-out chain is sketched in Fig. 2.4b. The idea behind this investigation is trying to move towards a more compact setup, and to investigate if the performances of the digital electronic chain are comparable to those of the standard analog chain.

The *DT5780* module has also two high voltage power supplies of fixed polarity, one negative and one positive in the one used. The maximum output is ± 5 kV and the maximum current is 300 μA with SHV connectors. The *CAEN DT5780* connects to the PC using both USB 2.0 or an Optical Link interface. The signals coming from the preamplifier are sent into a fast amplifier, which modifies the amplitude without changing the shape, and then directly to the digitizer.

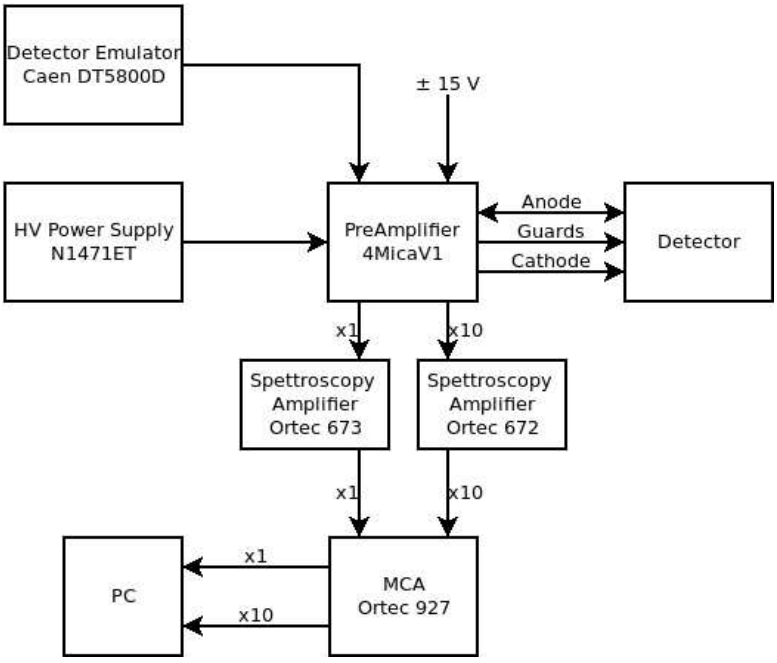

(a)

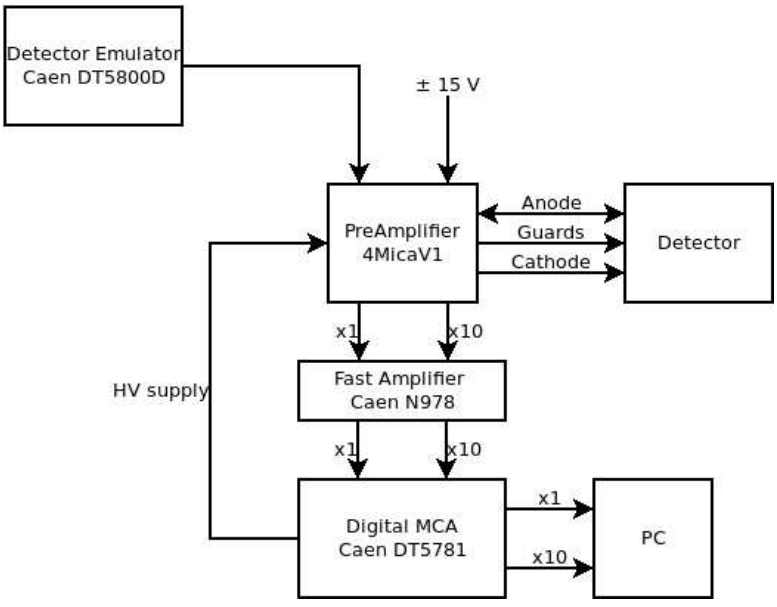

(b)

Figure 2.4: Schematic representation of the analog (a) and digital (b) electronic chains

Chapter 3

Methods and Development of Analysis Software

The purpose of this thesis is not only the characterization of the new mini-TEPCs, but also to provide a user-friendly software for the analysis of the spectra to be implemented to the final set-up that has to be easy to be used by the non-expert user in the clinical center. A dedicated software has been developed, with the objectives of being as intuitive as possible, in order to be used by medical physicists in clinical practice and less dependent on the user choices (robustness).

The software, called **Mik**ro-**An**alysis (MikAna), has been written in C++, with a **G**raphical **U**ser **I**nterface (GUI) designed using the Qt framework [34]. The aspects related to the visualization of histograms, fit algorithms and other advanced mathematical procedures have been integrated in the program embedding the ROOT libraries from the CERN software [35].

In the following sections the aspects related to the analysis of a microdosimetric spectrum will be discussed, also presenting the logic and the behavior of MikAna, providing a step-by-step example of the analysis. For the demonstration, a neutron spectrum is used.

3.1 Main Window and Configuration

Once the program starts, the main window, reported in Figure 3.1, presents the options of starting a new analysis or to load one or more saved spectra.

In order to be as flexible as possible, there are almost no numbers hard-coded in the source files. Instead the program will load a configuration file which can be modified from the configuration window, shown in Figure 3.2, once the *config* button has been clicked. The most important parameters in this window are: the number of channels given by the ADC, the pre-defined path to the data folder and the range of the parameters for the Fermi-like function. The usefulness of these and other parameters will be discussed later in this chapter.

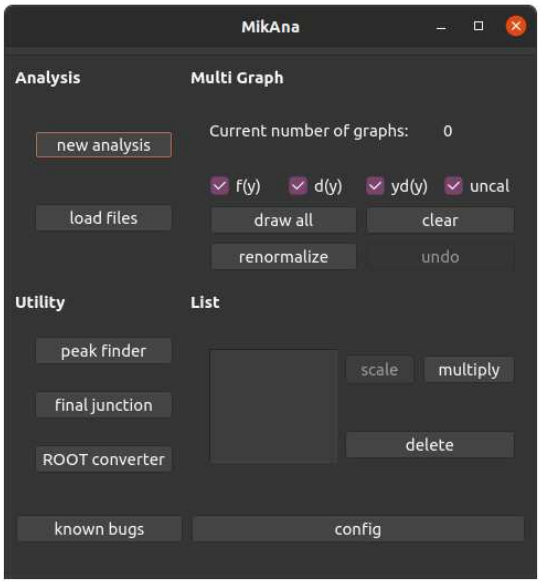

Figure 3.1: Main window of Mikana

Figure 3.2: The configuration window

3.2 The Analysis frame

The first step of a new analysis is to upload the two files corresponding to low-Let (LL) and high-LET (HL) sub-spectra. These files, provided by the ADC, contains the histograms in ASCII format. From the *File Structure* box in the configuration window the user can select the number of channels provided by the ADC and, in case, the number of lines that needs to be skipped before storing the data. Once the files have been uploaded the histograms can be shown clicking the *draw!* button, or the analysis can proceed with the calibration from ADC channels to volts.

The calibration is done through a linear regression, in particular a given pulse height in Volts can be correlated with the channel x via the linear relation:

$$y[\text{mV}] = q + m \cdot x[\text{channels}] \tag{3.1}$$

To perform the calibration there are two possible ways:

- Load a calibration file: a simple "`.txt`" files containing four columns, where the first two are the amplitude in voltage of the calibration signals and the corresponding centroids in channels for the LL spectrum, and the second two are the same for the HL spectrum
- Manually inserting the calibration coefficients for the two spectra

Note that in the first method the program will perform the linear fit of the calibration pulses, warning the user if the probability derived from the χ^2 of the fit is less than 90%. This check has been integrated to avoid copy-paste errors, but mostly to help the user to spot non-linearity in the electronic chain. Once the *calibrate!* button is clicked, the showed spectra are calibrated in millivolts and the analysis can proceed.

Examples of the analysis windows and the canvas are shown in Figures 3.3 and 3.4, respectively.

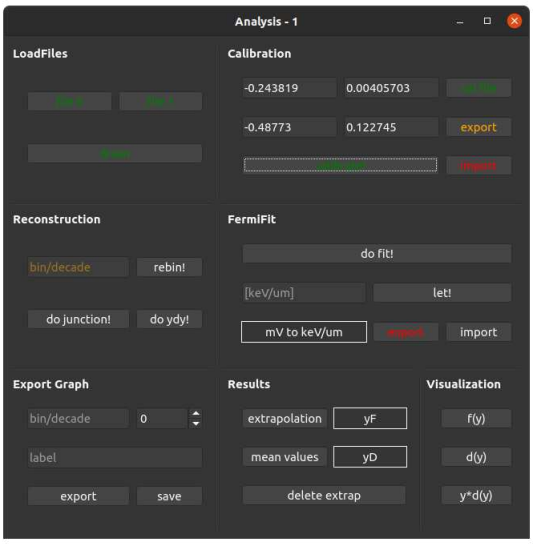

Figure 3.3: The analysis frame

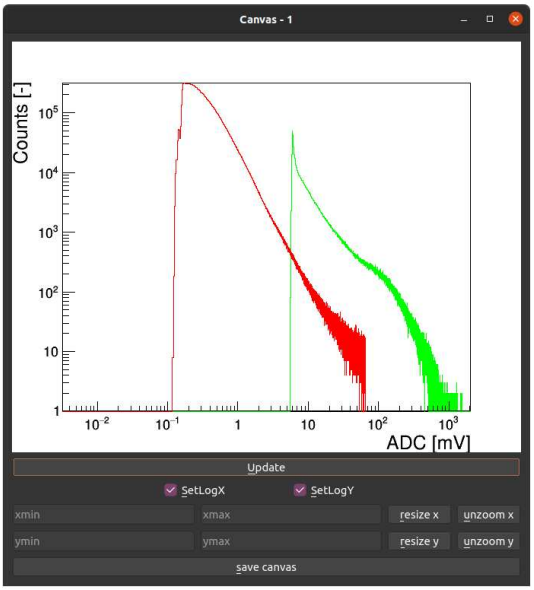

Figure 3.4: Canvas with LL spectrum (red) and HL spectrum (green) calibrated in mV

3.3 Peak Finder

As a utility feature, the software can generate the calibration file from channels to volts needed to perform the analysis. To produce the file the user can click the *peak finder* button on the main window, so that the peak finder frame can appear. In the frame, reported in Figure 3.5, the user is asked to load the calibration files for the two channels, which are expected to contain a series of calibration peaks, obtained for example with a pulser or detector emulator and acquired with the same **D**ata **A**cquisition **S**ystem (DAQ) as the measurements. After that the user can insert in the frame the values of the peaks in millivolts, one per line, and click on the *find peaks* button. The algorithm will then find the peaks, perform a gaussian fit, and assign the values inserted by the user to the centroid, as shown in Figure 3.6. Once the procedure has been completed for both channels, the user can click the *create file* button, type a name for the file and save it. This file is ready to be used in the analysis frame.

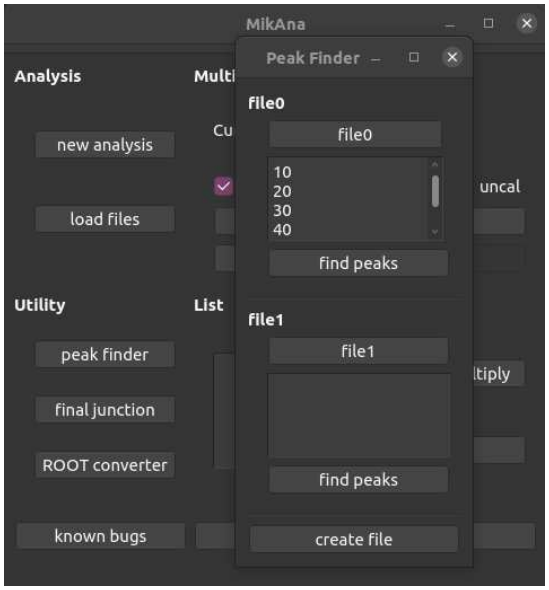

Figure 3.5: Main window with the peak finder pop-up.

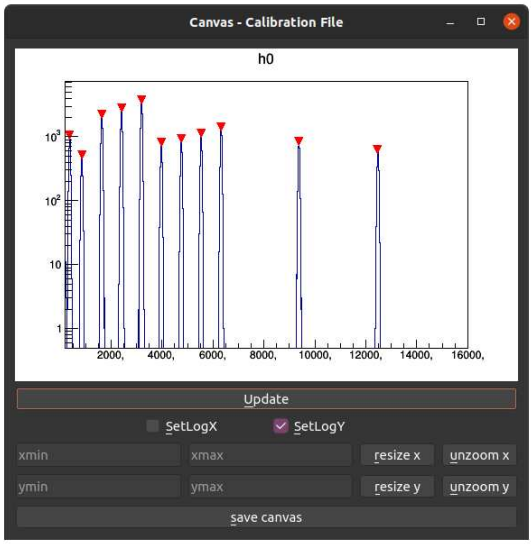

Figure 3.6: Calibration spectrum, the red triangles represent found peaks.

3.4 Logarithmic Rebinning and Junction

After the calibration procedure, the spectra are re-binned in logarithmic scale. The user is asked to insert the number of bins per decade, which will be referred as B. The number of decades, N, is 6 by default, but it can be changed from the configuration file, along with the starting point y_0. This implies that the edge of the i-th bin is given by:

$$y_i = y_0 \cdot 10^{\frac{i}{B}}, \quad y_0 = 0.01 \text{ mV}, \quad i = 0, \ldots, \text{N} \cdot \text{B} \tag{3.2}$$

The value of B has to be chosen high enough to avoid loss of resolution in the spectra, but keeping in mind that a value higher than the resolution of the ADC will produce empty bins and distortion.

The following step is to join the two re-binned spectra in one. Once the *do junction!* button is clicked, MikAna will automatically look for the overlap region of the spectra, normalize them to have the same height in that region and then create a new spectrum containing both LL and HL data. On the canvas are then shown the old histograms and the new one, together with a black line which represent the cutting point. This point is chosen to be as close as possible to the end of the LL sub-spectrum, to keep the higher resolution, however its position can be changed from the configuration window. The result of the junction is shown in Figure 3.8.

Observe that in the overlapping region, even if the raw number of counts is different between HL and LL, their ratio must remain constant, hence the sub-spectra must be parallel. This is because signals in the overlapping region are produced by the same ionization events in the sensitive volume, the only difference in the total amount of events can be due to the different dead times during the acquisition in the two ADCs. If the spectra are not parallel it can be due to an error in the calibration procedure or non-linearity problems of the electronic chains during the acquisition. To verify the condition of parallelism of the two sub-spectra, the program divides the region of overlap in ten parts, evaluates the ratio between the integrals of the sub-spectra in each part and then verifies the compatibility with a zero-grade polynomial. In case the data do not fulfill this test, a warning appears.

At the end, the $yd(y)$ spectrum is computed, and based on some characteristic features of the spectrum the calibration from mV to lineal energy can be performed.

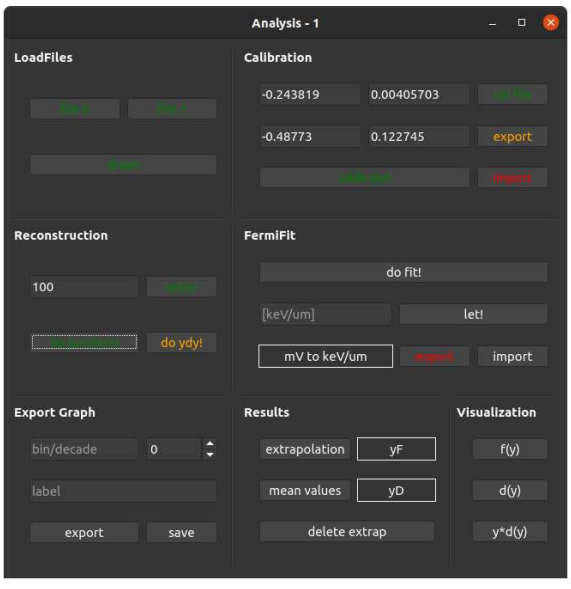

Figure 3.7: Analysis frame in the current step

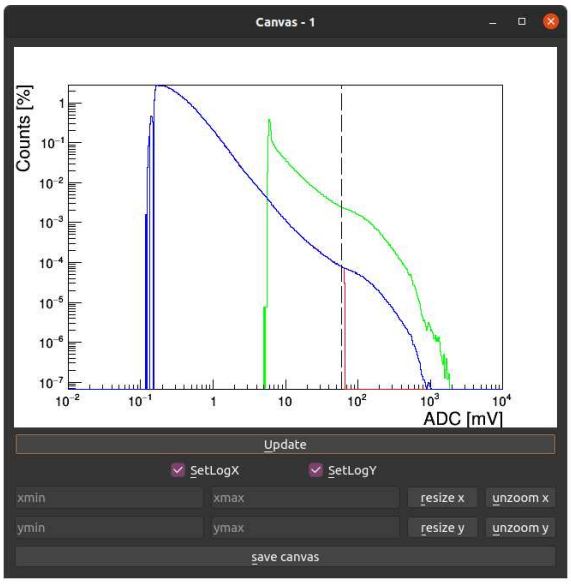

Figure 3.8: Canvas with the joined spectrum (blue) and the black line highlighting the junction point

3.5 Lineal Energy Calibration

Miniaturized TEPCs do not allow built-in calibration alpha-particle sources, and the lineal energy calibration of these counters must be performed using the proton or electron edge methods. These methods are based on the identification of a characteristic signature on the $yd(y)$ spectrum (a marker point) to which a defined lineal energy value can be ascribed [36–38]. In particular, if the spectrum contains a low-energy proton component (for example in a neutron or proton field), there can be a lineal energy drop in the $yd(y)$ distribution, corresponding to the maximum energy that protons can deposit in the gas-filled cavity of the mini-TEPC. When the sensitive volume diameter is smaller than the range of protons at maximum stopping power, the proton edge corresponds approximately to the maximum stopping power of protons in the given material. If the proton edge is not identifiable in the measured spectrum, as it may happen for a fast proton radiation field, a gamma source can be used instead, identifying the maximum lineal energy due to electrons (e-edge). The electron-edge is produced by those electrons that release all of their energy in the sensitive volume, when their tracks end exactly at its border. These electrons are called exact-stoppers.

To determine the marker position with good precision, the edge on the $yd(y)$ distribution is empirically parameterized by a Fermi-like function:

$$F(y) = \frac{A}{1 + e^{B \cdot y - C}} \tag{3.3}$$

where A is the highest value of the function and C/B is the position of the inflection point which will be used for the calibration. When the *do fit!* button is clicked a pop-up window will appear, as shown in Figure 3.9. This window presents two cursors trough which the user can select the range in which the fit will be carried out. In addition, two colored lines, representing the range of the fit, will appear on the canvas, moving according with the changes on the cursors. By default the cursors will appear at 60% and 10% of the peak maximum, in the falling edge region, as these values can be considered a good range for the Fermi fit. An example of the canvas before and after the Fermi fit is presented in Figure 3.10 and Figure 3.11.

Once the fit has been carried out, the user can insert the value in $\mathrm{keV}{\cdot}\mu\mathrm{m}^{-1}$ to be assigned to the inflection point to perform the calibration.

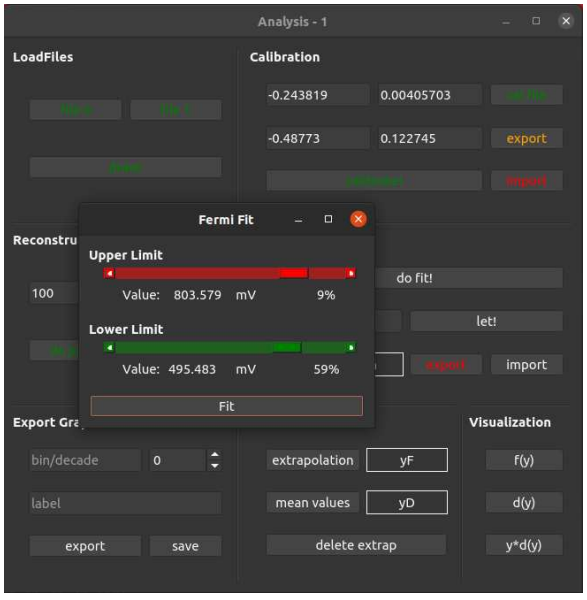

Figure 3.9: Analysis frame with the fit pop-up

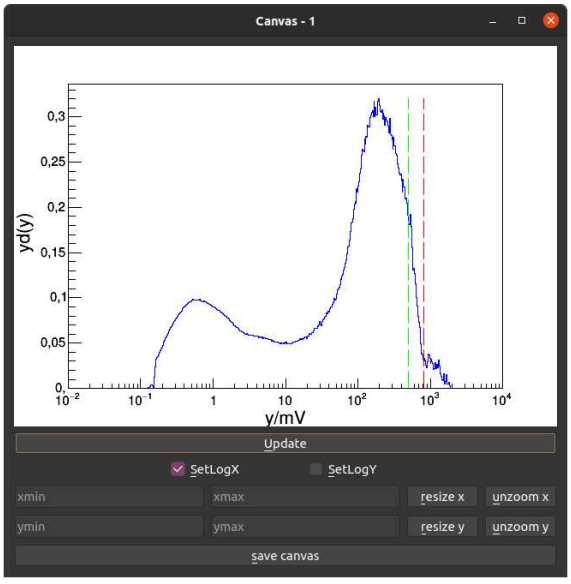

Figure 3.10: The $yd(y)$ spectrum with lines presenting the fit range

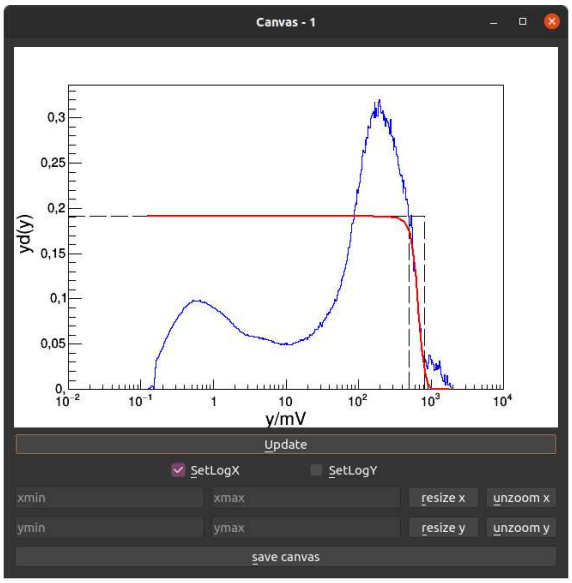

Figure 3.11: Canvas showing the $yd(y)$ with the Fermi fit on the proton edge

3.6 Extrapolation

The final step in the analysis consists in the extrapolation the spectra down to the minimum value of 0.01 keV$\cdot\mu$m^{-1}, corresponding approximately to the single ionization in tissue. This value has been chosen because the corresponding energy is 0.01 $\frac{\text{kev}}{1\mu\text{m}} \cdot 1\mu\text{m} = 10$ eV, which is the ionization potential, so the minimum energy needed to create an electron-ion pair.

As discussed in A. Bianchi, et al. [39], the extrapolation of the microdosimetric spectra to a common value of 0.01 keV$\cdot\mu$m^{-1} is strongly advisable because it significantly reduces the deviations in the mean values of the lineal energy distributions, due to different lower detection thresholds. The extrapolation procedure allows uniformity in data analysis and facilitate the intercomparison of data. Once the *extrapolation* button is clicked, a pop-up similar to the one of the Fermi-like fit will appear, as depicted in Figure 3.12, together with a moving line on the canvas, highlighting the extrapolation threshold, Figure 3.13. The user can then select the exact point to place the lower limit of experimental data. In principle the behavior of the spectrum below the detection threshold is unknown. However, if the threshold is not too high and there are not significant structures in this low-lineal energy region, a linear extrapolation can be performed as a first approximation. MikAna will fit the data contained in the next 10 bins after the preselected lower limit, however this fitting window of 10 bins can be changed in the configuration file. The linear fit is then used to create new bins below the threshold chosen by the user. The result of the extrapolation is presented in Figure 3.14.

Note that the extrapolation point is chosen on the $yd(y)$ spectrum, however the linear fit is performed on the $f(y)$ distribution and then the $d(y)$ and $yd(y)$ are re-evaluated.

The extrapolation is performed on the original data, not logarithmically binned, which in the meantime have been calibrated. This is done because the computation of the mean values defined before, $\overline{y_{\text{F}}}$ and $\overline{y_{\text{D}}}$, has been proved to be more precise on the non-compacted data, since the logarithmic re-binning implies a loss of resolution.

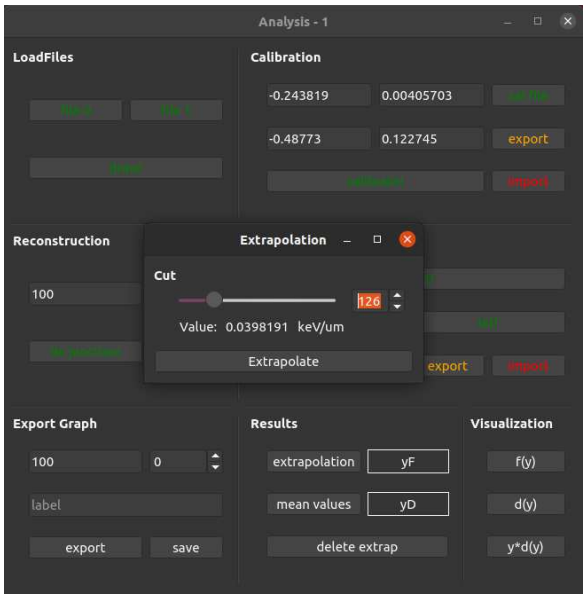

Figure 3.12: Analysis window with the selection of the extrapolation point

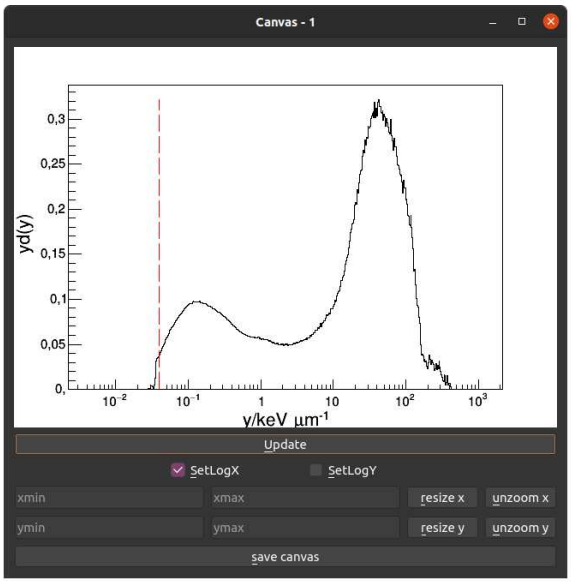

Figure 3.13: The $yd(y)$ spectrum calibrated in keV$\cdot\mu$m^{-1} and the line used for the extrapolation

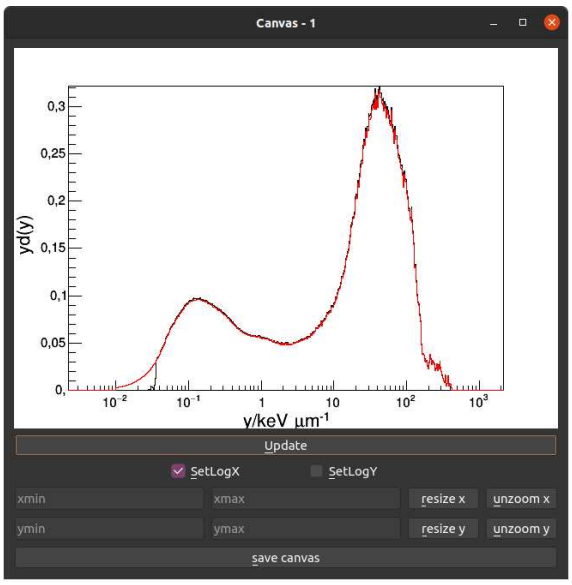

Figure 3.14: Comparison between extrapolated spectrum (red) and the original one (black)

3.7 Exporting and MultiGraph

At the end of the analysis the user can type a label for the graph which will be used for the legend and select a color for the histograms. Moreover one can save the resulting spectra in a text file. Clicking the *save* button the user is asked to choose a name of the file in which, beyond the $f(y)$, $d(y)$, $yd(y)$ in both lineal energy and volt, the mean values and the label will also be saved.

In addition, the export button allows to load the spectra in the multi graph of the main window without saving it to file. From the main window, reported in Figure 3.15, the user can see the number of analyses saved and the corresponding labels and colors. There is also the possibility to fix the height of the spectra or to multiply a single histogram for a given factor.

Previously saved files can be loaded, without performing the analysis again. The user can then check the boxes relative to the quantity to be plotted and draw all the histograms in the same canvas. An example is reported in Figure 3.16.

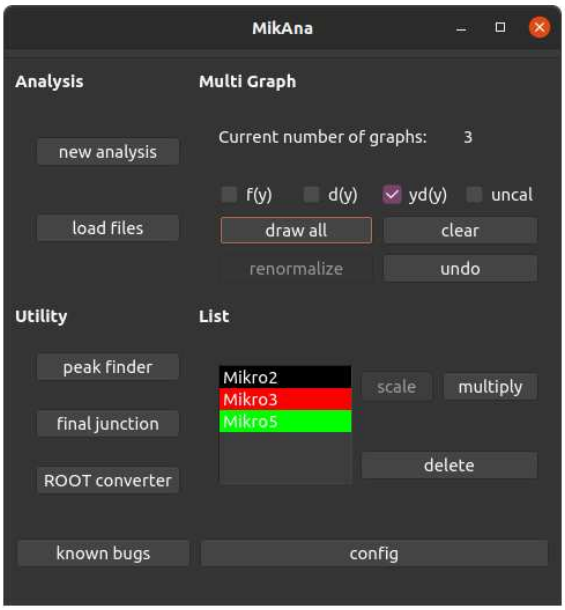

Figure 3.15: Main window with three different analyses loaded

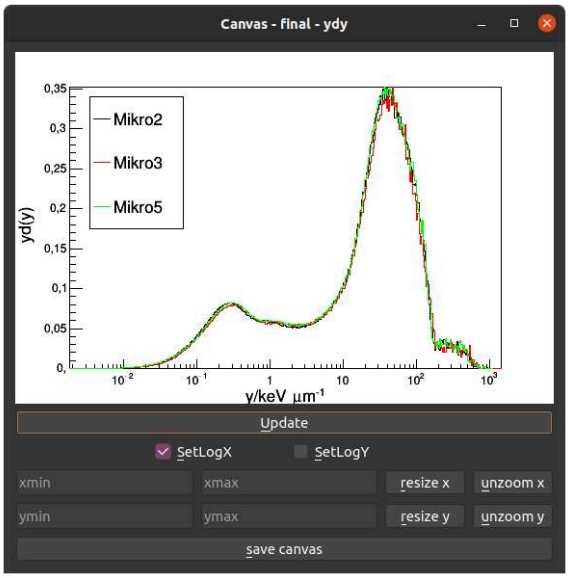

Figure 3.16: Final canvas with three $yd(y)$ spectra for different detectors

3.8 Junction between different voltages

As discussed before, since the spectra obtained with a lower bias and a higher one carry different but useful information, in the analysis it is helpful to join the spectra in one. In particular the objective is to keep the low-LET information carried by the data obtained with a higher voltage, around 850 V for these detectors, and integrate them with the high-LET part of the spectrum achieved with a lower bias, between 700 and 750 V.

In order to perform this task, *MikAna* has the option to "size and sew" the **H**igh **V**oltage (HV) spectrum with the **L**ow **V**oltage (LV) one. Once the *final junction* button is pressed on the main window, a pop-up asking to load the HV and LV file will appear, as in Figure 3.17. At this point, a canvas with the two spectra will show up, as in Figure 3.18. From the figure the limited proportionality of the spectra with 850 V bias can be observed: the higher LET events are more compressed respect to the ones obtained at 700 V, clearly indicating a loss of proportionality possibly caused by the shutdown of the avalanche. Instead the LV spectrum does not contain the LL events, since the low electric field is not able to prevent the recombination of electron-ion pairs.

Another window, with the same properties as the one for the extrapolation, allows the user to choose the cut point, with a red line moving in the canvas according to the position of the slider. After the procedure the mean values are re-evaluated, the user can type a name for the final histogram and save it in a text file, which can be loaded in the main window.

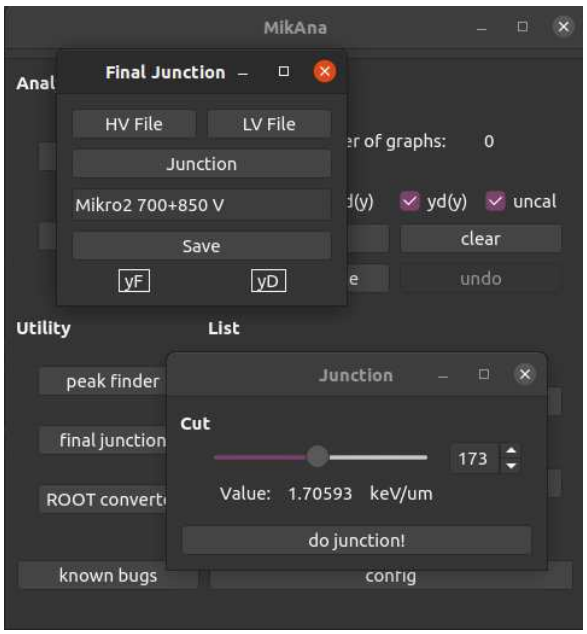

Figure 3.17: The main window with the final junction frame and the cut selection pop-up.

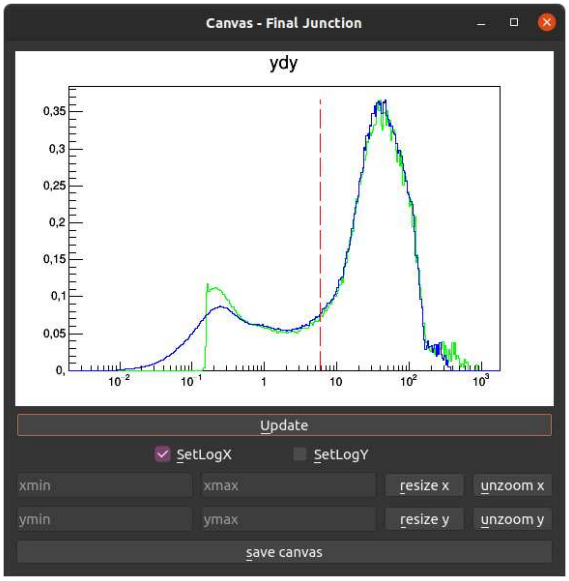

Figure 3.18: Canvas showing a spectrum obtained at 700 V (green) and one at 850 V (blue).

Chapter 4

Preamplifiers Test

4.1 Analog Chain

The first step in the analysis is verifying the correct functioning of the electronic chain. With the test bench previously described, for each pre-amplifier the integral and differential linearity has been checked, together with the noise level. The analog chain has been tested with the prototype preamplifiers *4MiCA-V0* and *4MiCA-V1*, in addition to the commercial *142PC* and *142* described in the previous chapter.

The integral linearity test has been performed by sending to the test input of the pre-amplifiers different voltage signals with similar properties of those provided by the detectors. For this purpose the *DT5800D* by *CAEN* has been used, sending the generated pulses into the test input of the preamplifiers. The amplitudes of the signals spans from 10 mV to 1110 mV in 10 mV steps, in the case of the x10 amplified channel these values have been divided by 10. Once the spectra have been acquired, each peak has been fitted with a gaussian function, providing the centroid and the sigma with related errors. Then a weighted linear fit has been performed between the centroids and the known amplitudes in voltage provided by the detector emulator, the fit results are shown in Figures 4.1a, 4.2a, 4.3a, 4.4a and 4.5a. In addition, the residuals of the fits have been evaluated as the distance between the centroid and the fit function, normalized with the value of the centroid and error calculated from the propagation. The residuals are reported in Figures 4.1b, 4.2b, 4.3b, 4.4b and 4.5b.

The noise level of the electronic chain can be estimated from the **F**ull-**W**idth at **H**alf-**M**aximum (FWHM) of the gaussian peaks. With the calibration from ADC to mV of the previous step, the relative FWHM has been calculated as

$$\text{FWHM} = \frac{2.35 \cdot \sigma}{H_0} \tag{4.1}$$

where H_0 is the position of the centroid resulting from the gaussian fit. The plots of the relative FWHM as function of the input signals amplitudes are in Figures 4.1c, 4.2c, 4.3c, 4.4c and 4.5c.

The last step regards the differential linearity and it has been performed using an analog pulser, which amplitude has been modulated by a ramp generator. In this case a good differential linearity should be represented by an angular coefficient of the linear fit as close as possible to zero. The spectra and the relative fits are shown in Figures 4.1d, 4.2d, 4.3d, 4.4d and 4.5d.

All the pre-amplifier resulted to be linear in the tested range, with the exception of the x1 channel of *4MiCA-V1*. From both the fit and the residuals the loss of linearity can be estimated to occur for input values above 800 mV. For this reason, in all future data acquisition with this specific preamplifier, it will be ensured that no portion of the spectrum will lay above that value.

The FWHM of the noise is acceptable, starting from less than 1% at 10 mV and rapidly decreasing as the reverse of the amplitude. For the amplified channel of *4MiCA-V1* the noise starts at about 6.5% and follows the usual trend. The result is acceptable given the x10 amplification.

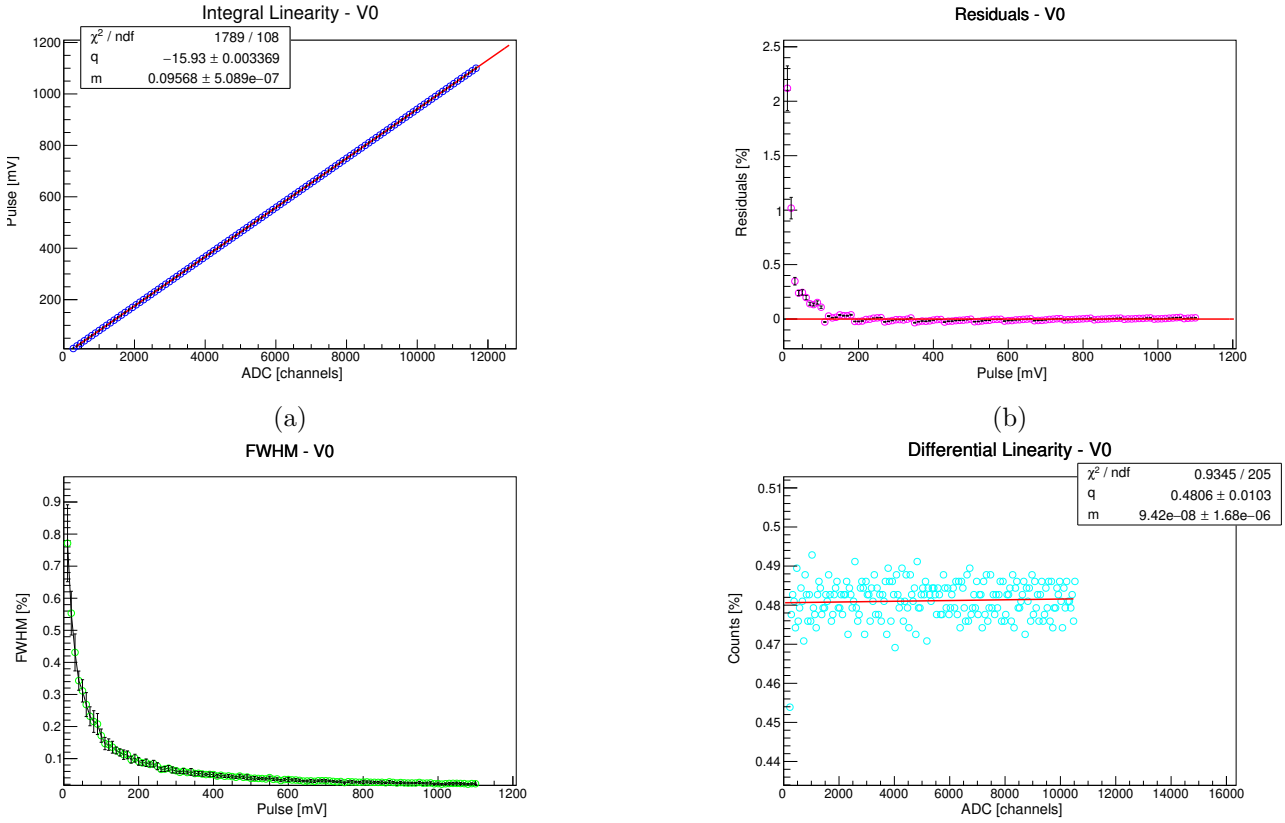

Figure 4.1: Analysis of the pre-amplifier *4MiCA-V0*.

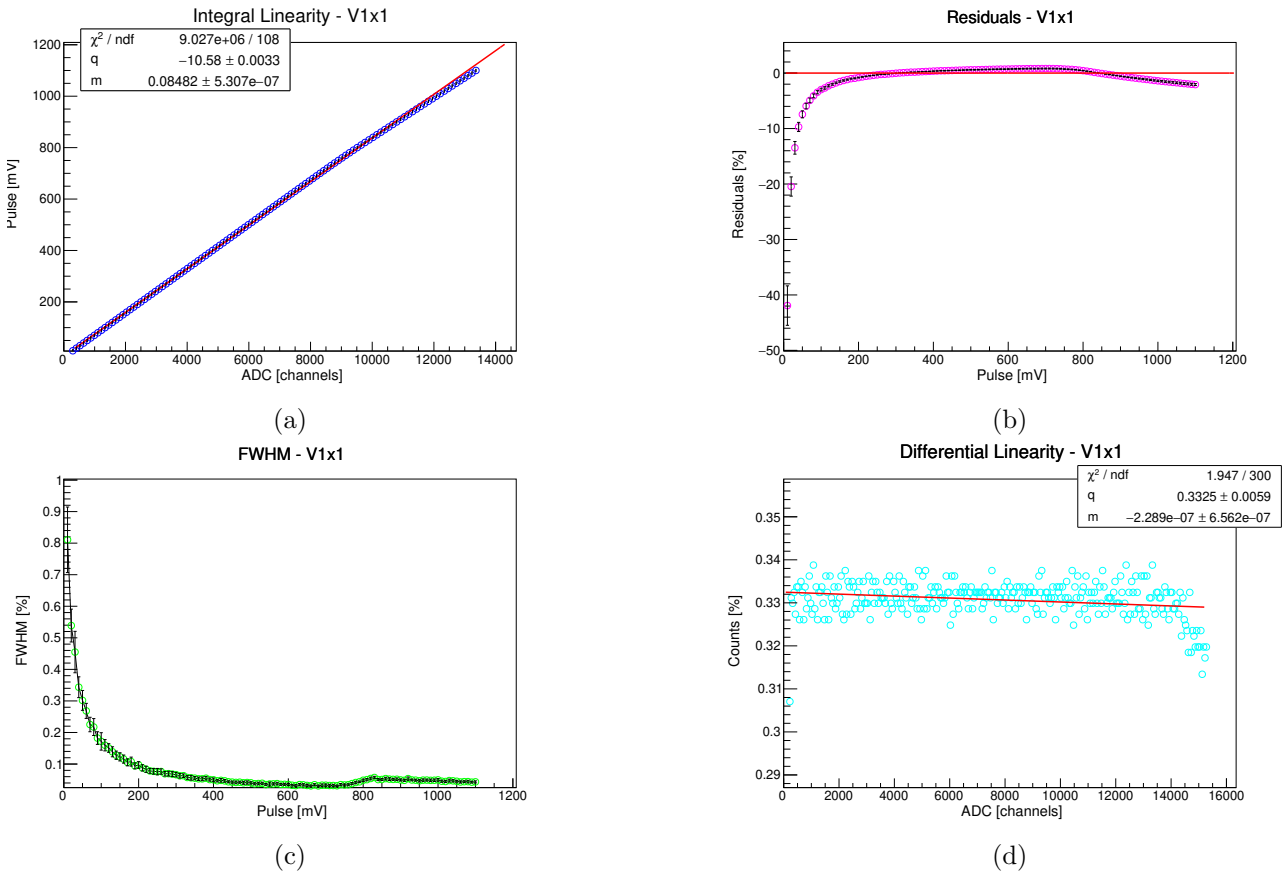

Figure 4.2: Analysis of the channel x1 of *4MiCA-V1*.

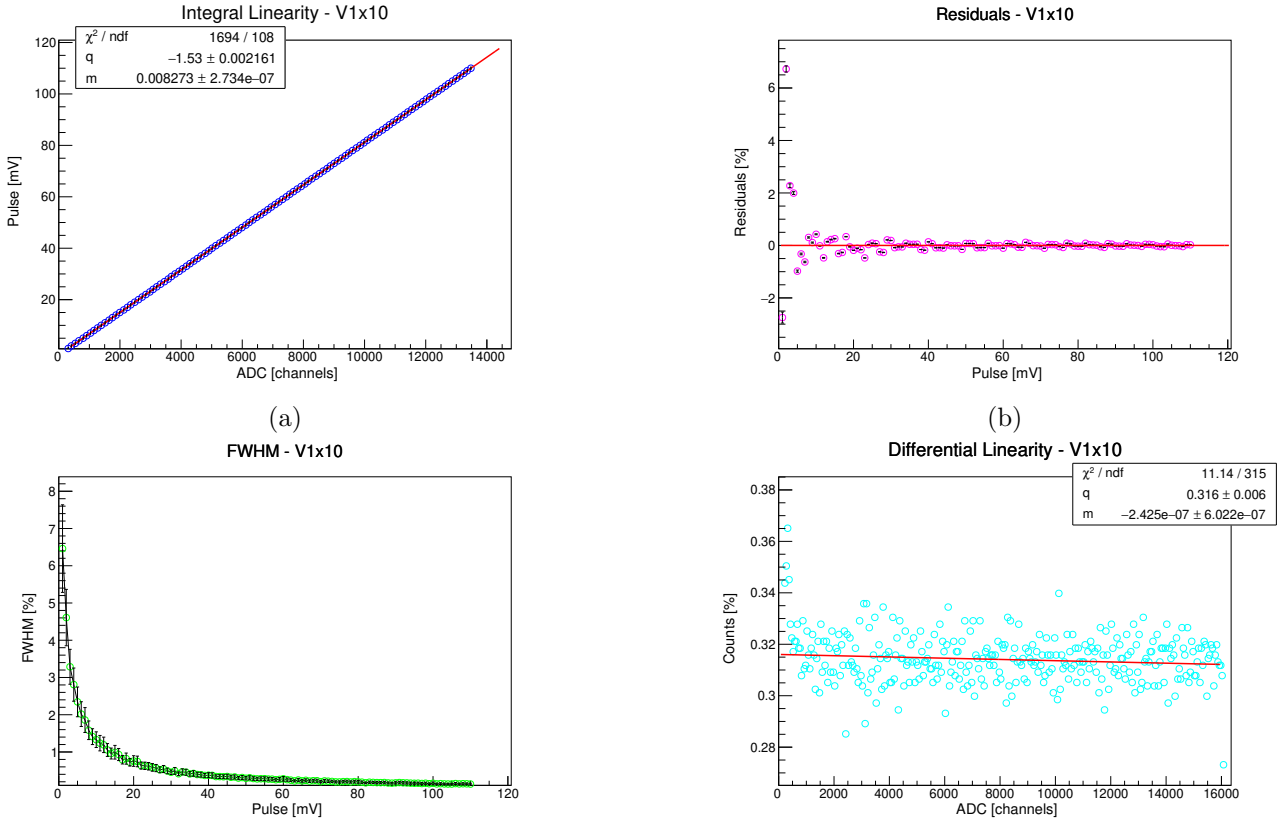

Figure 4.3: Analysis of the channel x10 of *4MiCA-V1*.

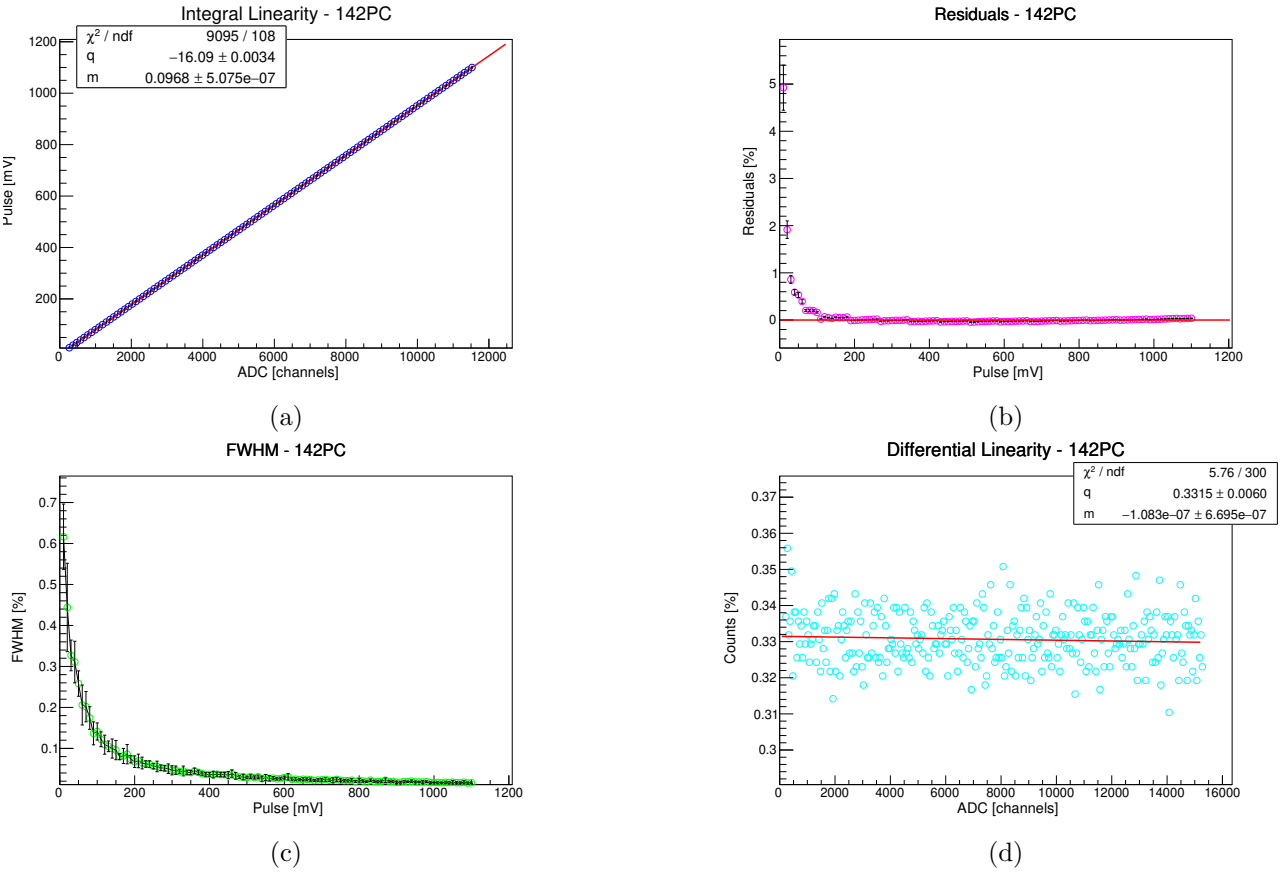

Figure 4.4: Analysis of the pre-amplifier *142PC* by *ORTEC*.

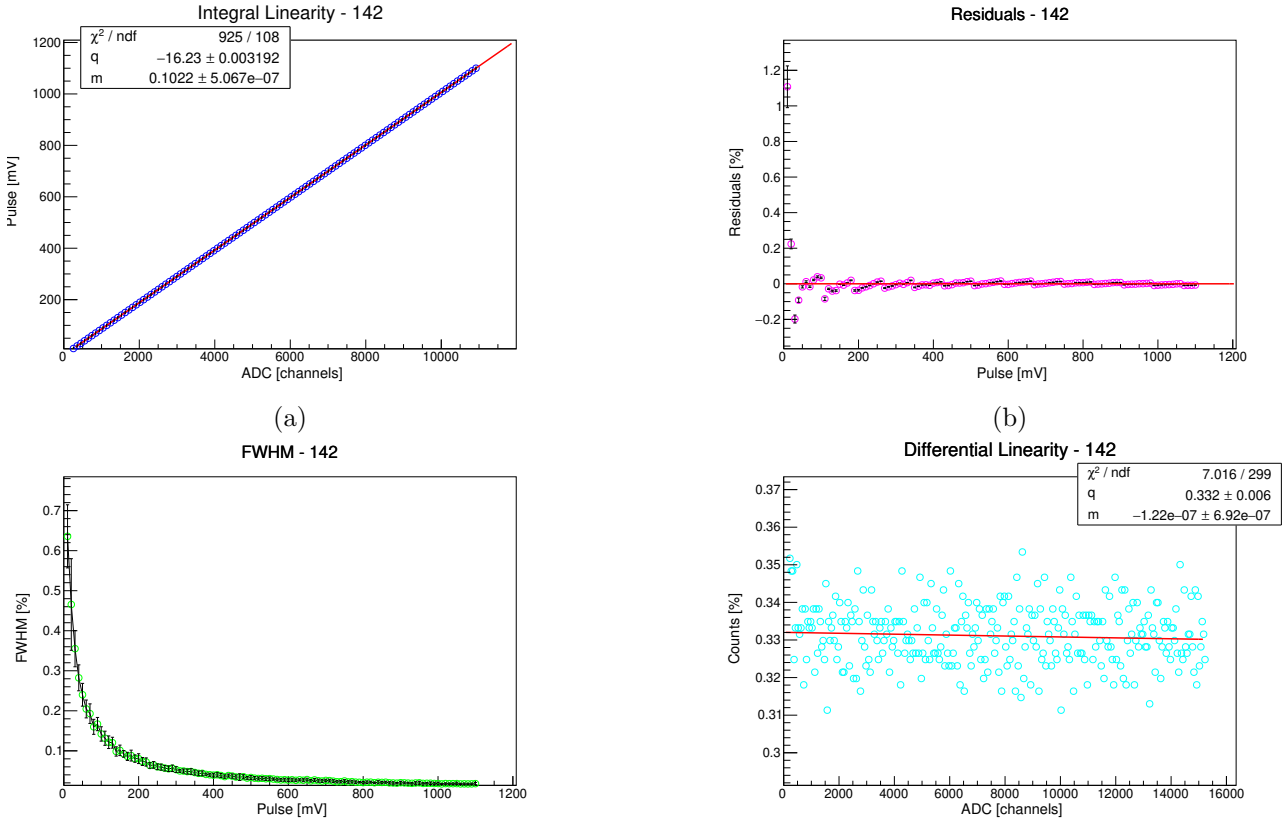

Figure 4.5: Analysis of the pre-amplifier *142* by *ORTEC*.

4.2 Digital Chain and Coupling

Since the detectors electrically behave like a capacitor, it is interesting to verify if the properties of the linear chain, once the detector has been connected and biased, deviate from the open circuit behavior. To perform this test, the detectors, one at the time, have been connected to the *4MiCA-V0* preamplifier and biased at 750 V using the power supply of the CAEN digitizer. Then the signals produced by the detector emulator have been sent to the test input of the preamplifier as in the previous section, and the output is analyzed by the digital chain described in a previous section.

For all the cases the FWHM results from two to four times larger, in particular it starts from 1.6-3.5% against the 0.6% obtained in the open circuit tests. This can be due to a larger signal to noise ratio in the digital chain, or to non-optimized parameters in the trapezoidal filter of the CAEN module. However, the linearity is preserved as shown by the fit results and there are no significant differences between the five detectors. The steps in the residuals are most likely due to the detector emulator, which is not able to convert some values in millivolts into *lsb*, its own unit of measure, without truncation. In particular 1 mV is equal to 7.8125 *lsb*.

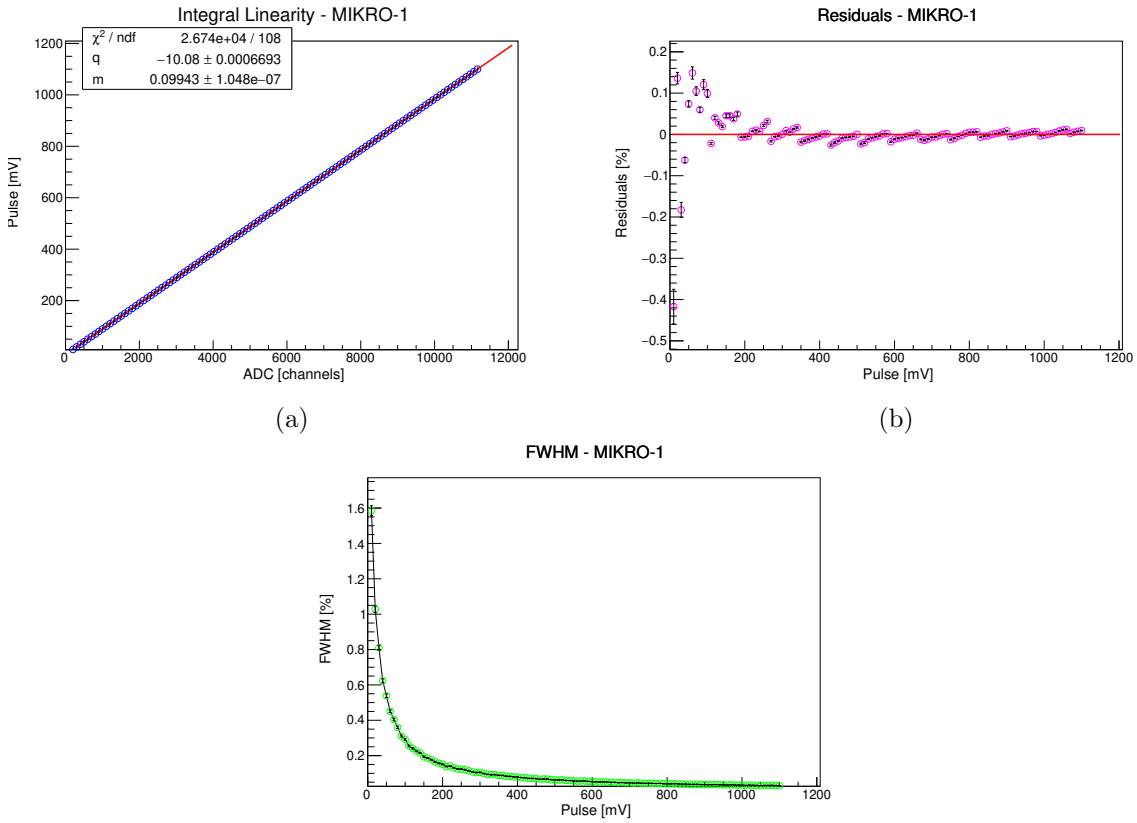

(a) (b)

(c)

Figure 4.6: Analysis of the pre-amplifier *4MiCA-V0* coupled with the detector *MIKRO-1*.

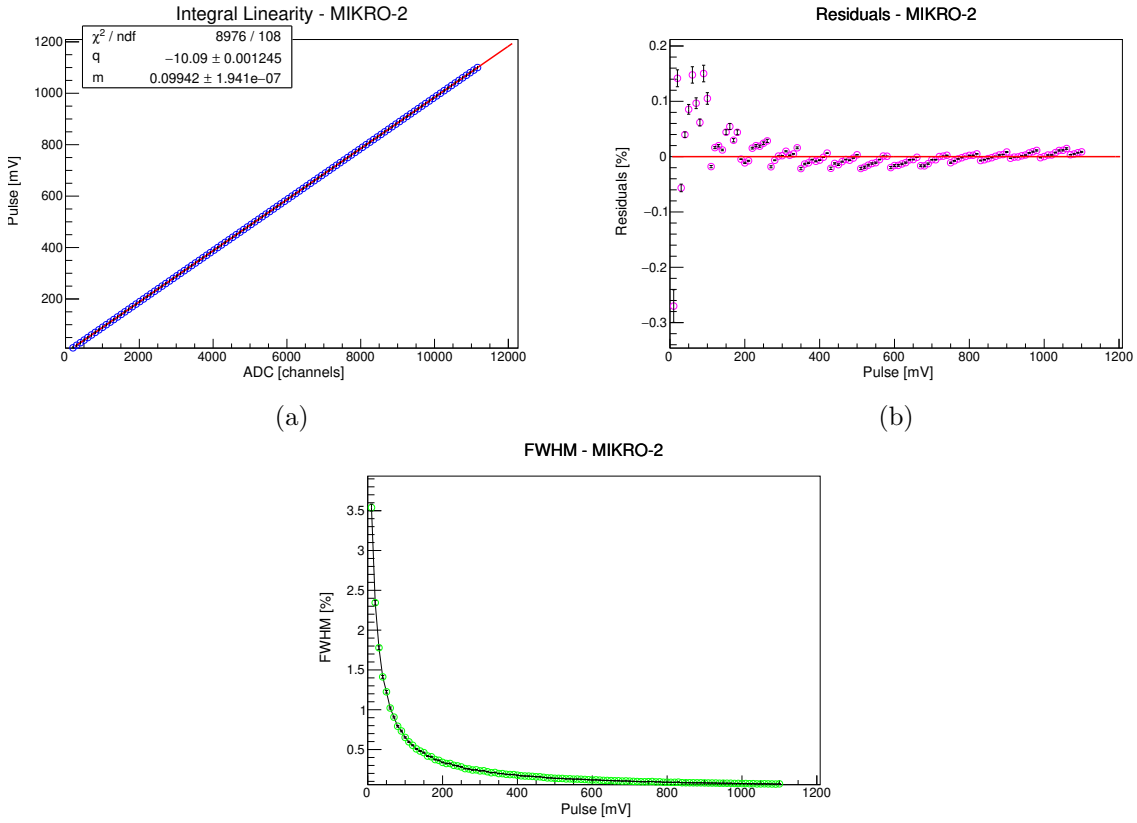

(a) (b)

(c)

Figure 4.7: Analysis of the pre-amplifier *4MiCA-V0* coupled with the detector *MIKRO-2*.

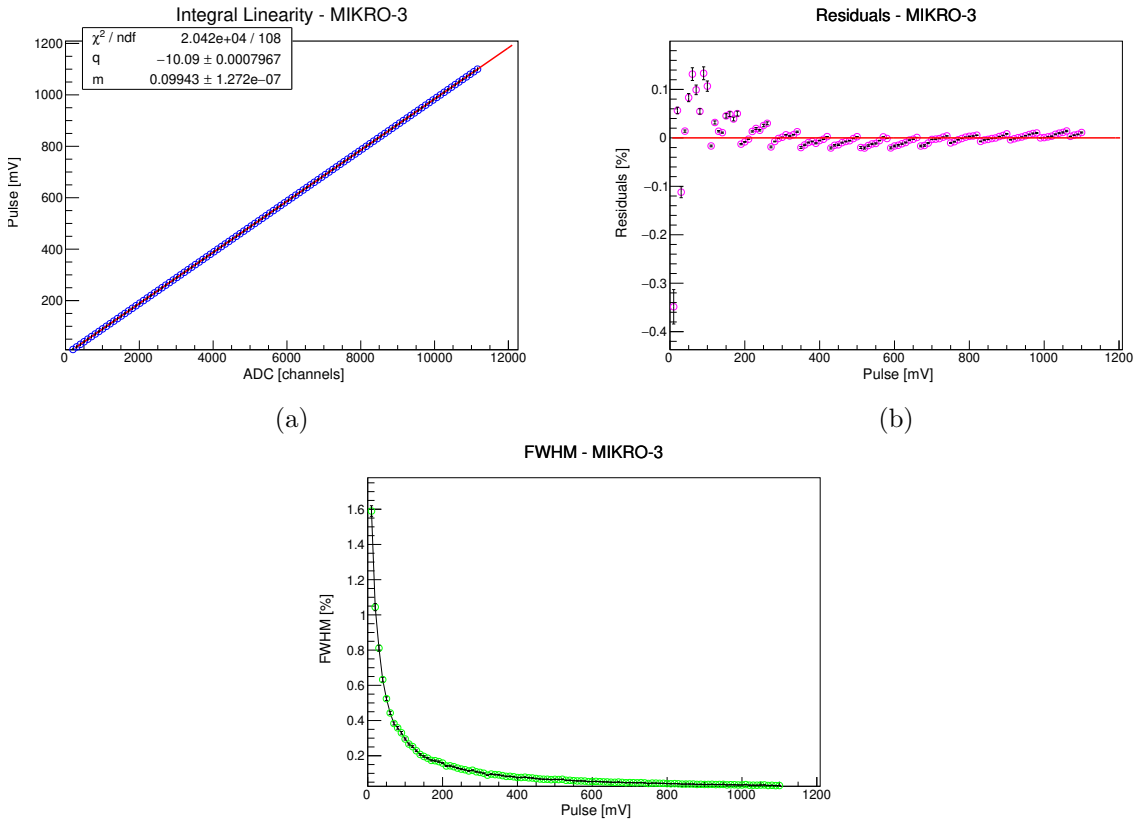

(a) (b)

(c)

Figure 4.8: Analysis of the pre-amplifier *4MiCA-V0* coupled with the detector *MIKRO-3*.

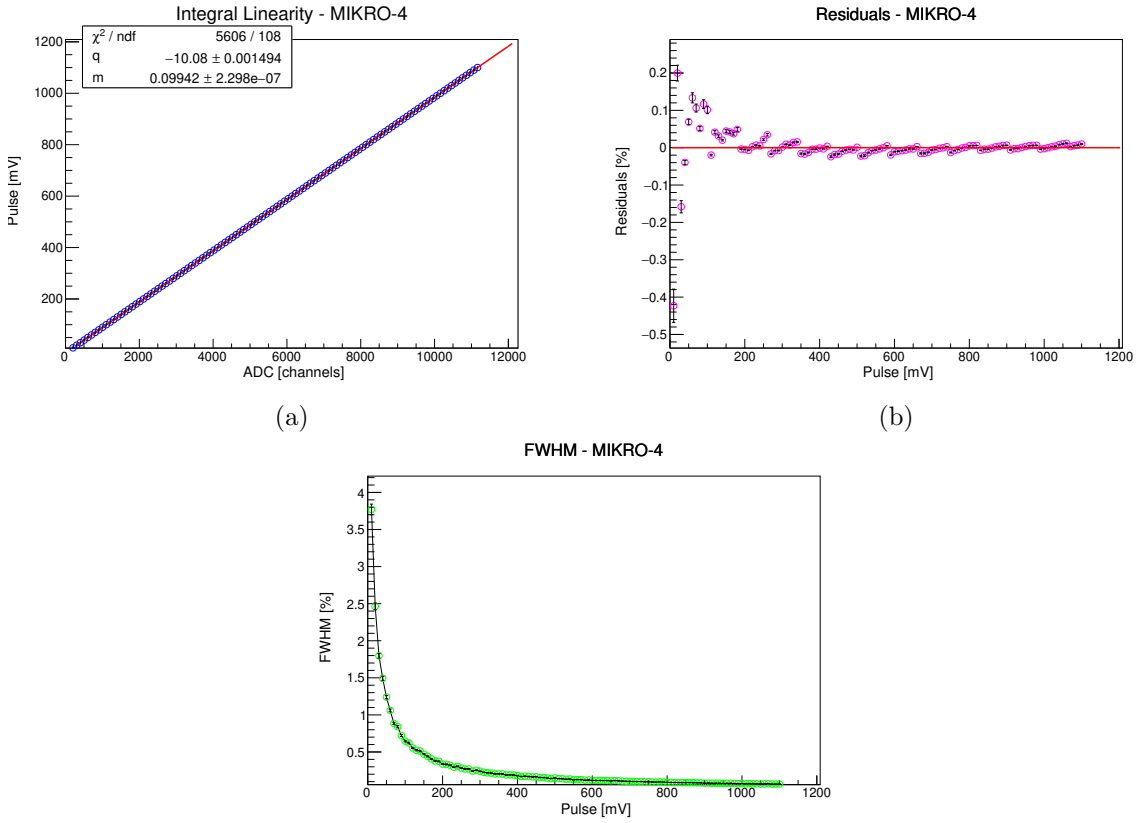

(a) (b)

(c)

Figure 4.9: Analysis of the pre-amplifier *4MiCA-V0* coupled with the detector *MIKRO-4*.

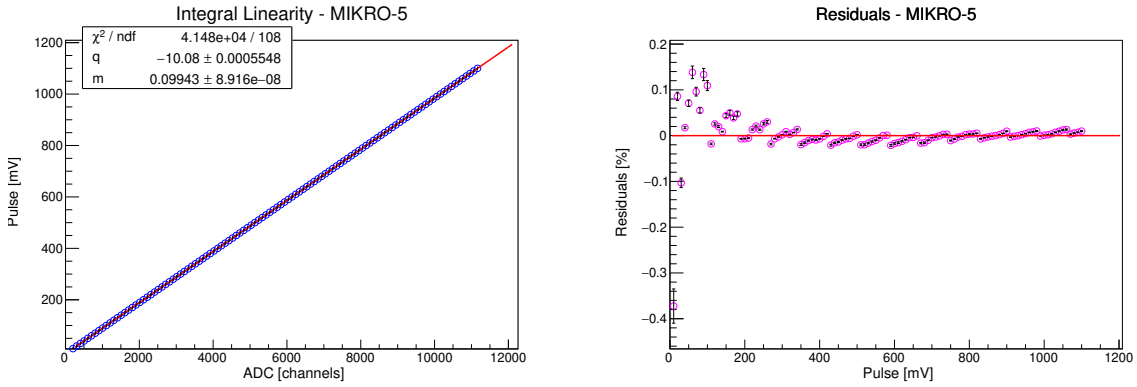

(a) (b)

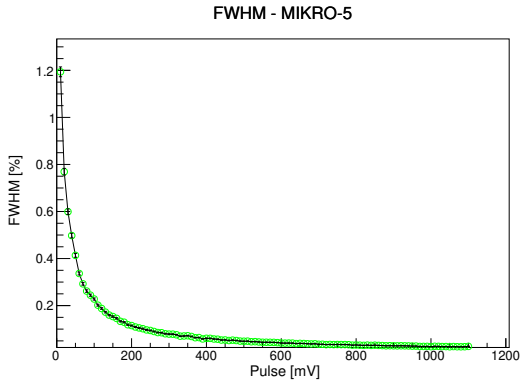

(c)

Figure 4.10: Analysis of the pre-amplifier *4MiCA-V0* coupled with the detector *MIKRO-5*.

Chapter 5

Measurements at the CN accelerator

The main aim of this chapter is to report the results obtained from the characterization of the five mini-TEPCs in the same known radiation field. A neutron spectrum has been acquired for each detector at the CN accelerator at the INFN-LNL facility and then the spectra calibrated in mV have been compared, in order to verify if the response functions of the detectors are the same both in terms of intrinsic gains and shape of the spectra, after the calibration in keV·μm^{-1}. For completeness, in addition to the shape of the spectra, the resulting mean values have also been compared.

As a last step, a comparison between the results obtained with different setups is present. The spectra obtained with the prototype preamplifier *4MiCA-V1* and the analog setup has been compared with the one obtained with the same preamplifier but a digital ADC and with the performance of a commercial preamplifier.

5.1 The CN accelerator at LNL

The first part of the analysis of the mini-TEPCs has been performed using a fast neutrons field available at the CN accelerator in the INFN-LNL facility. The CN is a "Van de Graaff" linear accelerator, its maximum high voltage at the terminal is nominally 7 MV.

To produce a neutron field, the reaction ^{7}Li(d,n)^{8}Be has been employed: energetic deuterons, at 5.5 MeV, are provided by the accelerator and directed toward the lithium target via magnetic deflectors. In particular, the target is made of a thin LiF layer, of mass thickness of 1000 μg·cm^{-2}, sputtered on a graphite surface thick enough to stop the deuterium passing through the LiF layer without interacting. Under these conditions, since the Q-value of the reaction is 15.1 MeV, neutrons are produced with energies up to 20 MeV. The deuteron current has been monitored during the data acquisitions, and it varied in a range between 250 and 350 nA.

All the detectors have been filled with pure propane at a pressure of 40.9 kPa at 21.8 °C. At this pressure, the mass thickness in the sensitive volume is 0.075 mg/cm^2, which is equivalent, in terms of imparted energy distributions, to 1 μm of biological tissue [22]. They have been placed about 1 cm away from the target and for each measurement, two data acquisitions, obtained at 750 V and 850 V, have been joined as described in Chapter 3. Pictures of the setup and of the detector are shown in Figure 5.1 and 5.2.

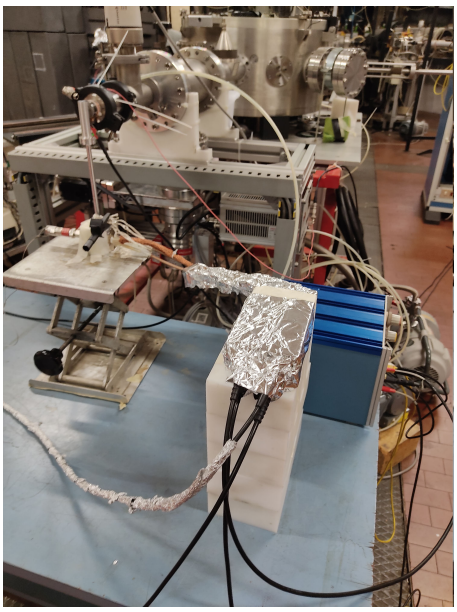

Figure 5.1: Picture of the setup at CN.

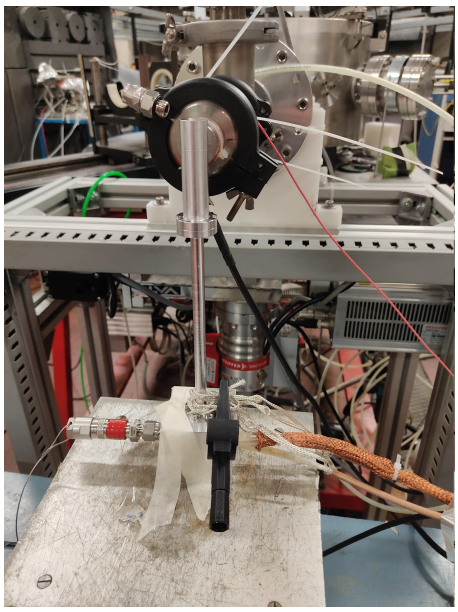

Figure 5.2: A detail of the detector in front of the target.

5.2 Test of the New *4MiCA-V1* Preamplifier

In this paragraph a comparison of the performances of different front-end electronics and different **D**ata **A**cquisitions **S**ystems (DAQs) when coupled to the same detector are shown.

In Figure 5.3 the spectra obtained with the commercial charge-sensitive preamplifier *142PC* and with the custom preamplifier *4MiCA-V1*, specifically designed at the *Politecnico di Milano* to be used with mini-TEPCs, are shown. Furthermore, in the same plot, a spectrum obtained with the *4MiCA-V1* preamplifier coupled with the digital acquisition system based on *DT5780* by *CAEN* is reported.

The *142PC* preamplifier is a low-noise charge-sensitive unit especially designed for use with proportional counters, with a noise of about 300-400 rms electrons. The prototype *4MiCA-V1* unit has a wider dynamic range and a noise much lower than 300 rms electrons. When connected to the *MIKRO* detectors, the lowest detectable signals corresponded to events of 0.2 keV$\cdot\mu$m^{-1} and 0.04 keV$\cdot\mu$m^{-1} respectively. Thanks to the wider dynamic range of *4MiCA-V1*, due to the low noise when coupled to the detector, it is possible to recover more information on the low LET part of the spectrum that is hidden below noise when the *142PC* preamplifier is used.

The best setup was proved to be the analog chain coupled with the *4MiCA-V1* preamplifier. In this case the minimum lineal energy is 0.04 keV$\cdot\mu$m^{-1}.

With the aim of moving towards a more compact setup for the employment in the clinical environment, it is under investigation the possibility of using digital DAQ to replace the high-resolution analog chain. During this thesis a digital DAQ has been tested to verify if the digital trapezoidal filter performed by the FPGA would allow a better discrimination between signal and noise with the result of a lower detection threshold. However, in this case the analog DAQ has proven to have a lower threshold, possibly related to a better noise filtering of the shaping amplifiers, allowing the peak-sensing ADC to better discriminate signals from the noise. This result is not invalidating, as it depends on the specific digital module: the *DT5780* uses a threshold trigger on the input signal to discriminate the noise, and then it performs the filtering only if the signal is larger than such threshold. Therefore, it can be expected that the module is not able to extract smaller signals from the noise level, unlike the analog shaper which continuously shape the input signal and then uses a discrimination algorithm on the shaped trace. There are digital ADC available on the market with the same logic, however this requires more computational power and hence these devices are more expensive.

Given the differences in the noise threshold, the electronic chain is also affecting the proton component of the spectrum. As reported in Table 5.1, the mean difference between the full analog chain with *4MiCA-V1* and the one with the commercial preamplifier is 6%. This is due to the higher noise contribution of the *142PC*, leading to a lower resolution which causes a larger proton peak, as clear in Figure 5.3. The value is lowered down to only the 2% for the digital chain coupled with the *4MiCA-V1* preamplifier. As discussed before, the low LET component depends mainly on environmental activation and, since the data sets have been obtained in different days, the comparison of this portion of the spectra is not significant.

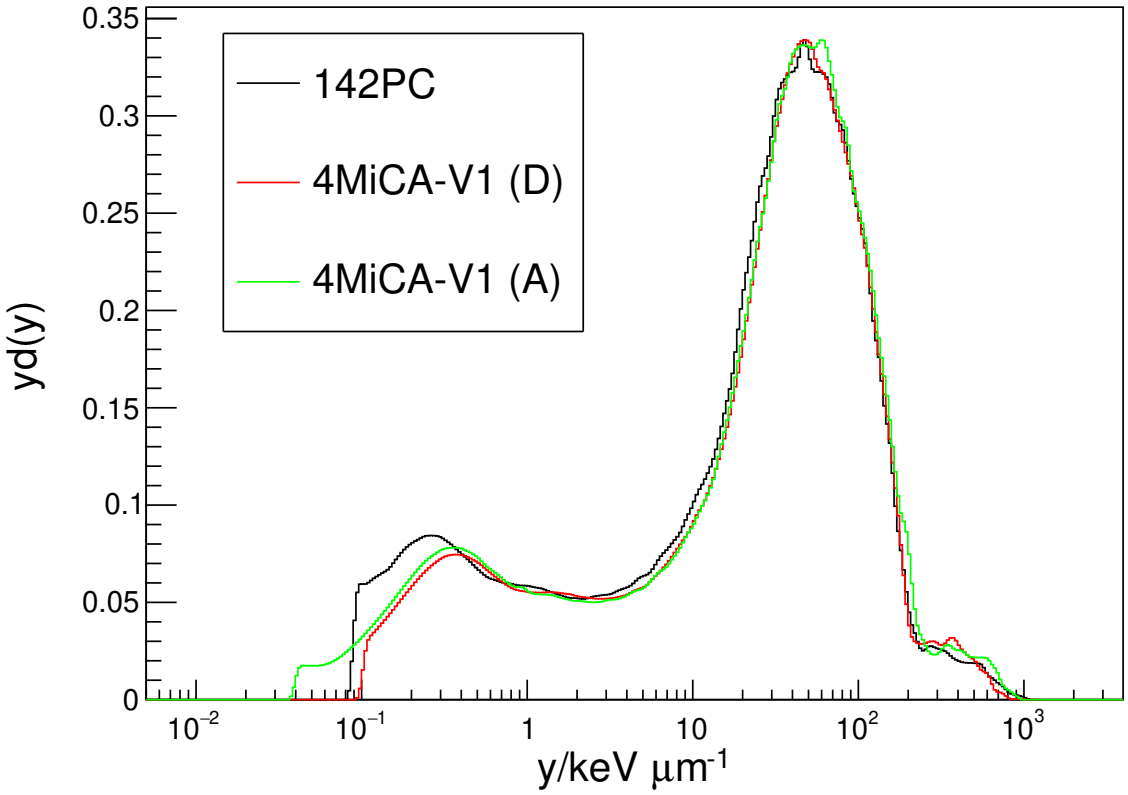

Figure 5.3: Spectra obtained with the *142PC* and analog ADC (black), *CAEN* digitizer and *4MiCA-V1* (red) and analog chain with *4MiCA-V1* (green).

χ [%]	Total	< 10 keV·μm^{-1}	$10 - 171$ keV·μm^{-1}	> 171 keV·μm^{-1}
142PC	12	13	5	20
4MiCA-V1 (D)	30	32	2	68

Table 5.1: Mean distance in percentage between the spectra obtained with the Ortec preamplifier, or the *CAEN* digitizer, and the analog chain with the *4MiCA-V1* preamplifier.

5.3 Reproducibility

5.3.1 Internal Gain

In order to verify the reproducibility of the response function of the 5 engineered mini-TEPCs produced, the spectra obtained with different detectors at the CN facility have been compared using the same electronic chain. The data analysis has been performed through the *MikAna* software with the procedure described in Chapter 3.

The first parameter that has been investigated is the internal gain of the detector when the same high voltage is applied to the cathode. As discussed before, the internal gain of a TEPC is the proportionality constant between the deposited energy by ionizing radiation and the response of the detector, for this reason the spectra reported in Figure 5.4 are expressed in mV, before the calibration in lineal energy. From this representation it is evident that the detectors present different internal gains, as the spectra are shifted between themselves. The reason behind the gain difference is still unclear and needs further investigations.

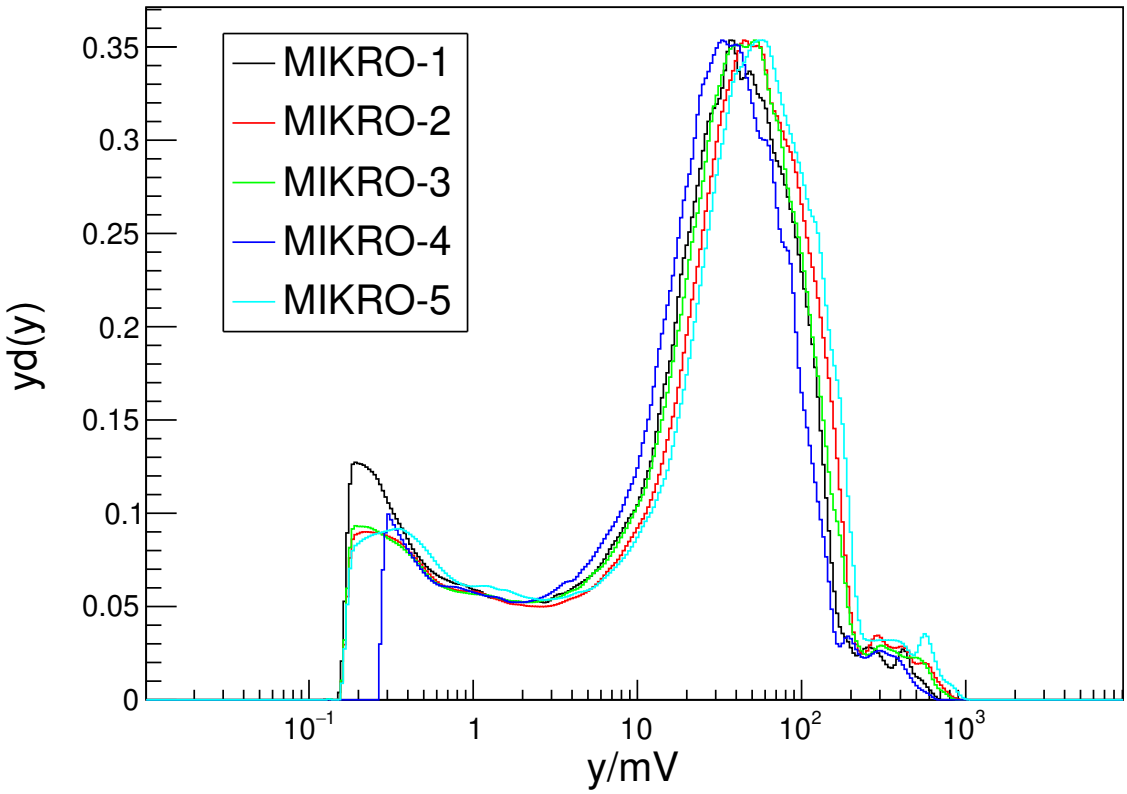

Figure 5.4: Dataset obtained at the CN accelerator with the five detectors. The spectra are calibrated in mV to observe the internal gain of the prototypes.

However, similar, and even more severe, internal gas gain variability can be registered with commercial detectors. Two nominally identical detectors, developed by *Far West Technology, Inc.* [40], have been filled with propane gas at the pressure of 32.2 kPa to simulate 1 μm of biological tissue and exposed to the same neutron field at the CN facility. The FWT detectors, model *FWT LET-1/2"*, are spherical mini-TEPCs with 1.27 cm of diameter and inner walls made of A-150 plastic. In principle their response function should be the same, as they are nominally identical. The spectra calibrated in mV are shown in Figure 5.5. For the second detector, the *FWT-2*, the bias voltage has been increased in order to obtain the same portion of the spectra achieved with the *FWT-1*, highlighting that the gain of this detector is much lower than the one of *FWT-1*. In addition, the slopes of the proton edge result different, indicating different resolutions of the two devices.

Once the spectra have been calibrated in keV$\cdot\mu$m^{-1}, as shown in Figure 5.6, the results are very similar. In Figure 5.7 the calibrated spectra obtained with the detectors *MIKRO-1* and *MIKRO-2* are present, highlighting a larger dynamic range of the new *MIKRO* devices and the same response function for both detectors, since the shape of the microdosimetric spectrum is completely superimposable with respect to the differences observed in Figure 5.6 for the *FWT* detectors. The comparison between *FTW-1* and *MIKRO-2* is shown in Figure 5.8. From this figure some differences in the shape of the spectra can be observed.

These small discrepancies between the two spectra are consistent with the different geometrical shapes (spherical and cylindrical), as the distributions of the mean chords changes depending on the volume. What can be also noted in the comparison, is the improved dynamic range obtained with the new setup (detector and preamplifier) thanks to which more than one decade of signal is recovered from below the noise.

To conclude, there is a variability in the gain of the *MIKRO* detectors that can be further investigated but that is also observed in commercial TEPCs such as the *FWT LET-1/2"*. However, the response function of the *MIKRO* detectors is the same once the calibration in lineal energy is performed while some differences are still present in the spectra gathered with the two commercial TEPCs indicating a different resolution between the two detectors. Moreover, this comparison has proved that the new setup that includes both the detector and the preamplifier allows a lower detection threshold increasing the dynamic range of more than one order of magnitude.

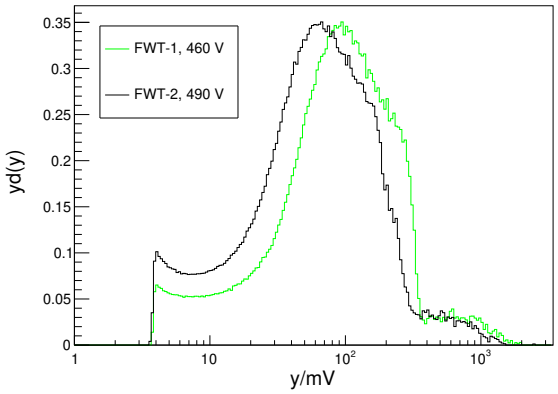

Figure 5.5: Dataset obtained at the CN accelerator with the FWT detectors. The change in voltage has been necessary to obtain the same portion of spectrum.

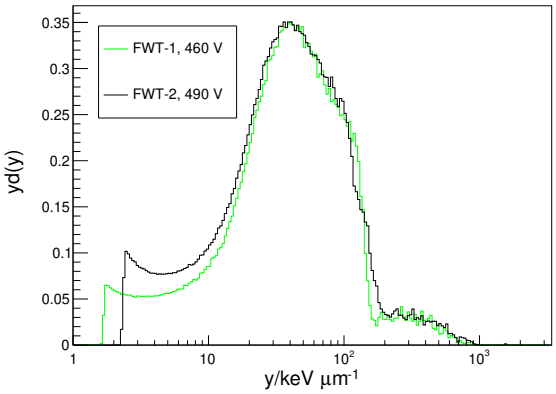

Figure 5.6: Calibrated spectra obtained with the detectors *FTW-1* and *FTW-2*.

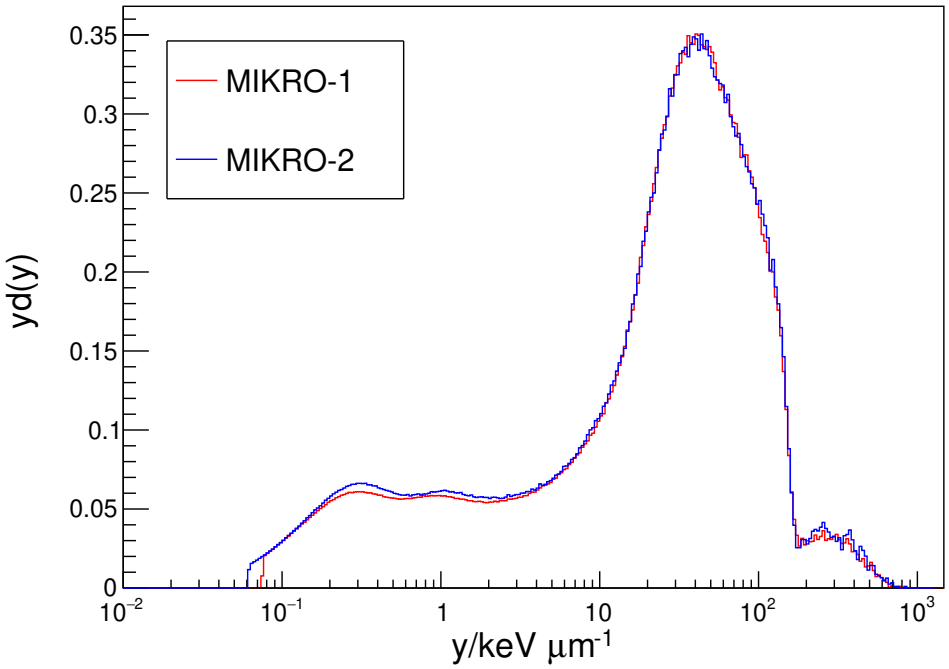

Figure 5.7: Calibrated spectra obtained with the detectors *MIKRO-1* and *MIKRO-2*.

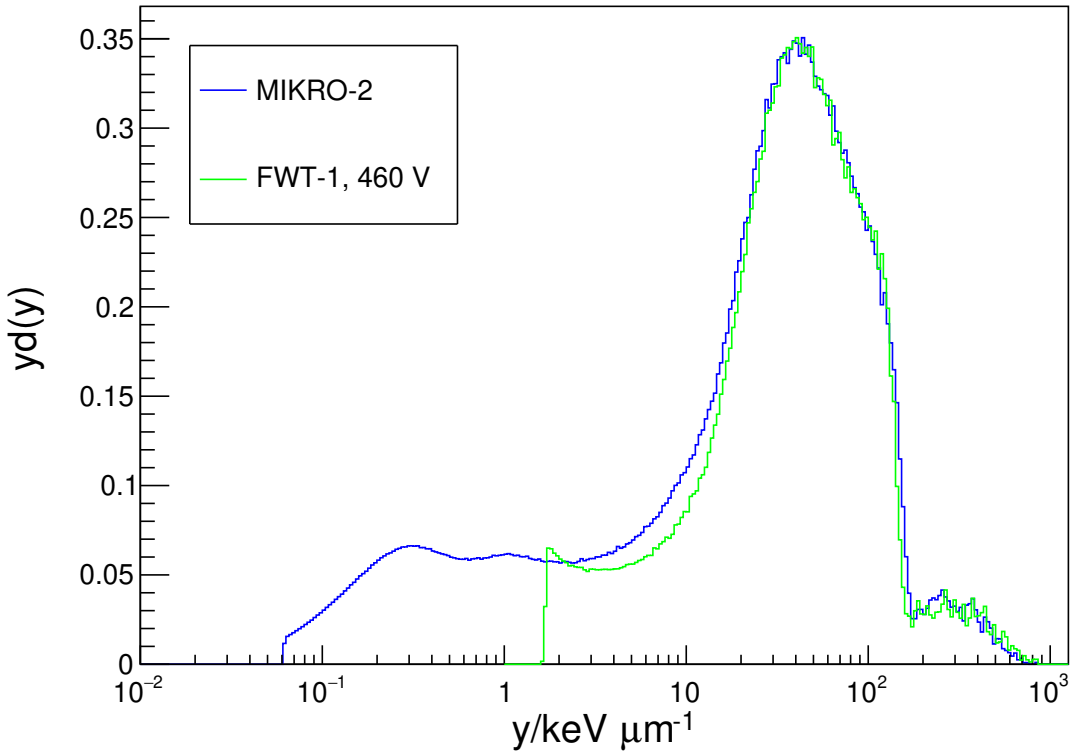

Figure 5.8: Comparison between the spectrum obtained with the detector *MIKRO-2* and the one obtained with *FTW-1*, employing the same neutron field.

5.3.2 Shapes and Mean Values

The spectra resulting from the analysis after the self-calibration in keV·μm^{-1}, obtained with the Fermi fit on the proton edge and the linear extrapolation, are shown in Figure 5.9, while the corresponding mean values of the distributions are presented in Table 5.2. The average $yd(y)$ distribution has been evaluated as the arithmetic mean, bin by bin, of the five measured distributions. In particular for each bin j, summing over the i-th detector, the mean with its uncertainty is given by

$$\overline{X}_j = \frac{1}{N_{\text{det}}} \sum_{i=1}^{5} x_j^i, \quad \sigma_{\overline{X}_j} = \sqrt{\frac{\sum_{i=1}^{5} \left(\overline{X}_j - x_j^i\right)^2}{N_{\text{det}} - 1}} \tag{5.1}$$

The average distribution is also shown in Figure 5.9, with error bars representing one standard deviation. It can be observed that the agreement between the different spectra is generally good, with differences more visible in the low lineal energy region corresponding to the photon component. The frequency and dose mean values of the lineal energy, calculated as the average of the mean values obtained by each detector, are $\overline{y_{\text{F}}} = (0.88 \pm 0.03)$ keV·μm^{-1} and $\overline{y_{\text{D}}} = (43 \pm 2)$ keV·μm^{-1}, and all the experimental values agree with the average within one standard deviation. The relative standard deviation is 3.4% for $\overline{y_{\text{F}}}$ and 4.6% for $\overline{y_{\text{D}}}$, which is below the usual uncertainties assigned to these values (7% for the $\overline{y_{\text{F}}}$ and 5% for the $\overline{y_{\text{D}}}$ [41]). To study in more detail the discrepancies between the different experimental spectra, the raw residuals of each $yd(y)$ distribution with respect to the average spectrum are shown for each detector in Figures 5.11, 5.12, 5.13, 5.14 and 5.15. In these figures the error bars result from the error propagation on the $f(y)$ distribution.

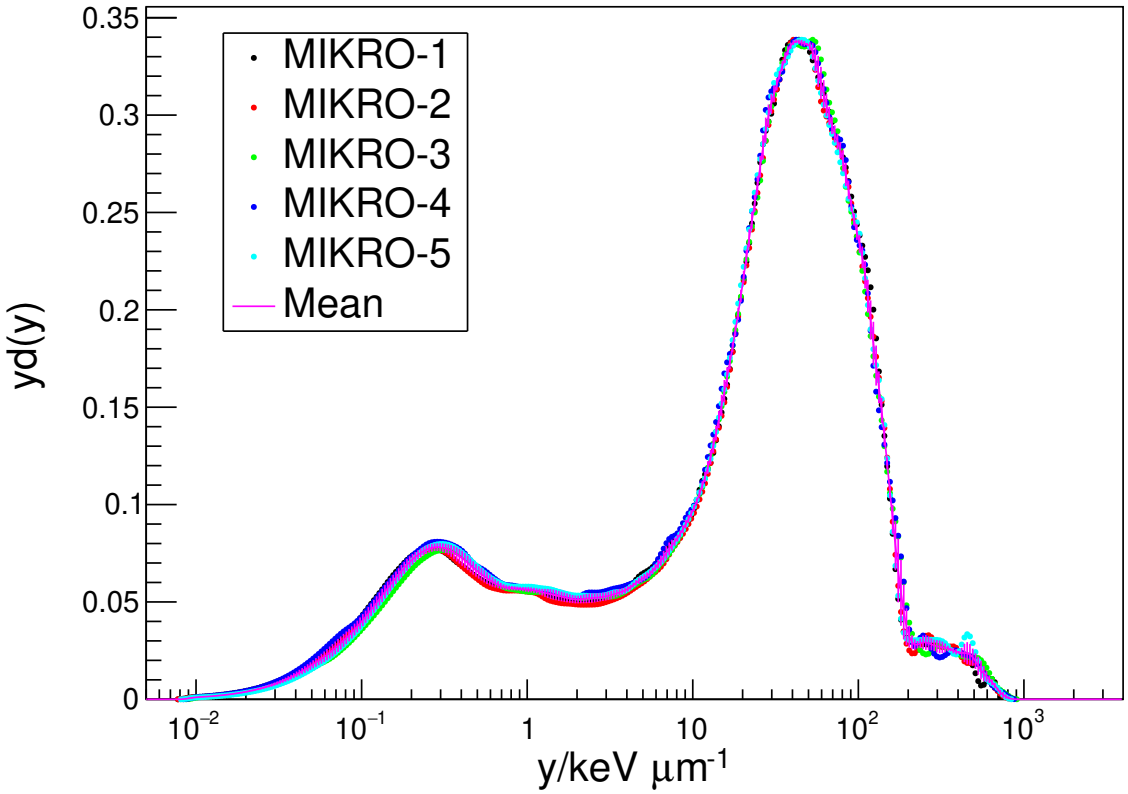

Figure 5.9: Dataset obtained at the CN accelerator with the five detectors. Error bars on the average distribution correspond to one standard deviation.

	$\overline{y_F}$ [keV·μm^{-1}]	$\overline{y_D}$ [keV·μm^{-1}]
MIKRO-1	0.85	42.7
MIKRO-2	0.87	43.7
MIKRO-3	0.86	40.1
MIKRO-4	0.89	42.6
MIKRO-5	0.91	45.3
Average	0.88±0.03	43±2

Table 5.2: Mean values of the microdosimetric spectra.

Two different estimators have been applied to further investigate the similarity of the responses of the detectors. The first one is the mean distance from the average, expressed in percentage, while the second one is the compatibility λ. In particular a value of $\lambda < 1$ means a difference of less than one standard deviation between two values, and can be interpreted as the fact that the only difference between the results is originated by statistics. For the i-th detector, summing over the bins j, their definitions are

$$\chi_i = \frac{1}{N}\sum_j^N \frac{\left|\overline{X}_j - x_j^i\right|}{\overline{X}_j} \tag{5.2}$$

$$\lambda_i = \frac{1}{N}\sum_j^N \frac{\left|\overline{X}_j - x_j^i\right|}{\sigma_{x_j^i}} \tag{5.3}$$

Both the variables have been calculated on the full spectra, and on the three main regions of interest discussed before: below 10 keV·μm^{-1}, between 10 and 171 keV·μm^{-1} and above the proton edge. The results are reported in Table 5.3 and Table 5.4.

χ [%]	Total	< 10 keV·μm^{-1}	$10 - 171$ keV·μm^{-1}	> 171 keV·μm^{-1}
MIKRO-1	5.2	4.5	3.1	12.3
MIKRO-2	5.3	5.0	3.2	9.9
MIKRO-3	7.9	4.2	2.2	32.9
MIKRO-4	7.3	7.8	2.8	13.2
MIKRO-5	5.9	5.1	2.5	16.1

Table 5.3: Mean distance in percentage between each spectrum and the average, calculated as in Equation 5.2.

λ	Total	< 10 keV·μm^{-1}	$10 - 171$ keV·μm^{-1}	> 171 keV·μm^{-1}
MIKRO-1	1.61	2.36	0.43	0.24
MIKRO-2	0.99	1.30	0.56	0.39
MIKRO-3	1.93	2.80	0.42	0.98
MIKRO-4	2.3	3.70	0.93	0.99
MIKRO-5	2.06	3.12	0.41	0.26

Table 5.4: Compatibility between each spectrum and the average, representing the distance between the average and a measure in units of standard deviation, as in Equation 5.3.

The indicators report a good agreement between the measurements in the intermediate LET range, while the low and high LET components are more distant between data sets. In particular the χ variable shows differences up to 32.9% in the high LET portion of the spectra, while the low LET one is some percentage points higher than the intermediate one. However these results can be expected for the low LET portion of the distribution, since it is dominated by γ-rays. In particular, the photon component is highly dependent on environmental conditions, such as activation of the target and the materials surrounding the detector due to the neutron interactions, and can vary with time. In fact, as shown by the λ parameter, the spectra are not compatible in the low LET region, highlighting the fact that the activation of the environment has changed among the acquisitions.

The differences in the high LET components can be traced back to statistics. In fact, the events above the proton edge are due to heavy particles, like α or other heavy recoil nuclei, and since they are rare (in average 1 large event happens every 1000 medium LET events, according to the frequency distributions), larger fluctuations among different spectra can be expected. Despite the fluctuations, since λ is less than one, it can be concluded that the spectra are fully compatible and therefore the differences are only due to statistic, as expected.

To visualize the dependence of the $\overline{y_{\mathrm{D}}}$ on those events the $y^2 d(y)$ can be used, as shown in Figure 5.10. In this function equal areas under the curve correspond to equal contributions to the second momentum of the $f(y)$ distribution and, in this case, it can be obtained that the few tens of events above the proton edge are responsible for about the 25% of the contribution on the $\overline{y_{\mathrm{D}}}$, despite the dataset contains more than 10^5 events.

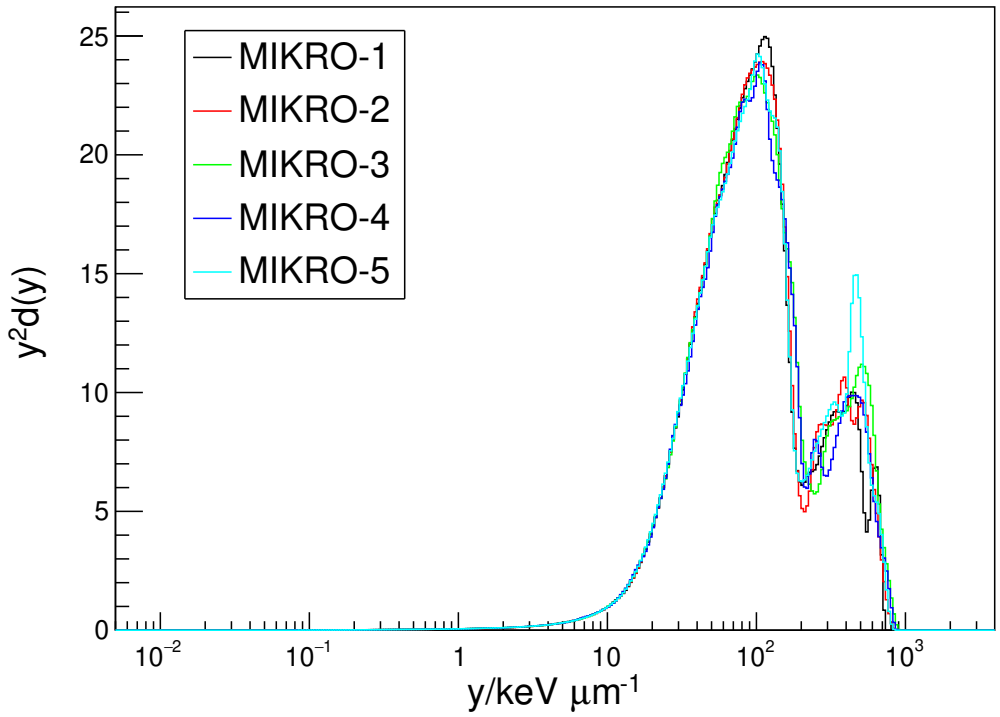

Figure 5.10: The $y^2 d(y)$ distribution for the different datasets. In this case equal areas correspond to equal contributions to the $\overline{y_D}$.

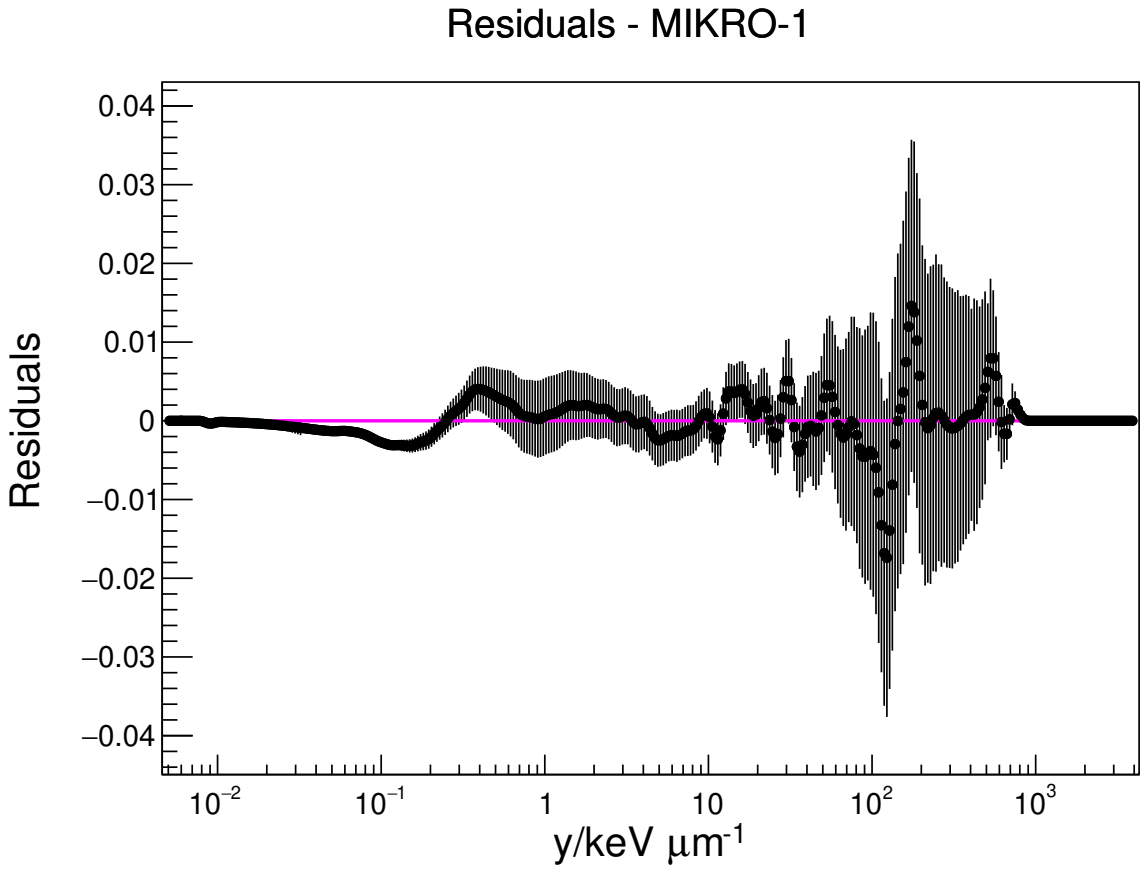

Figure 5.11: Residuals of *MIKRO-1* respect to the average.

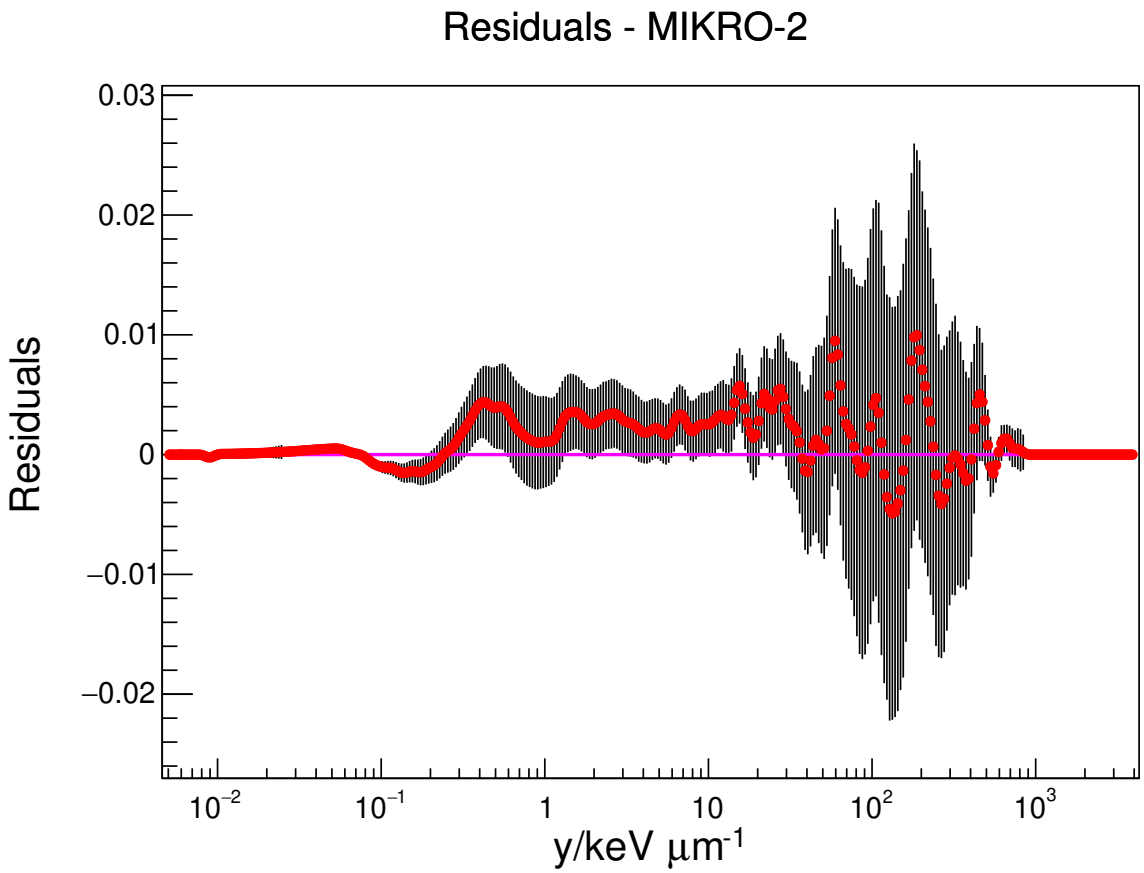

Figure 5.12: Residuals of *MIKRO-2* respect to the average.

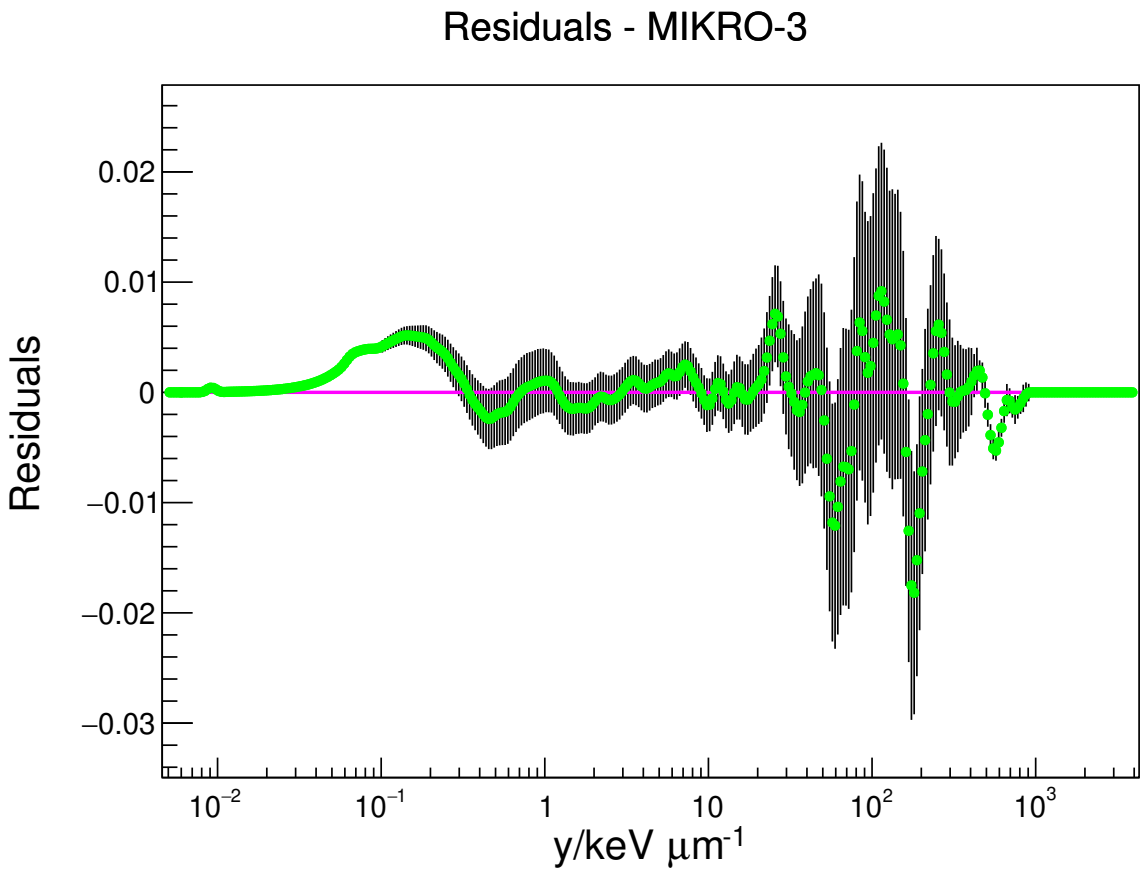

Figure 5.13: Residuals of *MIKRO-3* respect to the average.

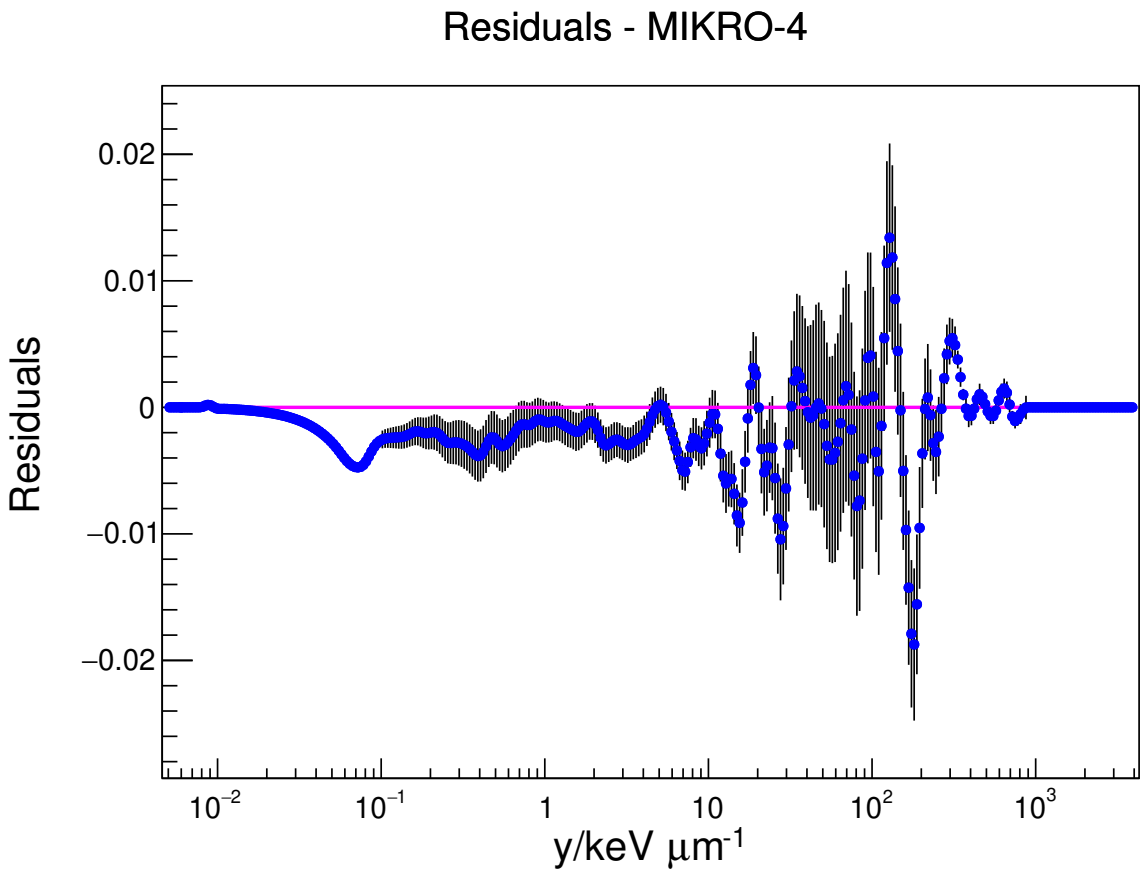

Figure 5.14: Residuals of *MIKRO-4* respect to the average.

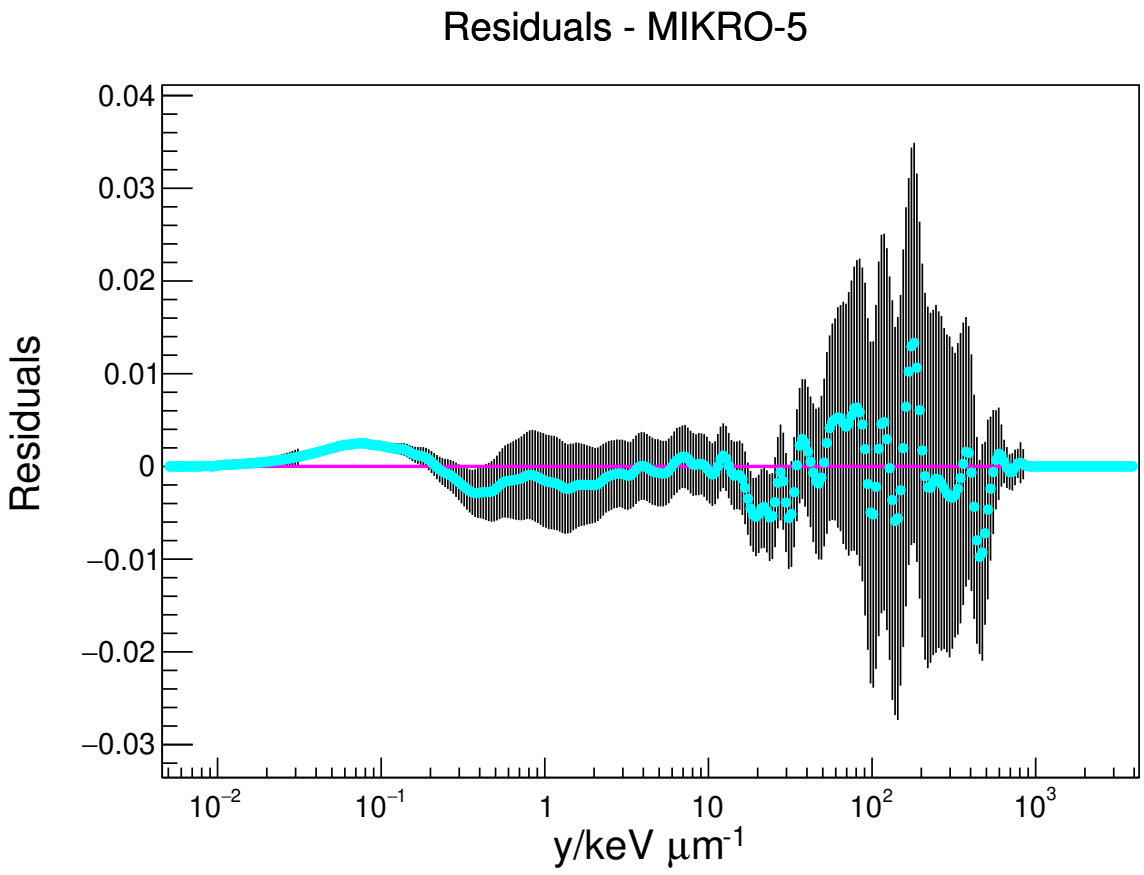

Figure 5.15: Residuals of *MIKRO-5* respect to the average.

The residuals suffer from large oscillations between 100 and 200 keV·μm^{-1}. Specifically, in all the graphs, the largest fluctuation is located around the region of the proton edge and it consists of a oscillating shape, with a rapid decrease of the residuals below zero followed by a sharp rise, or vice versa. This kind of behavior can be explained with a variation of the B parameter of the Fermi fit, describing a different steepness of the function around the inflection point. As an example, two Fermi functions with the same inflection point, same height but different slopes are reported in Figure 5.16, along with the difference between the two, simulating the residuals. Despite the fact that the position of the inflection point is the same, the different slopes generate sharp changes in the distribution of the residuals around zero due to the high gradient of the functions in the region around the inflection point, similar to the one obtained respect to the average. The change in the slope of the proton edge can be interpreted as a different resolution between the detectors, most likely due to slight differences in the gas pressure and purity.

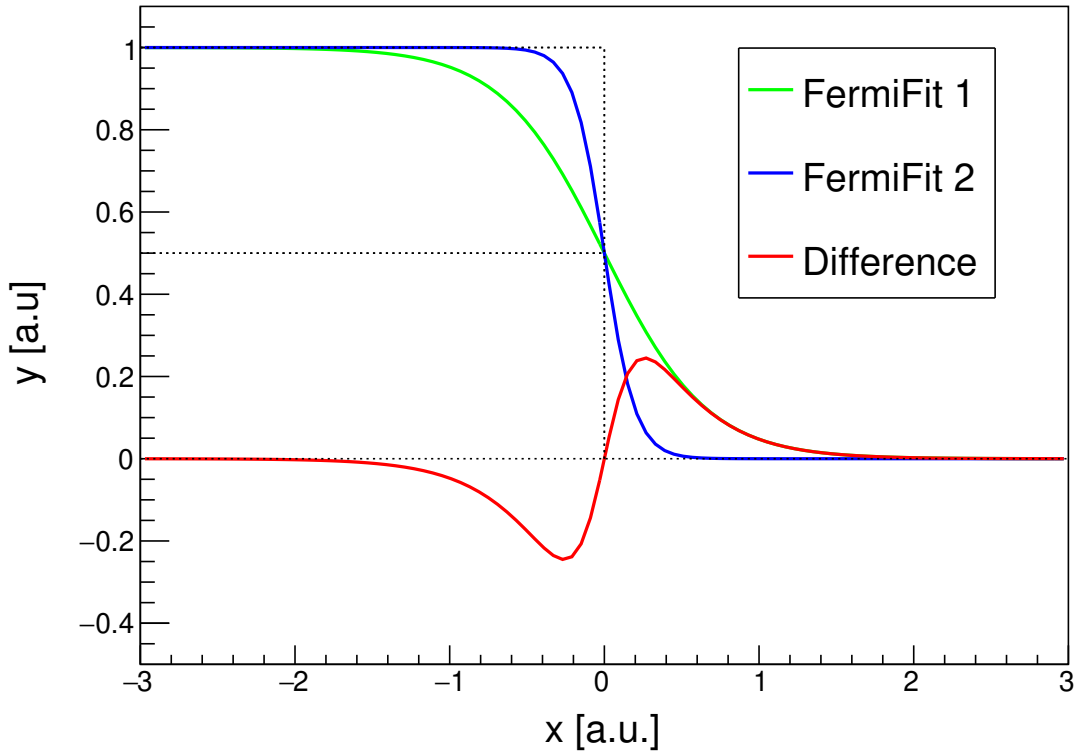

Figure 5.16: Example of the origin of the sinusoidal shape in the residuals. The vertical dotted line represents the position of the inflection point, which is the same for both the example functions.

Chapter 6

Measurements in therapeutic field

This second part of the analysis is focused on the response of the setup under high particles fluxes, similar to the ones used in proton therapy. With the therapeutic proton beam available at the Trento facility, several acquisitions of the same spectra have been obtained changing the beam current, allowing to study the response of the detector and the preamplifier at high particle rates.

Exploiting the fact that the proton beam in Trento is mono-directional (not isotropic as the neutron field at the CN accelerator), another set of measurement has been acquired, rotating the detector by 90°. The comparison between the rotated spectra is useful to determine if the detector is symmetric in its two main components, the anode and the internal plastic surface surrounding the active volume.

6.1 The Proton-Therapy Center

The Trento Proton Therapy facility is equipped with a cyclotron serving two medical treatment rooms in which, between 2014 and 2017, more than 300 patients have been treated. Moreover, two additional beam lines are dedicated to scientific applications, one is mainly used for radiobiology, while the second is predisposed for physics applications, including detector testing and radiation hardness measurements [42].

The cyclotron accelerates the proton beam up to a maximum energy of 228 MeV, after the extraction the energy is tuned via a rotating degrader with variable thickness, which allows a minimum energy of 70 MeV. The beam intensity can be chosen in a range between 1 and 320 nA, however lower beam currents can be achieved exploiting the accelerator *dark current*. This condition is obtained by reducing the high voltage of the accelerator source below the threshold used for standard operation and adjusting the proton beam flux by the cyclotron radio frequency. Particle rates between 10^1 and 10^5 Hz can be reached in this operation modality.

The beam delivered for physics applications is a fixed pencil beam with a gaussian profile. At the end of the beam pipe, the protons cross a 70 μm-thick titanium window and a laser system is used to align the detector at 1.25 m from the titanium plate. At 70 MeV, the energy used for this work, the full width at half maximum of the beam spot profile has been estimated as 6.93 mm for the x direction and 6.91 mm for the y direction, perpendicularly to the beam propagation direction [42, 43]. Under these conditions the uniform irradiation of the detector volume is ensured, since the dimensions of the active volume are much smaller than the beam spot. In general the beam spot decreases with increasing energy.

Due to the limited availability of beam-time, only one detector was tested at the proton facility center, namely the *MIKRO-5* detector, coupled with the *4MiCA-V1* preamplifier and the analog electronic chain previously described. The mini-TEPC has been filled at a pressure of 40.9 kPa, so that the sensitive volume diameter is equivalent to 1 μm of biological tissue, and biased at 750 V. A picture of the detector in position is presented in Figure 6.1.

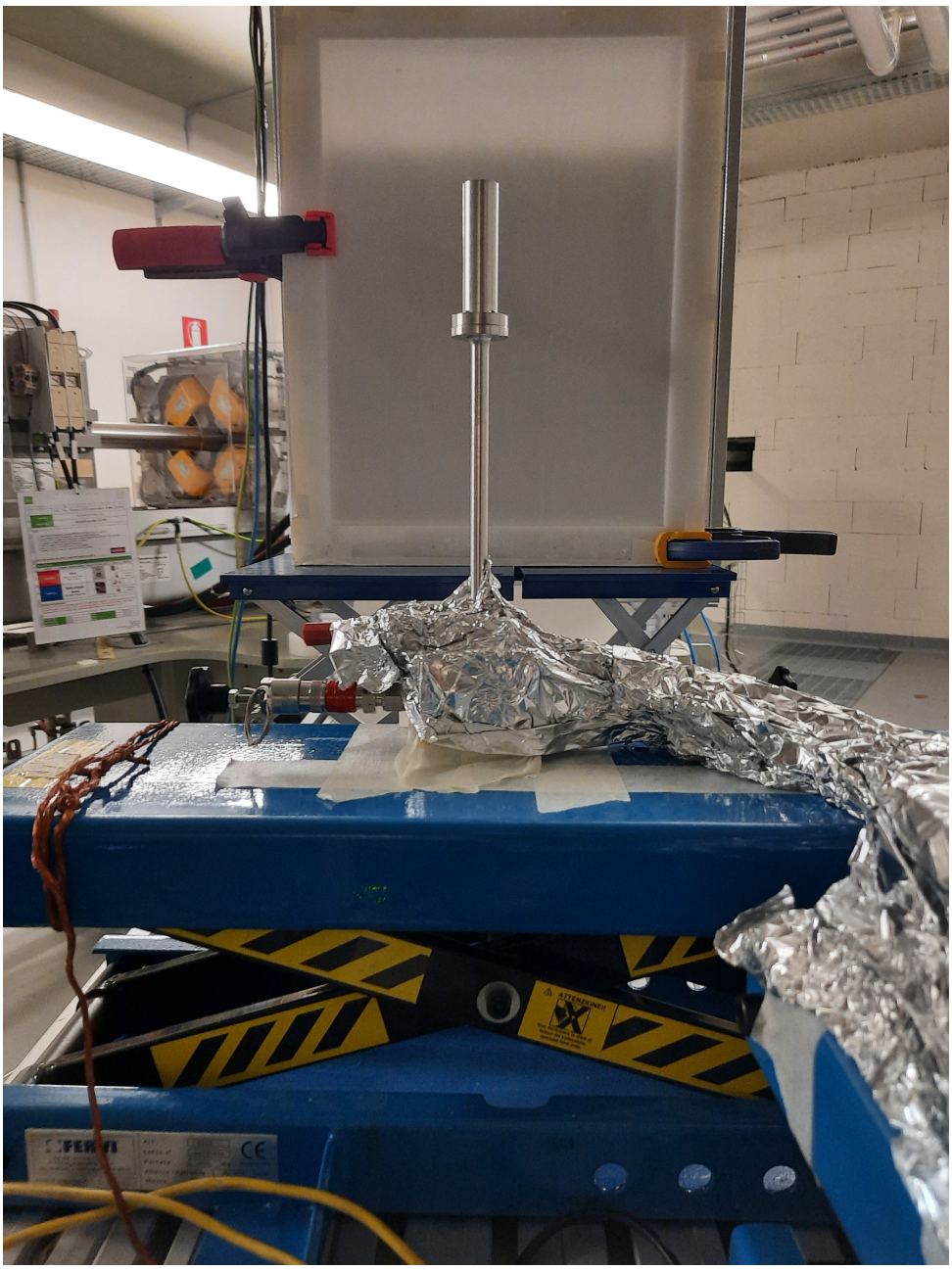

Figure 6.1: Position of the detector after being collimated with the laser system.

6.2 Test of the Maximum Sustainable Rate

The aim of these measurements is to verify the behavior of the detector and the preamplifier under high particles fluxes. The shaping time of the amplifiers has been set to the minimum available, 0.25 μs for the low LET chain and 0.5 μs for the high LET one, to avoid a large dead time.

A set of data using eleven values of beam current has been acquired, in particular two of them have been obtained in the *dark current* mode, at 0.2 nA and 0.5 nA. The remaining ones have been obtained in clinical mode, the nominal values of the beam current are from 1 to 7 nA, with a 1 nA step, and 10 nA. In addition, from the time information of the ADC, the counting rate in the detector has been evaluated as the number of counts divided by the live time of the acquisition, and reported in **p**articles **p**er **s**econd (pps). The acquired spectra, calibrated with a unique calibration factor, are shown in Figure 6.2 and the mean values are presented in Table 6.1.

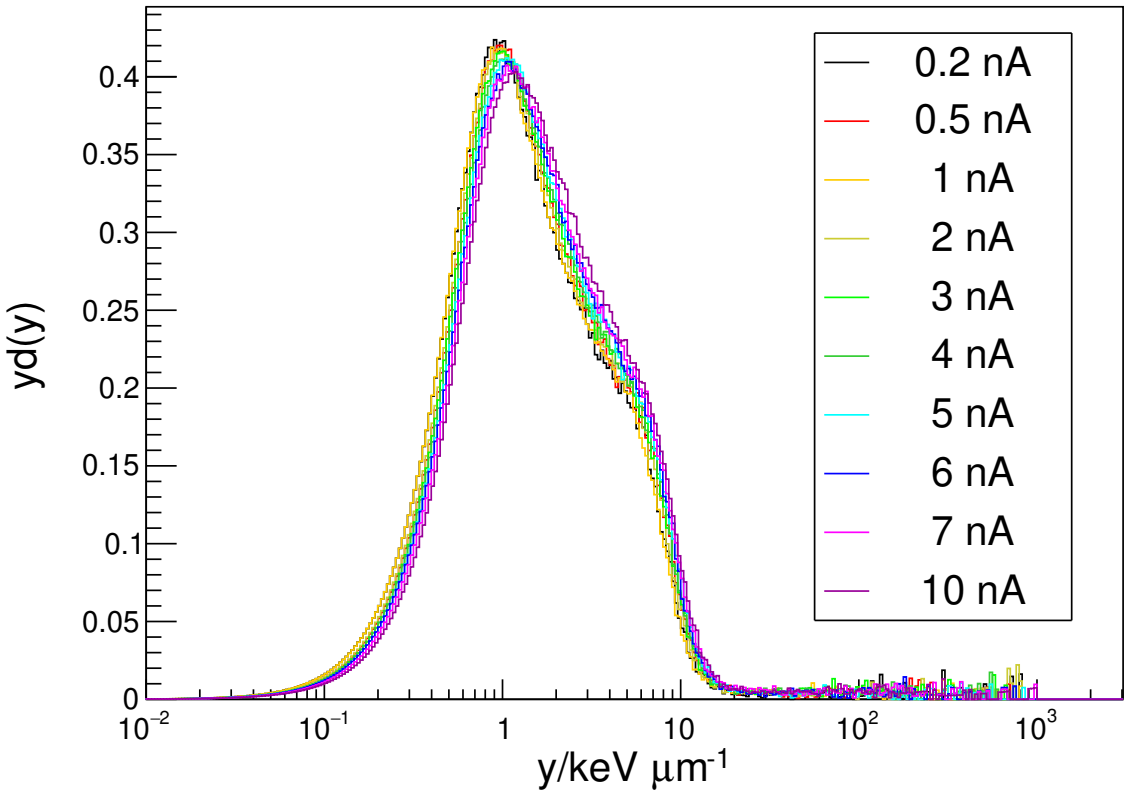

Figure 6.2: Spectra obtained with different beam currents.

Beam current [nA]	0.2	0.5	1	2	3	4	5	6	7	10
Detected rate [k pps]	2.0	4.9	11	20	29	39	50	61	72	108
$\overline{y_F}$ [keV·μm^{-1}]	0.78	0.78	0.78	0.83	0.86	0.86	0.89	0.90	0.93	0.98
$\overline{y_D}$ [keV·μm^{-1}]	4.62	4.86	4.69	6.05	4.76	5.06	4.58	4.80	5.23	5.83
$\overline{y_D}^*$ [keV·μm^{-1}]	2.11	2.09	2.10	2.21	2.28	2.32	2.38	2.40	2.47	2.55

Table 6.1: The mean values of the distribution as function of the beam current, expressed in nA. The origin of $\overline{y_D}^*$ is discussed in the next paragraph.

As debated in the previous chapter, the stochastic of the rare events with high LET compromise the ability of properly evaluate the $\overline{y_D}$. For this reason the $\overline{y_D}$ values have been re-evaluated cutting the spectra at 20 keV·μm^{-1} in order to remove the influence of the component of the spectra above that threshold. These new values, called $\overline{y_D}^*$, are reported in Table 6.1 and all the mean values of the spectra are pictured in Figure 6.3. Both the mean values presents a plateau region below 1 nA, after which they show an approximately linear trend.

To better visualize the data, the two sets have been normalized using the average of the points below 1 nA, which are reasonably constant. These sets are presented in Figure 6.4. It can be observed that both $\overline{y_F}$ and $\overline{y_D}^*$ follow the same trend of proportionality with respect to the beam current, or to the count rate. This can be interpreted as a rigid shift of the spectra toward higher values of y, as both the first and second momenta of the $f(y)$ distribution are moving in the same way. In the spectrum obtained at 10 nA the increased distance between normalized mean values suggests a deformation of the spectra due to pile-up.

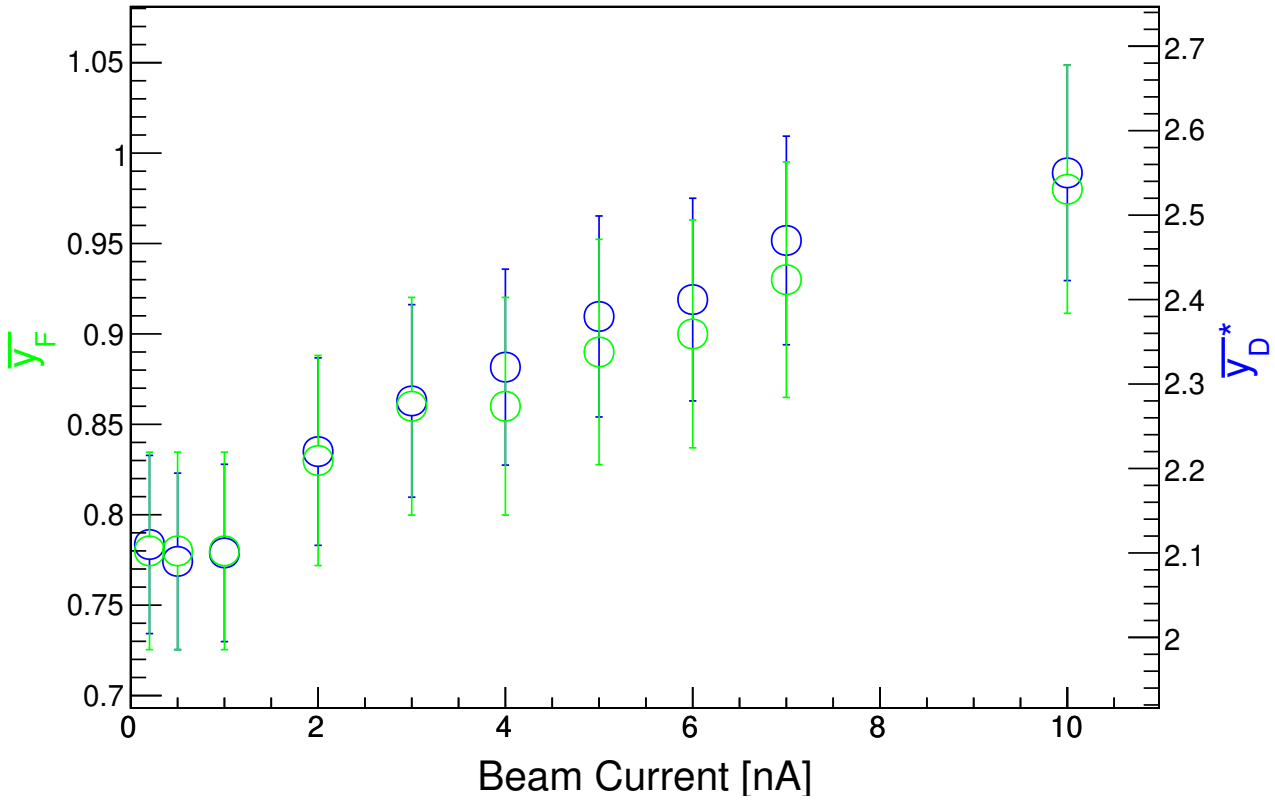

Figure 6.3: Mean values of the spectra as function of the beam current. Y-axes expressed in keV·μm^{-1}.

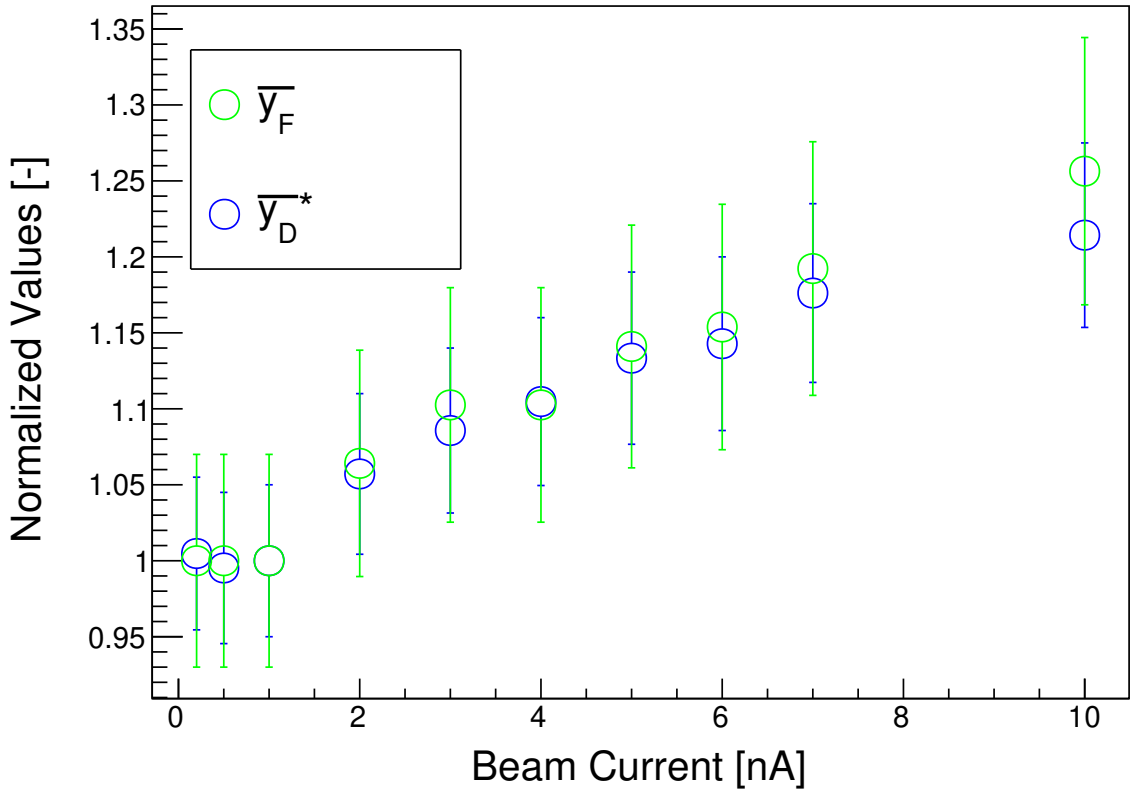

Figure 6.4: Mean values of the spectra, normalized by the average of the points below 1 nA.

The shift of the mean values can be furtherly studied in terms of the variance of the distribution. Given the definition of n-th momentum of a distribution, as reported in Equation 6.1, it follows that the $\overline{y_{\mathrm{D}}}$ is the ratio between second and first momentum of the $f(y)$ distribution, Equation 6.2. Subtracting one from this ratio, one can obtain the normalized variance of the $f(y)$ directly from the definition, as shown in Equation 6.3, where $\mathbb{E}[y]$ is the expectation value of y. The set of values obtained with this expression is presented in Figure 6.5. The variance of $f(y)$ is constant within the error bars, even if after 4 nA it is noted a drop of the variance, implying a "shrinking" of the distribution.

The shrinking effect may have been caused by the combination of two contributions:

- Electronic pile-up: at very high rates, the internal baseline may not have the time to return to zero and therefore the spectra are shifted toward higher values in millivolts, proportional to the number of events per unit of time, hence to the beam current.
- Detector pile-up: the flux of particles inside the detector is so high that two or more avalanches generated by different particles are collected at the same time, not only shifting the spectra but also reducing the probability of low energy events, shrinking the spectrum on the x-axis.

Unfortunately there has been no possibility to record the traces of the events and verify this theory, nor has been possible to test the setup with the digital ADC. Further tests including a pile-up rejection circuit could increase the maximum high rate sustainable by the setup that now has been found to be 40 kHz.

$$m_n = \int x^n p(x)\ \mathrm{d}x \tag{6.1}$$

$$\overline{y_{\mathrm{D}}} = \frac{\int y^2 f(y)\ \mathrm{d}y}{\overline{y_{\mathrm{F}}}} = \frac{m_2}{m_1} \tag{6.2}$$

$$\frac{\overline{y_{\mathrm{D}}}}{\overline{y_{\mathrm{F}}}} - 1 = \frac{m_2 - m_1^2}{m_1^2} = \frac{\mathbb{E}[y^2] - \mathbb{E}^2[y]}{\mathbb{E}^2[y]} = \sigma_y^2 \tag{6.3}$$

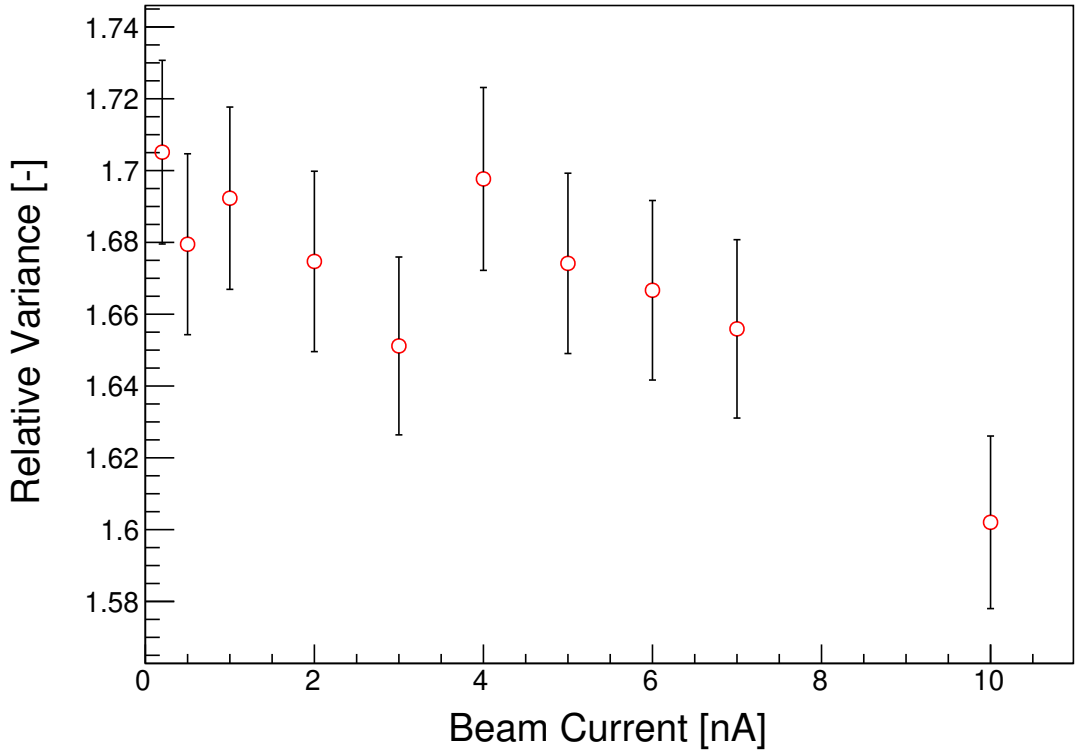

Figure 6.5: Distribution of the relative variance of the spectra as function of the beam current.

6.3 Angular Response

Another interesting feature to be investigated is the angular response of the detector when irradiated with a parallel beam orthogonal to its main axis. In the case of asymmetry of the detector, for example if the anode deviates from the cylinder' symmetry axis or if the internal surface of the plastic is not perfectly coaxial to the anode, the electric field inside the detector would be asymmetric as well and therefore the avalanche process would change as well. In addition, small differences are unavoidable, because of the presence of the wires that connect the electrodes to HV connectors.

Hence, rotating the detector by 90° is useful to spot possible defects in the symmetry of the detector. With the setup provided by the Trento facility both kinds of asymmetry could be tested. This test could not be performed at the CN facility since the interaction by neutrons takes place mainly in the detector walls, therefore the irradiation of the detector can be considered almost isotropic.

The angular response was tested at a proton energy of 70 MeV, both with the detector naked and behind a solid water (RW3) slab of 3.15 cm thickness. At low proton energy, because the LET (hence also the lineal energy distribution) of protons varies more rapidly when they have small energy, close to the Bragg peak. The response of the detector is therefore more sensitive to small variations in the wall thickness and composition, while the high energy proton measurement could underline a difference in the gain of the detector if the anode is not centered correctly.

To decrease the initial energy of impinging protons, the 3.15 cm thick solid-water slab (RW3) has been placed between the end of the beam pipe and the detector.

A first measurement, with the *RW3* phantom, has been acquired with a beam current of 1.2 nA, after that, the detector has been rotated by 90°. For the second set of measurements, the absorber has been removed and the beam current has been kept at 2 nA, with the detector placed at 0° and 90°.

The spectra are shown in Figure 6.6. The χ variable has been evaluated in the two cases, the results are presented in Table 6.2.

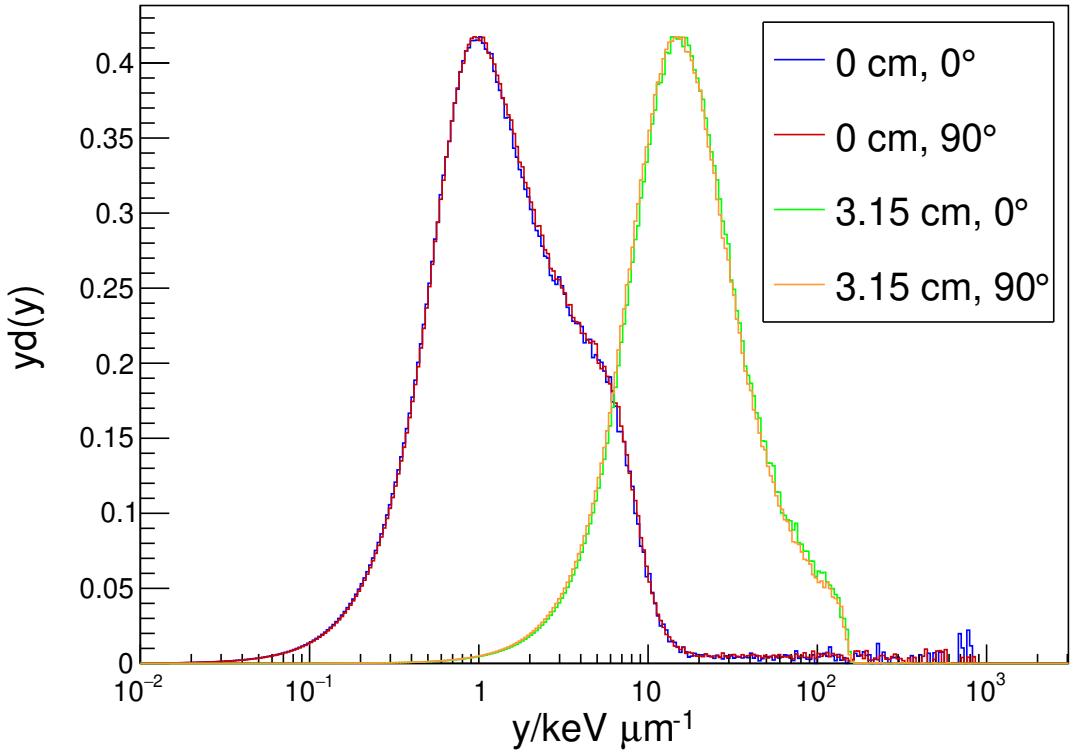

Figure 6.6: The spectra obtained rotating the detector of 90°, with and without the absorber.

χ [%]	Total	< 10 keV·μm^{-1}	$10 - 147$ keV·μm^{-1}
3.15 cm	6.5	7.5	3.5
0 cm	9.6	2.6	30.0

Table 6.2: Mean distance in percentage between the spectrum obtained with the detector at 0° and 90°, with and without the 3.15 cm thick absorber.

For the spectra acquired with the 3.15 cm panel, without considering the lower portion of the spectra which difference is due to the uncertainty of the extrapolation, the spectra are different for a 3.5%, which is slightly larger than the differences between prototypes obtained at the CN facility. In addition, the rotated spectrum is shifted towards lower values of y, this shift is compatible with a reduction in thickness of less than 10 μm, which is in line with the tolerances of the machines used to construct the components. In the data without the absorber, most of the events are below the 10 keV·μm^{-1} threshold, and the rotation produces a difference of 2.6%, which can be associated to the statistical uncertainties of the measurement.

Despite the differences in the spectra, the mean values, reported in Table 6.3 are similar within a few percent. Also in this case, for the data at the entrance, the $\overline{y_{\mathrm{D}}}^*$ has been evaluated, with a cut on 20 keV·μm^{-1}, in order to reduce the contribution originated by rare high-LET events. Expressing the variation of the mean values as

$$\sigma = \frac{y_1 - y_2}{(y_1 + y_2)/2} \tag{6.4}$$

the differences are of 3.2% for the $\overline{y_{\mathrm{F}}}$ and 2.9% for $\overline{y_{\mathrm{D}}}$, for the data set with the absorber. In the other case the variations between mean values are of 2.4% and 1.3% for the $\overline{y_{\mathrm{F}}}$ and $\overline{y_{\mathrm{D}}}^*$, respectively. All the obtained variations are within the standard uncertainties assigned to the frequency and dose mean lineal energies, thus it can be concluded that no significant asymmetry is observed in the detector.

cm	deg	$\overline{y_{\mathrm{F}}}$ [keV·μm^{-1}]	$\overline{y_{\mathrm{D}}}$ [keV·μm^{-1}]	$\overline{y_{\mathrm{D}}}^*$ [keV·μm^{-1}]
3.15	0°	11.34	24.59	-
3.15	90°	10.98	23.89	-
0	0°	0.82	6.05	2.22
0	90°	0.84	4.93	2.24

Table 6.3: The mean values of the distributions for the different setups.

Chapter 7

Conclusions and Perspectives

The purpose of this thesis is the characterization of a new microdosimetric device, specifically designed and constructed to be used in proton therapy centers by medical physicists. In order to be introduced in the clinical practice by a non-expert user, i.e. by a medical physicist, the equipment has to fulfill three main properties: reasonable cost, stability and ease of operation. In particular, the stability of the response of the detectors has to be verified in terms of the mean values, $\overline{y_F}$ and $\overline{y_D}$, of the microdosimetric spectra, whose overall estimated uncertainties are less than 7% and 5%, respectively.

Five new mini-TEPCs have been designed and constructed at the technical office and mechanical workshop of INFN-LNL, employing computer numerical control machines and with engineering techniques allowing better reproducibility of the processes and a reduction of time and production costs.

As an important part of this thesis work, a dedicated software for the data analysis has been developed, with the objective of being as intuitive and simple as possible to be used by medical physicists in clinical practice. As described in Chapter 3, the software, called *MikAna*, is provided with a GUI and assists the user during all the analysis process, from the calibration to the extrapolation and the evaluation of the mean values. In addition, it is equipped with several automatic controls that guarantee the outcome of the process, such as the linearity test on the electronic calibration, and warns the user in case of mistakes during the procedure. In order to test the functioning and the stability of *MikAna*, all the data in this work have been analyzed with the new software and the results have been compared among different machines and performed by different operators, verifying the stability and robustness of the procedure.

A new prototype preamplifier, *4MiCA-V1*, has been specifically developed for microdosimetric applications at *Politecnico di Milano*. The preamplifier is provided with two different outputs, with x1 and x10 amplification factors; it has been tested and compared to the commercial *142PC* by *ORTEC*, with the same analog chains, presenting a larger dynamic range and a lower noise level. However, the x1 amplification channel, which can reach up to 10 V before saturating, suffers from non-linearity above 800 mV, hence the circuit is still undergoing further improvements.

The first part of this work, reported in Chapter 5.3, has been dedicated to test the reproducibility of the response function of the five mini-TEPCs, through the exposure of the detectors to the same neutron field at the CN accelerator of the INFN-LNL. Despite a difference in the internal gain of the detectors, which can be due to slightly different gas pressures and will be further investigated in the future, both the spectra and the mean values have been found to be overall compatible with each others. In particular, the average $\overline{y_F}$ has been evaluated as (0.88 ± 0.03) keV$\cdot\mu$m^{-1}, and the $\overline{y_D}$ resulted (43 ± 2) keV$\cdot\mu$m^{-1}, with relative standard deviations of 3.4% and 4.6%, respectively. Therefore the engineering procedures employed to construct the devices are precise enough to comply with the requirements, and the detectors can be considered completely reproducible. The higher variance of the $\overline{y_D}$ is due to the poor statistics of rare high-LET events, and could be further reduced with longer acquisition times. Unfortunately, due to beam time constraints, longer acquisitions were not possible.

Using the therapeutic proton beam at the Trento Proton Therapy Center, the response of the setup as function of the count rate has been studied, employing one of the detectors and the preamplifier *4MiCA-V1*, as presented in Chapter 6.2. The $\overline{y_F}$ can be considered constant below 10^4 counts per second, then it increases linearly with the count rate, being however stable up to $4 \cdot 10^4$ counts per second if a 7% uncertainty is taken into account. For the $\overline{y_D}$ the situation is very similar. However, the normalized variance of the spectra, evaluated from the first and second momentum of the $f(y)$ distribution, suggests that after 10^4 counts per second not only the spectra are shifted, but also deformed due to pile-up. The situation can be likely improved by implementing a pile-up rejection circuit in the electronic chain. Further studies are required to optimize the response function of the microdosimetric setup at high count rates.

For the last test, as described in Chapter 6.3, the angular response of the detector under rotations has been investigated. Two datasets have been acquired, one with the 70 MeV clinical proton beam, and one at lower energy, achieved by interposing a 3.15 cm layer of solid water (RW3) between the beam exit and the detector, rotating the device by 90° in each case. The $\overline{y_F}$ of the distributions differ by 3.2% at low energy and 2.4% at 70 MeV, while the $\overline{y_D}$ differ by 2.9% at low energy. At 70 MeV larger fluctuations are produced by rare large energy deposition events, due to target fragments. If these rare events are not considered in the averaging process, the $\overline{y_D}$ values obtained at 0 and 90° differ by only 1.3%. The mean values of the distribution are therefore the same within their uncertainties, thus the response of the detector at different angles remains unchanged under rotations. Further studies are required to investigate the effect of rotations of smaller angles, such as 5 or 10°, since a small misplacing in the rotation is more likely to occur during the positioning of the device.

Bibliography

[1] IARC World Cancer Report 2020

[2] Isselbacher K.J., Braunwald E., Wilson J.D., Martin J.B., Fauci A.S., Kasper D.L., ed., *Principles of Internal Medicine, vol. 2*, McGraw-Hill (1994).

[3] M. Durante, J. S. Loeffler, *Charged particles in radiation oncology*, Nat Rev Clin Oncol. 2010 Jan;7(1):37-43. doi: 10.1038/nrclinonc.2009.183. Epub 2009 Dec 1. PMID: 19949433.

[4] G. F. Knoll, *Radiation Detection and Measurements*, Fourth Edition.

[5] H. Paganetti, *Relative biological effectiveness (RBE) values for proton beam therapy. Variations as a function of biological endpoint, dose, and linear energy transfer*, Phys Med Biol. (2014) 59: 419– 472.

[6] P. Chaudhary, T. I. Marshall, F. M. Perozziello, et al. *Relative biological effectiveness variation along monoenergetic and modulated Bragg peaks of a 62-MeV therapeutic proton beam: a preclinical assessment*, Int J Radiat. Oncol. Biol. Phys. (2014) 90: 27–35.

[7] H. H. Rossi and M. Zaider, *Microdosimetry and Its Applications*, Springer - Heidelberg, 1996.

[8] C. P. Karger, P. Peschke, *RBE and related modeling in carbon-ion therapy*, Phys Med Biol. 2017 Dec 19;63(1):01TR02. doi: 10.1088/1361-6560/aa9102. PMID: 28976361.

[9] B. Sørensen, J. Overgaard, N. Bassler, *In vitro RBE-LET dependence for multiple particle types*, Acta oncologica (Stockholm, Sweden). 50. 757-62. doi: 10.3109/0284186X.2011. PMID: 582518.

[10] International Commission on Radiation Units and Measurements, *Microdosimetry, ICRU Report 36*, 1983.

[11] Paul Reuss, *Cauchy's theorem and generalization*, EPJ Nuclear Sci. Technol. 4, 50 (2018). doi: 10.1051/epjn/2018010.

[12] L. Lindborg, M. Hultqvist, Å. Carlsson Tedgren, H. Nikjoo, *Lineal energy and radiation quality in radiation therapy: model calculations and comparison with experiment*, Phys Med Biol. 2013 May 21;58(10):3089-105. doi: 10.1088/0031-9155/58/10/3089. PMID: 23594445.

[13] A. Bianchi, D. Mazzucconi, A. Selva, P. Colautti, A. Parisi, F. Vanhavere, B. Reniers, V. Conte, *Lineal energy calibration of a mini-TEPC via the proton-edge technique*, Radiation Measurements, Volume 141, 2021, 106526, ISSN 1350-4487, https://doi.org/10.1016/j.radmeas.2021.106526

[14] D. T. Goodhead, *An assessment of the role of microdosimetry in radiobiology*, Radiat Res. 1982 Jul;91(1):45-76. PMID: 7048402.

[15] P. Olko, *Fluctuations of Energy Deposited in Biological Targets by Ionizing Radiation*, Thesis at the Institute of Nuclear Physics of Krakov (1989).

[16] T. Loncol, V. Cosgrove, J.M. Denis, J. Gueulette, A. Mazal, H.G. Menzel, P. Pihet, R. Sabattier, *Radiobiological Effectiveness of Radiation Beams with Broad LET Spectra: Microdosimetric Analysis Using Biological Weighting Functions*, Radiation Protection Dosimetry, Volume 52, Issue 1-4, 1 April 1994, Pages 347–352, https://doi.org/10.1093/oxfordjournals.rpd.a082212

[17] L. De Nardo, V. Cesari, N. Iborra, V. Conte, P. Colautti, et al., *Microdosimetric Assessment of Nice Therapeutic Proton Beam Biological Quality*, Physica medica : european journal of medical physics : XX, 2, 2004.

[18] R. B. Hawkins, *A microdosimetric-kinetic model for the effect of non-Poisson distribution of lethal lesions on the variation of RBE with LET*, Radiat Res. 2003 Jul;160(1):61-9. doi: 10.1667/rr3010. PMID: 12816524.

[19] Y. Kase, T. Kanai, Y. Matsumoto, Y. Furusawa, H. Okamoto, T. Asaba, M. Sakama, H. Shinoda, *Microdosimetric measurements and estimation of human cell survival for heavy-ion beams*, Radiat Res. 2006 Oct;166(4):629-38. doi: 10.1667/RR0536.1. PMID: 17007551.

[20] L. De Nardo, V. Cesari, G. Donà, G. Magrin, P. Colautti, V. Conte, G. Tornielli, *Mini-TEPCs for radiation therapy*, Radiat Prot Dosimetry. 2004;108(4):345-52. doi: 10.1093/rpd/nch023. PMID: 15103064.

[21] Waker, A. J., *Principles of experimental microdosimetry*, United Kingdom: N. p., 1995.

[22] S. Chiriotti, D. Moro, P. Colautti, V. Conte, B. Grosswendt, *Equivalence of pure propane and propane TE gases for microdosimetric measurements*, Radiat Prot Dosimetry. 2015 Sep;166(1-4):242-6. doi: 10.1093/rpd/ncv293. Epub 2015 May 4. PMID: 25944956.

[23] Anatoly B. Rosenfeld, *Novel detectors for silicon based microdosimetry, their concepts and applications*, Nuclear Instruments and Methods in Physics Research Section A: Accelerators, Spectrometers, Detectors and Associated Equipment, Volume 809, 2016, Pages 156-170, ISSN 0168-9002, https://doi.org/10.1016/j.nima.2015.08.059.

[24] J. Prieto-Pena, F. Gómez, C. Guardiola, G. Pellegrini, C. Fleta, M. Donetti, S. Giordanengo, D. González-Castaño, J. Pardo-Montero, *Microdosimetric Spectra Measurements on a Clinical Carbon Beam at Nominal Therapeutic Fluence Rate With Silicon Cylindrical Microdosimeters*, IEEE Transactions on Nuclear Science. 10.1109/TNS.2019.2921453.

[25] L. T. Tran, L. Chartier, D. A. Prokopovich, D. Bolst, M. Povoli, A. Ummanwar, et al., *Thin silicon microdosimeter utilizing 3D MEMS technology: charge collection study and its application in mixed radiation fields*, IEEE Transactions on Nuclear Science. (2018) 65:467–472. doi: 10.1109/TNS.2017.2768062

[26] C. Verona, G. Magrin, P. Solevi, M. Bandorf, M. Marinelli, M. Stock, et al., *Toward the use of single crystal diamond based detector for ion-beam therapy microdosimetry*, Radiat Meas. (2018) 110:25–31. doi: 10.1016/j.radmeas.2018.02.001

[27] S. Agosteo, P. Colautti, I. Fanton, A. Fazzi, M. V. Introini, D. Moro, et al., *Study of a solid state microdosimeter based on a monolithic silicon telescope: irradiations with low-energy neutrons and direct comparison with a cylindrical TEPC*, Radiat Prot Dosimetry. (2011) 143:432–5. doi: 10.1093/rpd/ncq481

[28] Dicello, J. F., et al., *A Comparison of Microdosimetric Measurements with Spherical Proportional Counters and Solid-State Detectors*, Radiation Research, vol. 82, no. 3, 1980, pp. 441–53. JSTOR, https://doi.org/10.2307/3575311.

[29] D. Bortoletto, et al., *TF3 Symposium: Solid State Detectors ECFA Detector R&D Roadmap*, 2021.

[30] L. De Nardo, V. Cesari, G. Donà, G. Magrin, P. Colautti, V. Conte, G. Tornielli, *Mini-TEPCs for radiation therapy*, Radiat Prot Dosimetry. 2004;108(4):345-52. doi: 10.1093/rpd/nch023. PMID: 15103064

[31] V. Conte, A. Bianchi, A. Selva, G. Petringa, G. A. P. Cirrone, A. Parisi, F. Vanhavere, P. Colautti, *Microdosimetry at the CATANA 62 MeV proton beam with a sealed miniaturized TEPC*, Phys Med. 2019 Aug;64:114-122. doi: 10.1016/j.ejmp.2019.06.011. Epub 2019 Jul 10. PMID: 31515010

[32] V. Conte, A. Bianchi, F. Pasquato, M. Rossignoli, A. Selva, *A new prototype of mini-TEPC*, LNL Annual Report 2020.

[33] A. Bianchi, A. Selva, P. Colautti, G. Petringa, P. Cirrone, B. Reniers, A. Parisi, F. Vanhavere, V. Conte, *Repeatability and Reproducibility of Microdosimetry With a Mini-TEPC*, Frontiers in Physics. 10.3389/fphy.2021.727816.

[34] https://www.qt.io/

[35] https://root.cern.ch/

[36] V. Conte, et al., *Lineal Energy Calibration Of Mini Tissue-Equivalent Gas-Proportional Counters (TEPC)*, AIP Conference Proceedings. 1530. 171-178. 10.1063/1.4812920.

[37] D. Moro, S. Chiriotti, V. Conte, P. Colautti, B. Grosswendt, *Lineal energy calibration of a spherical TEPC*, Radiation Protection Dosimetry, Volume 166, Issue 1-4, September 2015, Pages 233–237, https://doi.org/10.1093/rpd/ncv153

[38] A. Bianchi, D. Mazzucconi, A. Selva, P. Colautti, A. Parisi, F. Vanhavere, B. Reniers, V. Conte, *Lineal energy calibration of a mini-TEPC via the proton-edge technique*, Radiation Measurements, 141, 106526.

[39] A. Bianchi, A. Selva, P. Colautti, A. Parisi, F. Vanhavere, B. Reniers, V. Conte, *The effect of different lower detection thresholds in microdosimetric spectra and their mean values*, Radiation Measurements, Volume 146, 2021, 106626, ISSN 1350-4487, https://doi.org/10.1016/j.radmeas.2021.106626.

[40] https://www.fwt.com

[41] D. Moro, E. Seravalli, P. Colautti, *Statistical and Overall Uncertainties in Proton Therapy Microdosimetric Measurements*, LNL Report 200/2003 (2003).

[42] F. Tommasino, M. Rovituso, S. Fabiano, S. Piffer, C. Manea, S. Lorentini, S. Lanzone, Z. Wang, M. Pasini, W.J. Burger, C. La Tessa, E. Scifoni, M. Schwarz, M. Durante, *Proton beam characterization in the experimental room of the Trento Proton Therapy facility*, Nuclear Instruments and Methods in Physics Research Section A: Accelerators, Spectrometers, Detectors and Associated Equipment, Volume 869, 2017, Pages 15-20, ISSN 0168-9002, https://doi.org/10.1016/j.nima.2017.06.017.

[43] F. Tommasino, M. Rovituso, E. Bortoli, C. La Tessa, G. Petringa, S. Lorentini, E. Verroi, Y. Simeonov, U. Weber, P. Cirrone, M. Schwarz, M. Durante, E. Scifoni, *A new facility for proton radiobiology at the Trento proton therapy centre: Design and implementation*, Phys Med. 2019 Feb;58:99-106. doi: 10.1016/j.ejmp.2019.02.001. Epub 2019 Feb 11. PMID: 30824157.